ANALYSIS OF FORCE COEFFICIENTS AND DYNAMIC PRESSURES FOR SHORT-LENGTH (L/D=0.2) OPEN-ENDS SQUEEZE FILM DAMPERS

A Thesis

by

SEAN DEN

Submitted to the Office of Graduate and Professional Studies of
Texas A&M University
in partial fulfillment of the requirements for the degree of

MASTER OF SCIENCE

Chair of Committee,	Luis A. San Andrés
Committee Members,	Andreas Polycarpou
	Yong Joe Kim
	Matthew Kuttalamodam
Head of Department,	Andreas Polycarpou

December 2015

Major Subject: Mechanical Engineering

ABSTRACT

Gas turbine engine manufacturers push for increasingly simpler squeeze film damper (SFD) designs that can still provide necessary damping to suppress rotor vibrations and offer stability to rotor-bearing systems. The work in this thesis addresses to industry needs by analyzing the experimental and predicted dynamic force performance of a very simply configured test SFD. The SFD incorporates three lubricant feedholes spaced 120° apart, a single short-length (L/D=0.2, L=2.54 cm) film land with no central feed groove, no end grooves for the provision sealing mechanisms (open-ends), and a nominal radial clearance c=0.267 mm (c/R=0.004).

Analysis of the SFD performing whirl orbits with various amplitude (r) and departing from various static eccentricity (e_s) endeavors to reveal the dynamic performance of SFDs to events in gas turbine engine operation such as a blade loss, or a change in eccentricity. Circular (r_X=r_Y) whirl orbits of the SFD with amplitude r/c=0.05 to 0.71, and departing from static eccentricity, e_s/c=0 to 0.86 lead to identification of the squeeze film force coefficients and measurements of the dynamic film pressures over the various dynamic operating conditions. Comparisons of experimentally identified force coefficients to those predicted by a finite element orbit-based model as well as those predicted by the classical short-length open-ends SFD theory strive to evaluate the accuracy of the state-of-the-art in SFD performance prediction. Comparisons of experimental results for the current SFD (termed damper 1) against that of two SFDs with similar configurations (dampers 2 and 3) examined in prior art, advance the simplicity of SFD design by highlighting the effects of a smaller radial clearance (in

damper 2) and the effects of end grooves (in damper 3) on SFD dynamic force performance.

Experimentally identified force coefficients for the current damper (#1) show moderate growth with orbit amplitude and strong nonlinear growth with static eccentricity, in particular at a largely off-centered position. Added mass coefficients for damper 1 increase with static eccentricity and, unexpectedly, with orbit amplitude. The experimentally identified SFD force coefficients for damper 1 exhibit excellent agreement with predicted force coefficients from the orbit-based model and the short-length open-ends model for whirl orbits departing from centered to slightly off-centered positions ($e/c < 0.4$) and with a small orbit amplitude ($r/c < 0.4$).

The fluid film dynamic *peak-to-peak* (*p-p*) pressures exhibit a strong growth with orbit amplitude, and a moderate growth with static eccentricity. Inconsistent increases in *p-p* pressure with whirl frequency demonstrate the occurrence of air ingestion for motions with a large orbit amplitude or departing from a large static eccentricity.

Comparisons of the current damper (damper 1) with damper 2 and 3 demonstrate that the damping and added mass force coefficients closely follow geometric ratios $(L/c)^3$ and (L^3/c), respectively, derived from the short-length open-ends SFD model. Damper 2, with ~half clearance (c_2=0.122 mm), produces eight times more damping and 1.9 times more added mass than does damper 1. Damper 3 with similar clearance (c_3=0.254 mm) and slightly longer film land length (L_{eff}=2.97 cm), produces just 1.75 times more damping and 2.12 times more added mass than does damper 1.

ACKNOWLEDGEMENTS

I thank Dr. L. San Andrés, my committee chair, for his patience, guidance, and detail throughout the course of my time in his research group, and for his life lessons that helped me become a better engineer. I also thank my committee members, Dr. A. Polycarpou, Dr. Y.J. Kim, and Dr. M. Kuttalomodam, for their support in my thesis.

I especially acknowledge Mr. Sung-hwa Jeung for his mentorship, instruction, and encouragement while I matured as a graduate researcher. I extend my gratitude to Pratt and Whitney Engines, which sponsored and provided objectives in this research. I also thank my friends, colleagues and the staff at the Texas A&M Turbomachinery Laboratory for making my time there an enriching experience.

Finally, I thank my father, mother, sister, and my friends for their encouragement and support in my decision to enroll at Texas A&M University to pursue a M.S. degree in Mechanical Engineering.

TABLE OF CONTENTS

Page

LIST OF FIGURES

Page

LIST OF TABLES

NOMENCLATURE

a	Bearing cartridge acceleration [m/s^2]
c	SFD radial clearance [mm]
$C_{i,j\ (i,j=x,y)}$	Damping coefficients [kN·s/m]
C^*	Damper 1 damping predicted by the short-length open-ends model for small amplitude motions about the centered position. [0.46 kN·s/m]
$\bar{C}_{i,j(i,j=x,y)}$	Normalized damping coefficient C/C^* [-]
C_{total}	Fluid flow conductance [m^3/s/Pa]
D	Journal diameter (R/2) [cm]
e	Journal eccentricity [μm]
h	Lubricant film thickness [μm]
$F_{i,j\ (i,j=x,y)}$	Excitation force [N]
$H_{(\omega)i,j\ (i,j=x,y)}$	Complex stiffness function, $(K\text{-}M\omega^2+i\omega C)_{i,j}$ [N/m]
$K_{i,j\ (i,j=x,y)}$	Stiffness coefficients [MN/m]
L	Film land axial length [cm]
M_{BC}	Mass of bearing cartridge [kg]
$M_{i,j\ (i,j=x,y)}$	Added mass coefficients [kg]
M^*	Damper 1 added mass predicted by the short-length open-ends model for small amplitude motions about the centered position. [0.82 kg]
$\bar{M}_{i,j(i,j=x,y)}$	Normalized added mass coefficient M/M^* [-]
O	Coordinates of a center position [m,m]
P	Dynamic pressure in film land [bar]
P_a, P_{cav}	Ambient pressure and lubricant cavitation pressure [Pa]
P_{in}	Lubricant supply pressure [Pa]
Q_{in}	Lubricant supply flow rate [m^3/s]
r	Whirl orbit amplitude [μm]
R	Journal radius [mm]
Re_s	Squeeze film Reynolds number, $\rho\omega c^2/\mu$ [-]
T	Temperature [°C]

t	Time [s]
$U_{C_{SFD}}$, $U_{K_{SFD}}$, $U_{M_{SFD}}$	Uncertainties in damping, stiffness, and inertia coefficients
x, y	Displacement along X and Y directions [mm]
z	Film land axial location [mm]
θ, Θ	Rotating and fixed coordinates [°]
ϕ	Feedhole diameter [mm]
μ	Lubricant dynamic viscosity [cP]
ρ	Lubricant density [kg/m^3]
ω, ω_n	Excitation (whirl) frequency, natural frequency [rad/s]

Matrices and Vectors

a	Matrix of bearing acceleration [m/s^2]
C	Matrix of damping coefficients $\mathbf{C}=\mathbf{C}_s+\mathbf{C}_{SFD}$ [kN·s/m]
K	Matrix of stiffness coefficients $\mathbf{K}=\mathbf{K}_s+\mathbf{K}_{SFD}$ [MN/m]
F	Vector of excitation force [N]
H	Complex stiffness matrix, $\mathbf{K}-\mathbf{M}\omega^2+i\omega\mathbf{C}$, [N/m]
M	Matrix of added mass coefficients $\mathbf{M}=\mathbf{M}_s+\mathbf{M}_{SFD}$ [kg]
z, ż, z̈	Vectors of bearing absolute displacement, velocity, and acceleration [m, m/s, m/s^2]
z	Vector of static plus dynamic displacement $\mathbf{z_s}+\mathbf{z_{dyn}}$ [m]

Subscripts

1	Current damper configuration, c_1=0.267 mm
2	Prior damper configuration with smaller radial clearance c_2=0.122 mm
3	Prior damper configuration with end grooves, c_3=0.254 mm, L_{eff}=2.97 cm
dyn	Dynamic
eff	Effective
ext	External
L	Related to the lubricated system
S	Related to the dry structure
s	Static position or component
SFD	Related to the squeeze film, *SFD=L-S*

CHAPTER I

INTRODUCTION

Squeeze film dampers (SFDs) are thin fluid film mechanical elements that provide viscous damping to mechanical systems. SFDs aid to attenuate rotor vibration, isolate mechanical components, and on occasion serve to tune the placement of system critical speeds. Current industrial practices often involve retrofitting SFDs onto rotating machinery due to their aptitude as a "quick fix" and ease of implementation into existing machinery without costly overhauls [1]. The primary disadvantage of SFDs, however, comes due to their viscous damping, they dissipate mechanical energy, which in turn, increases power loss. Furthermore, practitioners often use SFDs to remedy the "symptoms" of a mechanical problem, i.e., excessive synchronous rotor vibration, but not its source.

Gas-turbine aircraft engines, for example, heavily rely on SFDs for safe operation [2-4]. Rather than retrofit, however, aircraft engines deliberately incorporate SFDs into their design. This is due to an aircraft engine's use of rolling element bearings to reduce weight and complexity, and to prevent, for example, the risk of oil supply interruption and rotordynamic instability in hydrodynamic bearings [2-4]. Consequently, the squeeze film damper remains the primary means to damp rotor vibrations.

Figure 1 depicts a schematic of a SFD and its configurations [2]. In aircraft engines, a non-rotating journal (or sleeve) holds the outer race of a rolling element bearing. The journal does not rotate due to an anti-rotation pin but displaces with a circular path (whirls) within a thin annulus (clearance) filled with lubricant between the

journal and the bearing housing. Lubricant supplied to the clearance between the journal and the housing produces hydrodynamic pressures when the journal whirls. The hydrodynamic pressures exert reaction forces on the journal that damp the rotor amplitude of motion and isolate the journal from the housing [2].

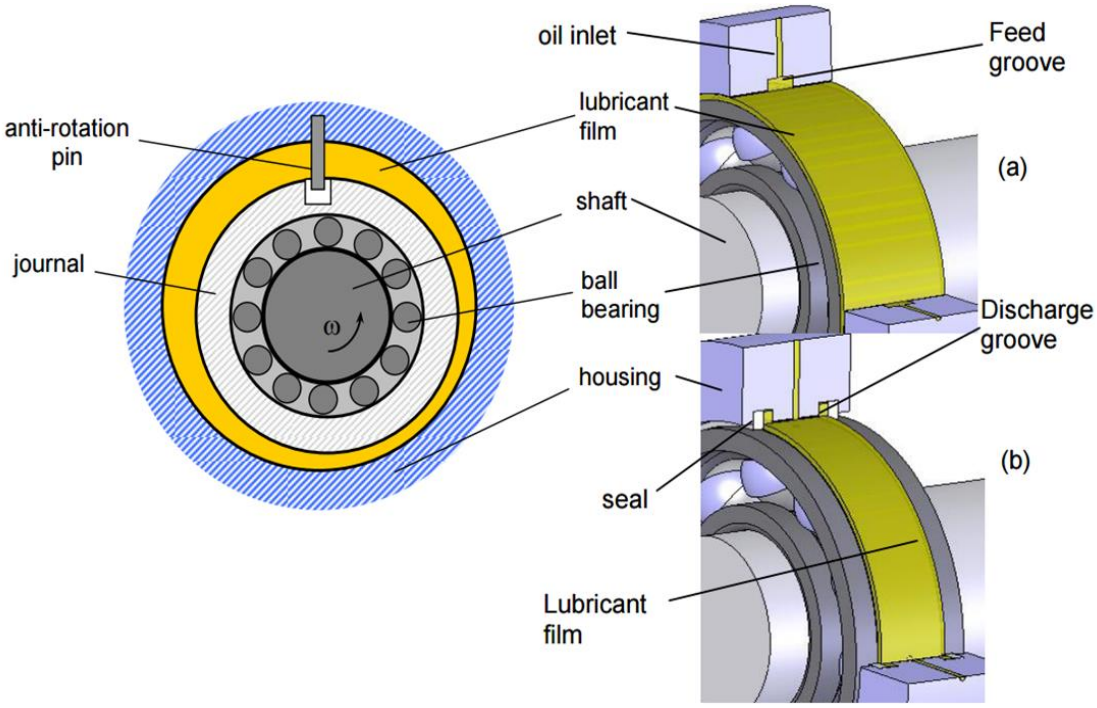

Figure 1. Squeeze film damper (SFD) configuration. a) SFD with central feed groove. b) SFD with end grooves and seals [2].

The squeeze film reaction force exerted on the journal depends on many factors, namely the lubricant feeding mechanisms, diameter, film length (L), clearance (c), type of end seals, and operating conditions [2]. Currently, industry prefer simpler designs having a low footprint to reduce cost, maintenance, weight, and space while pushing for higher operating speeds to increase power output. As a result, research devotes to determining the effects of shortening damper length, reducing film clearance, employing seals,...etc.

on a SFD dynamic forced response [1, 5, 6]. Other studies, on the other hand, may investigate the effects of various operating conditions such as a large orbit amplitude or a large static eccentricity (emanating from increased rotor flexibility at higher speeds) on the dynamic forced performance of SFDs.

Statement of Work

The main task evaluates the dynamic force performance of a simply configured damper, that is: open-ends, short-length (L/D=0.2), no central groove, no end grooves (provisions for end seals), a nominal radial clearance c_1=0.267 mm (c_1/R=0.004), and with three lubricant feedholes spaced 120° apart. This SFD configuration marks the simplest examined to date in a series of experiments on the same SFD test rig used in this thesis [7-12]. The results are pertinent to an aircraft engine manufacturer (sponsor of the work) and the SFD configurations closely resemble those used in an aircraft engine. In controlled tests, the SFD test rig undergoes a circular whirl path with orbit amplitude r=0.05c_1 to 0.71c_1, and departing from various static eccentricity; e_s=0c_1 (centered) to 0.86c_1, a largely off-centered position. Recorded displacements, accelerations, and dynamic loads lead to estimate the SFD force coefficients $(\mathbf{K}, \mathbf{C}, \mathbf{M})_{SFD}$. Recorded dynamic film pressures evidence the occurrence (or lack thereof) of air ingestion or fluid oil/vapor cavitation phenomenon. Comparisons of the SFD force coefficients against predictions from simple formulas based on the short-length SFD open-ends model [2] and predictions from a computational orbit-based model developed in Refs [13-15] strive to evaluate the accuracy of the predictive models.

Comparisons of the experimental results with those of damper configurations examined in prior art [10-12] will improve SFD design practices as industry continually pushes for simpler designs and higher operating speeds. Identified force coefficients and measured fluid film pressures for the current damper (#1) are compared with those of two prior examined dampers, one with ~half the clearance, c_2=0.122 mm (damper 2), and one with nearly equal clearance c_3=0.254 mm (damper 3) and configured with end grooves (thus a longer wetted length L_{eff}).

CHAPTER II

LITERATURE REVIEW

Background

The investigation of SFDs first began in the late 19th century with the idea of using a fluid film to ameliorate detrimental vibrations in mechanical systems. Nikolajsen and Holmes [16] traced early industrial applications of SFDs to an 1889 C. A. Parsons and Company machine in which a fluid film aided to support bearings in a steam turbine, and to a 1939 Brown Boveri turbocharger that incorporated SFDs. Della Pietra and Adiletta [5] report that US patents issued in 1933 and 1948 depict concepts that resemble modern day SFDs. In the 1960s, the use of SFDs experienced a boom and became prominent in rotating equipment, in particular gas turbine engines. As a result, substantial research and development emerged and sought to improve and predict the performance of SFDs [17]. Cooper [18] in 1963 performs the first concerted experimental investigation of SFDs as a mechanism to reduce the amplitude of rotor vibrations due to imbalance.

Zeidan, San Andrés, and Vance [1] (1996) thoroughly review the industrial motives leading to the design and use of SFDs. The authors provide practitioners with numerous and comprehensive design aspects that affect the performance of SFDs, such as geometry (length, diameter, and radial clearance), lubricant viscosity and fluid inertia, supply pressure, feeding and discharge flow mechanisms, type of end seals, and even two-phase flow regimes. Lastly, the authors discuss and suggest SFD design practices for operation in commercial turbomachinery to the date.

The ensuing literature review outlines chronologically research performed on key aspects in SFD design and modeling relevant to the current study: SFD configurations, fluid inertia effects, parameter identification techniques, cavitation and air ingestion, and performance of SFDs undergoing off-centered orbital motions.

Typical SFD Configurations

Aircraft engine manufacturers explore new squeeze film damper (SFD) design spaces with the generation of benchmark empirical data as part of on-going efforts to develop and market advanced aircraft gas turbine engines. In general, SFD configurations fall within two categories, those with a centralizing spring element, and those where the rotor rests on the housing [19]. SFDs may also vary in their lubricant feeding, sealing mechanisms, and film land length. Seshagiri [7], Mahecha, [8], San Andrés and Seshagiri [9] provide comprehensive experimental results on the dynamic force performance of (piston-ring-sealed) SFDs with diverse film land lengths and clearances. Note that experiments conducted in the above studies took place on the same test rig as the one used in this thesis, and pave the way for the investigation of short-length open-ends SFDs. The remainder of this review, however, addresses only damper configurations relevant to this thesis: elastically supported, hole fed, open-ends SFDs.

There are two commonly used lubricant feeding mechanisms for SFDs: circumferential feed groove and in-film land feedholes [17]. A circumferential feed groove provides a continuous source of lubricant flow and “uniform” pressure into the film lands that aids in preventing lubricant starvation and/or cavitation. A space-saving SFD configuration uses feedholes directly impinging into the film land. Research efforts

have investigated SFDs with the latter feeding mechanism as a means to simplify the design of SFDs, reduce the effects of fluid inertia emanating from a circumferential feed groove [20, 21], and provide, theoretically, up to four times more damping than SFDs with a circumferential feed groove (and same land length) [22]. As a result, the tasks defined in this thesis intend to further understand the performance of SFDs with a hole-fed configuration.

Marmol and Vance [17] in 1978 and Chen and Hahn [22] in 1994 examine SFDs configured with feedholes. Findings from these early studies reveal that there are fluctuations generated in the film land pressures for hole fed SFDs in contrast to the uniform pressure assumed in groove fed SFDs [17]. Moreover, the pressure distribution within a feedhole shows its nature as a "source" potential-flow element [22].

Defaye et al. [23] (2006) experimentally compare the radial (inertia) and tangential (damping) SFD forces in a sealed-ends SFD with either a central-groove or three orifice feedholes, and with various lubricant supply pressure and inlet temperature. The authors find that an orifice feedhole configuration generates the largest tangential (damping) force and radial force while the circumferential feed groove configuration generates the lowest tangential force. Moreover, oil cavitation occurs at lower orbit journal amplitudes of motion for a feedhole configuration than for a circumferential groove configuration.

In 2013, Bradley [11] presents comprehensive comparisons (experimental and predictions) between SFDs with lubricant feedholes and SFDs with a circumferential feed groove. Note that the experimental work was performed using the same test rig as in this thesis and provides a basis for comparison of experimental findings. The tests conducted comprise of circular centered orbits of the SFD with various amplitudes. Comparisons of

damping coefficients between a SFD with a circumferential feed groove and a SFD with feedholes show that both dampers offer similar damping coefficients, albeit damping for the hole-fed SFD appears more sensitive to the journal static eccentricity. On the other hand, the grooved damper shows at least ~60% larger inertia force coefficients. Furthermore, measured fluid film pressures show that the static pressure distribution around the circumference of the SFD is not uniform; rather it is largest at the location of the feedhole and smallest at halfway between two feedholes. Thus, Bradley promotes the benefits of SFDs configured with feedholes, namely a reduced weight and size, comparable damping, and avoidance of fluid inertia effects associated with the feed groove [20, 21, 29, 30] (discussed in the following section). The tradeoff, however, is that the fluid film static pressure is not uniformly distributed throughout the circumference of the SFD, and could facilitate oil cavitation.

Fluid Inertia Effects

The effect of fluid inertia on SFD dynamic force performance manifests as added mass coefficients of significant magnitude. Classical lubrication theory assumes fluid inertia as negligible in a thin fluid and delivers the Reynolds equation governing the hydrodynamic pressure generation in the fluid film [24]. A plethora of research, however, demonstrates that this remains an over simplification and that fluid inertia has a significant role in the dynamic force performance of SFDs. Moreover, predictive models based on classical lubrication theory often deviate from experimental results, usually due to the exclusion of fluid inertia effects in the models.

Efforts to understand fluid inertia effects of lubricant in fluid film bearings can be traced back to as early as the 1960's [25].

In 1975 Reinhart and Lund [26] find that the fluid film inertia coefficients in a long-length damper can be several times the mass of the journal itself. The authors warn that the large inertia coefficients may affect the rotordynamics of turbomachinery. Next, Tichy [27, 28] (1982-1984) studies the influence of fluid inertia on SFD forced response to circular centered motions and presents experimental results demonstrating that fluid inertia causes a large increase in pressure, a change in the shape of the dynamic pressure curve, and a phase shift of the pressure peak in the direction of the whirl motion. The author finds that increasing the eccentricity ratios produces squeeze film Reynolds numbers ($Re_s = \rho\omega c^2 / \mu$ where ρ denote the fluid density, μ the fluid viscosity, ω the whirl frequency, and c the film radial clearance) up to 13. This is a significant finding since fluid inertia stood largely disregarded at the time (or in some cases not even thought to exist). Current knowledge states that fluid inertia must be accounted for when $Re_s > 12$ [24]. Tichy states that his model with fluid inertia effects produces damper forces (and pressures) in better agreement with experimental measurements than does a model without fluid inertia effects.

San Andrés [29] (1985) further studies the effects of fluid inertia on SFD performance and finds that large squeeze film Reynolds numbers can be achieved during SFD operation, particularly for circular centered motions with small orbit radii. San Andrés also demonstrates that at low squeeze film Reynolds numbers ($Re_s \approx 1$), viscous forces mostly dominate the damper forced performance, while at large squeeze film Reynolds numbers ($Re_s \geq 10$), inertial forces dominate the SFD forced performance. This

leads the author to create a predictive model including convective and temporal fluid inertia terms that determines the SFD force coefficients for operation with circular centered journal motions. San Andrés' model serves as the basis of the orbit-based model [15] used in this thesis.

Arauz [30] (1993) extends the knowledge on fluid inertia by experimentally investigating a centrally grooved SFD undergoing whirl motions with an increasing whirl frequency, as well as configured with various groove depths. Consistent with findings by San Andrés [29], the circumferential feed groove exhibits significant levels of dynamic fluid pressure, particularly for damper configurations with small groove depths. Radial forces of the same magnitude as those developed at the groove are determined in the film lands where the film thickness is considerably smaller. The author suspects that the circumferential groove creates an inertia effect on the adjacent film lands. In addition, experiments show that the significance of the radial (inertial) force is slightly larger at the groove than at the land. The author finds that the deeper the groove, the smaller the dynamic film land pressures, and the larger the Reynolds number and fluid inertia. On the other hand, the smaller the groove depth, the more significant the dynamic film land pressures and damping capacity.

Parameter Identification and SFDs Theoretical Models

There exist several experimental parameter identification techniques to evaluate physical parameters (e.g. force coefficients) in mechanical systems. Typically, however, methods that effectively reduce error due to noise while maintaining high computational

efficiency merit the most recognition. The following literature review discusses techniques and methodology incorporated in the current experimental procedure.

Tiwari, Lees, and Friswell [31] review methods of identifying bearing parameters in the time and frequency domains and expound on the most recent parameter identification techniques developed. The authors discuss assumptions and governing equations of bearing models as well as parameter identification algorithms.

Fritzen [32] (1986) introduces the Instrumental Variable Filter Method (IVFM) to identify parameters for vibrating systems from data containing measurement noise. Fritzen's method, a variation of the least squares estimation, iteratively builds a force coefficient matrix of the stiffness, damping, and mass coefficients (*K*, *C*, *M*). Iterations reduce the measurement error until satisfaction of a residual error criterion. The author also expounds on the efficiency of the method, as it generally takes no more than four iterations to estimate parameters. In comparison with other existing methods to the date, Fritzen finds that the IVFM produced the most accurate and consistent results with reasonable computational time.

In 2010, Delgado and San Andrés [13] present a linear fluid inertia bulk-flow model for determination of SFD force coefficients for dampers configured with end-seals. This model greatly improves on previous models by incorporating the use of an effective groove depth and an effective clearance obtained from computational fluid dynamics (CFD) analysis. As noted in the previous section, SFDs with various sealing and feeding mechanisms often include grooves in the film land that amplify fluid inertia effects. A comparison of experimental and predicted results shows that the groove effective depths are approximately half of the actual groove depth while the penetration depth of the

streamline dividing the flow regions is approximately 1/5 of the actual groove depth. By incorporating the effective groove depth and clearance, results from the authors' model drastically improve the agreement between experimental and predicted added mass coefficients. The findings thus show that SFD force coefficients appear as strong functions of its geometry and that correct modeling of fluid flow paths in SFDs proves critical in accurately predicting the SFD force coefficients. As a result, the analysis in this thesis incorporates similar principles in the investigation of a SFD with end grooves.

Oil Cavitation and Air Ingestion in SFDs

Lubricant cavitation and air ingestion, common in SFDs, cause the fluid in the film land to rupture and become two-phase in regime, and often lead to adverse effects on the generation of dynamic pressures. It is important to note, however, that air entrainment and gaseous cavitation are distinct phenomena. Air ingestion commonly occurs in SFDs with ends open to ambient pressure such as those investigated in this thesis. In brief, as the film thickness increases locally, it produces a suction pressure at the end of the film land, drawing air into the film or gap. On the other hand, cavitation takes place when the film dynamic pressure reaches below the fluid saturation pressure and either (rarely both [2]) dissolved gases in the lubricant become liberated (gaseous cavitation), or lubricant vaporizes and forms a local cavity (vapor cavitation) [33].

Due to the complex behavior of a two-phase flow and its adverse effects on SFD forced performance, research continues to improve models to predict cavitation and air ingestion.

Walton et al. [34] (1987) present, for the first time, high-speed camera photographs of SFDs operating with gaseous cavitation. Walton et al. investigate two different damper feed configurations, namely, feed groove and feedholes. The high-speed photos show marked differences in the cavitation region for a groove fed SFD and for a hole fed SFD. For SFDs with feedholes, the film rupture zone is strongly influenced by the hole geometry and is not repeatable from cycle to cycle, unlike the grooved damper. The analysis shows that feedholes may act as a sink when the film land pressure becomes greater than the feedhole supply pressure.

Zeidan and Vance [35-37] (1989) in a series of experiments investigate the occurrence and extent of air ingestion and gaseous cavitation by also employing high-speed photography to capture images and videos of the fluid flow in a SFD whirling at a centered position. In their study, the whirl frequency, journal static eccentricity, supply pressure, and use of end seals influences the cause and extent of cavitation. In particular, at low whirl speeds, the fluid film shows no cavitation; at high speeds, the fluid film enters a two-phase regime; and at intermediate speeds, signs of cavitation occur. The oil cavitation in turn has an effect on the generated squeeze film dynamic pressure and resulting force coefficients. Next, the authors investigate SFD operation under conditions where air entrainment is dominant and find that it produces a nonlinear decrease in the film stiffness coefficient not previously known to exist in squeeze film dampers. The authors note that the use of end seals can significantly reduce the amount of air entrainment in the lubricant film.

In 2001, Diaz and San Andrés [38, 39] study a short-length, open-ends SFD undergoing circular centered orbits with air entrainment. The authors introduce the feed

squeeze flow parameter $\gamma = \frac{Q_{in}}{\pi DLr\omega}$, a relationship to predict onset of air ingestion, where ω denotes the whirl frequency, r the journal orbit amplitude, L the journal length, D the diameter, and Q_{in} the lubricant flow rate supplied to the damper. Essentially, the feed squeeze flow parameter describes the ratio between the lubricant supply flow-rate and the rate of volume change due to squeeze motion of the journal. While γ>1, the supply flow rate is sufficient to fill the volume change due to squeeze and no air ingestion will occur. Vice versa, when γ < 1, air ingestion will occur. Thus, air ingestion is more likely to occur at a large orbit amplitude, r, and at a high whirl frequency, ω, as confirmed by experimental data. A further study by Mendez et al. [40] (2010) extends Diaz and San Andrés [38, 39] squeeze flow parameter (γ) to finite length bearings by solving via finite elements the Reynolds equation. The authors find that a uniform lubricant feed pressure condition produces results most similar to experimental results for long land-length dampers but note that, contrary to Diaz and San Andrés' findings, air entrainment occurs up to γ=2 when using a uniform feed pressure condition.

Younan et al. [41] (2011) study numerically the effects of air entrainment on SFD dynamic performance by introducing to the Reynolds equation the viscosity and the density of an air/lubricant mixture, which are themselves functions of the air/oil volume and mass fraction. The authors benchmark their model against experimental results from Tao et al. [42] which also defined lubricant viscosity as a function of the volume fraction. Results from Younan et al's study confirm that as the air/oil mass ratio increases, the developed hydrodynamic pressure decreases. Consequently, the magnitude of the nonlinear forces and resulting load capacity of the SFD decrease as the mass ratio of

air/oil increases in the lubricant. Furthermore, increasing the air/oil mass content leads to undesirable increases in the journal orbit amplitude.

Gehannin, Arghir, and Bonneau [43] (2015) develop an improved numerical model for SFDs operating with both air ingestion and cavitation. The model incorporates the Rayleigh Plesset equation for modeling of cavitation, and models an air bubble via a volume of fluid and computational fluid dynamics (CFD) approach. By further considering that the air bubble is subject to time variation of the local pressure, the authors introduce a bubble pressure and a (bubble) surface dilatation viscosity term. Comparisons of the predicted results against experimental results from Adiletta and Pietra [44] show good agreement for the extent of vapor cavitation and its pressure magnitudes, and evidence the importance of bubble pressure and the dilatation viscosity on lubricant cavitation phenomenon. Predicted pressure profiles demonstrate the cavitation pressure is a low-pressure zone usually close to the absolute zero pressure. The pressure profiles also demonstrate air ingestion as a zone of almost constant pressure located between the minimum (absolute zero) and the maximum pressures in the profile, and with magnitude close to the atmospheric/exit pressure. Such observations coincide with earlier observations advanced in Ref. [2], the observations in numerous experiments performed on the test rig used in this thesis [7-12], as well as the observations in a bevy of other experimental studies of SFDs.

SFDs Operating At a Large Static Eccentricity

The experiments performed in this thesis include operating conditions that produce slightly to moderately off-centered circular whirl motions. These conditions often exist in

aircraft engine operation when events such as maneuver loads, sudden loss of lift due to air turbulence, and blade loss that instantaneously increase the load exerted on the rotor to perform large amplitude or large eccentric motions [45]. SFDs supported on a squirrel cage can easily bottom out during these events and increased transmitted forces to the engine support structure may cause component fatigue and failure.

Research focusing on the eccentric operation of squeeze film dampers first began with Pan and Tonessen [45] in 1978. The authors model rotor orbits with a large static eccentricity due to a large static pre-load (causing an offset between the rotor and bearing center of masses). The authors also apply the short-length bearing assumption, and examine the dynamic performance of a rigid rotor in the presence of a static load. The fluid film pressure is determined via the half-film (π) assumption or the full-film (2π) assumption, and used to calculate the fluid-film forces. For the π-film assumption, the vibrations from an imbalance response tend to force the motion into a large orbit.

San Andrés and De Santiago [46] (2004) determine experimentally SFD force coefficients of an open ends SFD operating with both circular and off-centered centered whirl orbits. The damping coefficients for small amplitude motions remain nearly constant for increasing static eccentricity, but increase with increasing orbit amplitude. On the other hand, the inertia coefficients are small for all orbit amplitudes and static eccentricities.

Adiletta and Della Pietra [44] (2006) investigate the distribution of lubricant pressure in a SFD undergoing eccentric whirl orbits. The experiments consider a centered position and two eccentric positions: slightly and moderately off-centered eccentricity of the journal bearing. Measured dynamic film pressure profiles at the three starting

positions exhibit noticeable differences. Additionally, the authors' theoretical predictions match the experimental results for operation at low static eccentricities provided adequate lubricant supply pressure delivered, and a full film condition (no cavitation) assumed in the model. At an off-centered position, the authors note significant differences in the amplitude and shape of measured pressure profiles at varying circumferential locations. Likewise, the behavior of the lubricant film depends on the type of cavitation, gaseous or vapor, whose prevalence and extent depends on the degree of off-centeredness.

Recently, Jeung [12] in 2013, conducts experiments using the same SFD test rig as that in this thesis that include whirl motions departing from static eccentricity up to e_s/c=0.75. Identified damping coefficients show a non-linear increase with static eccentricity while identified added mass coefficients show a slight increase with static eccentricity. The reported relationships between SFD force coefficients and static eccentricity provide a basis for comparison against those from experiments conducted in this thesis.

Summary

The reviewed literature provides a background for the experimental procedure and observations in experiments performed in this thesis. Various test SFD configurations show the evolution of SFD design, with the inclusion or lack thereof of features such as seals, grooves, or feedholes. The work in this thesis investigates a simply-configured SFD that does not include seals and grooves altogether as industry strive for simpler designs.

Much of fluid inertia effects reported in literature pertain to whirl motions with small to moderate orbit amplitude about a centered to slightly off-centered position [29,

30]. The work in this thesis furthers the investigation by identifying fluid film added mass coefficients in a SFD whirling with a large amplitude, departing from largely off-centered positions, and operating with squeeze film Reynolds number $Re_s < 12$.

Improving the modeling and prediction of SFD fluid film pressure dynamics, cavitation phenomenon, air ingestion, continues to this day with much needed experimental validation. The work in this thesis contributes to the endeavors by experimentally recording *peak-to-peak* pressures and fluid film pressure profiles over various operating conditions.

Lastly, a multitude of experiments [7-12] performed on the same test rig in this thesis delivered findings pertinent to an aircraft engine manufacturer and sets the stage for the relentless analysis of simpler SFD configurations to meet industry demands.

CHAPTER III

SFD KINEMATICS AND THE SHORT-LENGTH SFD MODEL

Coordinate System

Figure 2 shows a schematic representation of a lubricated film clearance between a journal and its housing. Θ defines an absolute (fixed) angular coordinate, while $\theta=\omega t$ designates a rotating coordinate with its origin at the location of maximum film thickness (h) and where ω denotes the whirl frequency in rad/s.

The distance between the journal instantaneous center position ($O_{J\text{-}dyn}$) and the bearing cartridge (BC) center position (O_{BC}) constitutes the instantaneous eccentricity (e), while the distance between the journal orbit center, i.e. journal static position ($O_{J\text{-}s}$) and the bearing cartridge center position (O_{BC}) establishes the static eccentricity (e_s). The journal center ($O_{J\text{-}dyn}$) whirls along the orbit path about $O_{J\text{-}s}$ with amplitude $r_X=r_Y$. Hence,

$$\begin{aligned} \vec{e} &= \vec{e}_s + \vec{r} \\ \left|\vec{e}\right| &\le c \end{aligned} \tag{1}$$

where c denotes the SFD radial clearance. Note that in the figure, the journal is not drawn to scale (smaller), while the lubricant film is greatly exaggerated. The film thickness equals:

$$h = c + \left[\underbrace{\left(e_{s_X} + r\cos(\theta)\right)}_{e_X(t)} + \underbrace{\left(e_{s_Y} + r\sin(\theta)\right)}_{e_Y(t)} \right] \tag{2}$$

where (e_{s_X} , e_{s_Y}) , and r denote the static eccentricity and amplitude of the journal whirl motion, respectively.

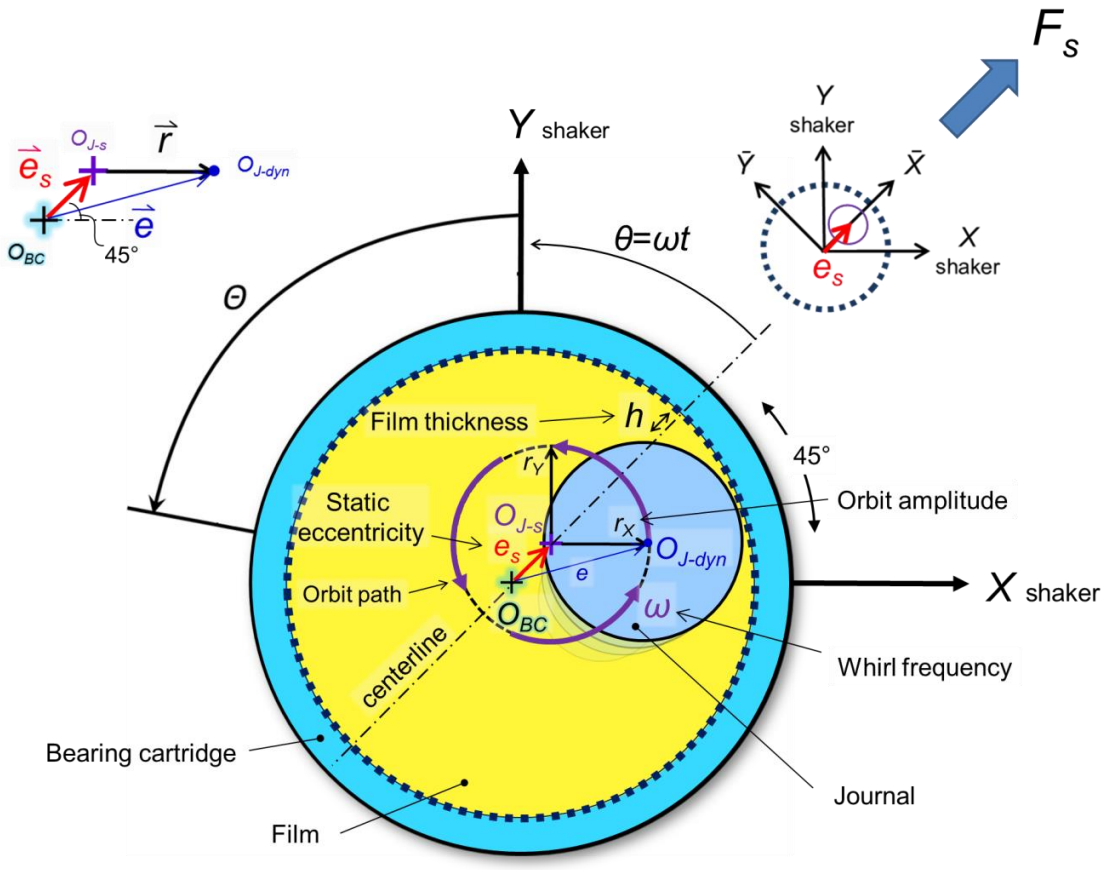

Figure 2. Schematic view of a lubricated film clearance between a journal and its housing, coordinate system, and kinematic parameters.

Representation of SFD Reaction Forces to an Externally Applied Load

Figure 3 depicts a schematic view of the SFD structure (*S*) and fluid film bearing (*SFD*) represented via spring (**K**), dashpot (**C**), and added mass (**M**) elements.

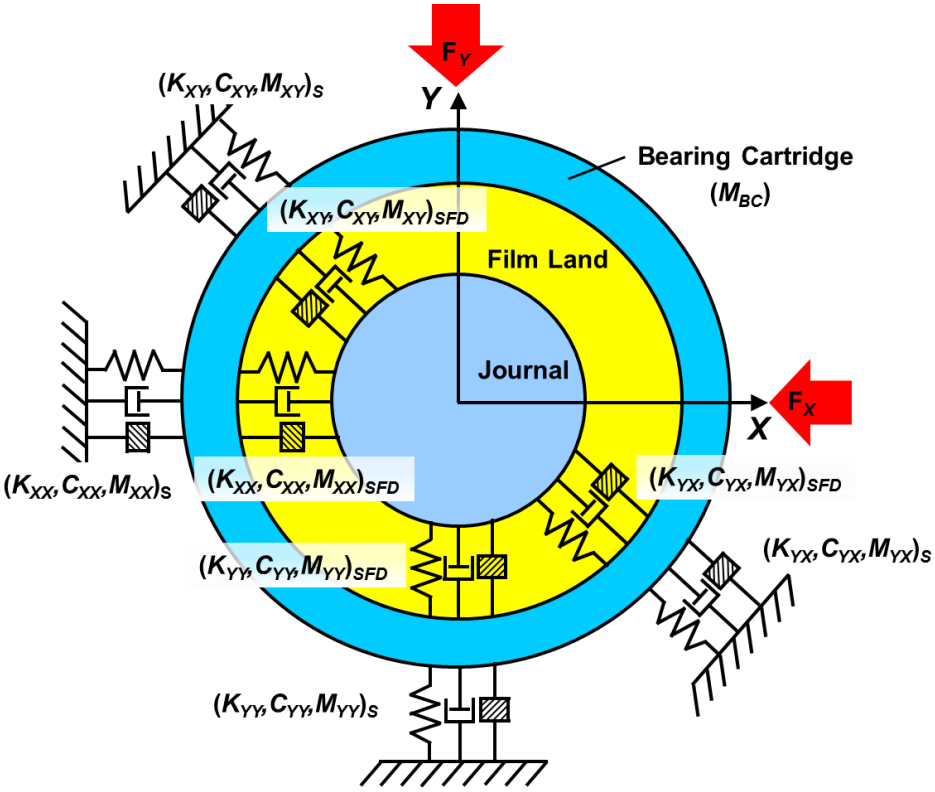

Figure 3. SFD structure (*S*) and fluid film bearing (*SFD*) represented via spring (K), dashpot (C), and added mass (M) elements [12]

Simple Formulas for SFD Force Coefficients

Given that the *X*,*Y* axes are 45° way from the static eccentricity (e_s) (see Figure 2), the short-length (open-ends) SFD model [2] states the linearized direct damping (C) and added mass (M) coefficients from a journal performing small amplitude circular whirl motions (thus no oil cavitation – 2π film) about static eccentricity ($\varepsilon_s = e_s/c$) as:

$$C_{XX} = C_{YY} = \frac{\pi \mu D}{4}\left(\frac{L}{c}\right)^3 \left\{\frac{1+2\varepsilon_s^{\,2}+(1-\varepsilon_s^{\,2})^{1/2}}{\left(1-\varepsilon_s^{\,2}\right)^2}\right\} \tag{3}$$

$$M_{XX} = M_{YY} = \frac{\pi \rho D}{24}\left(\frac{L^3}{c}\right)\left\{\frac{1}{\left(1-\varepsilon_s^{\,2}\right)^{1/2}}\right\} \tag{4}$$

See Appendix A for the derivation of the damping and added mass formulas. Note that the model delivers M_{XY}=M_{YX} that are effectively nil for motions in the range $e_s/c_1 < 0.86$.

The short-length (open-ends) SFD model also presents the direct damping and added mass coefficients for a journal performing circular centered (e_s/c=0) orbits (with no oil cavitation – 2π film) as a function of the orbit amplitude $\bar{r} = r/c$ [2]:

$$C_{tt} = \overline{C}^{CCO}_{XX} = \overline{C}^{CCO}_{YY} = \frac{\pi\mu D}{2}\left(\frac{L}{c}\right)^3 \left\{\frac{1}{\left(1-\bar{r}^2\right)^{3/2}}\right\} \tag{5}$$

$$M_{rr} = \overline{M}^{CCO}_{XX} = \overline{M}^{CCO}_{YY} = \frac{\pi\rho D}{12}\left(\frac{L^3}{c}\right)\left[1-2(1-\bar{r}^2)^{1/2}\right]\left\{\frac{(1-\bar{r}^2)^{1/2}-1}{\bar{r}^2(1-\bar{r}^2)^{1/2}}\right\} \tag{6}$$

The model also reveals C_{XY}, C_{YX}, M_{XY}, and M_{YX} are effectively nil [2]. Note that the direct damping and added mass coefficients would be half the values given by Eqns. (5, 6) for a model with cavitation (π film).

Notice that the above relations derived from the short-length (open-ends) SFD model depend strongly on the SFD geometry (i.e. L, D, c). In addition, the coefficients are valid for squeeze film Reynolds number $Re_s = \rho\omega c^2/\mu < 10$ [2]. The Re_s for the current damper operating with frequency f=10-100 Hz are 1.4-12.5, respectively, and mostly within the range of validity for the force coefficients. Ref. [2] also provides an adjustment factor α to the force coefficients for Re_s up to 50. It is important to point out, however, that the above relations, Eqns. (3-6), ignore any feedhole, size, number and their disposition in the damper.

CHAPTER IV

EXPERIMENTAL PROCEDURE

Test Rig Mechanical Assembly

Figure 4 depicts the SFD test rig, its support structure, two electromagnetic shakers, and a hydraulic static loader. The two shakers orthogonally positioned along the *X* and *Y* axes connect, through slender stingers, to the bearing cartridge (BC) for delivery of dynamic loads at a specified frequency and amplitude to displace the BC about the stationary journal. Note that this relative motion between the BC and journal, $\mathbf{z}_{dyn}$, is analogous to the kinematics presented in Figure 2. The hydraulic static loader positioned 45^{o} away from the *X* and *Y* axes statically displaces (pulls) the BC to an off-centered (eccentric) position. The reasoning behind exciting the BC into performing whirl motions, as opposed to a spinning rotor plus journal, lies in its simplicity in implementation and control.

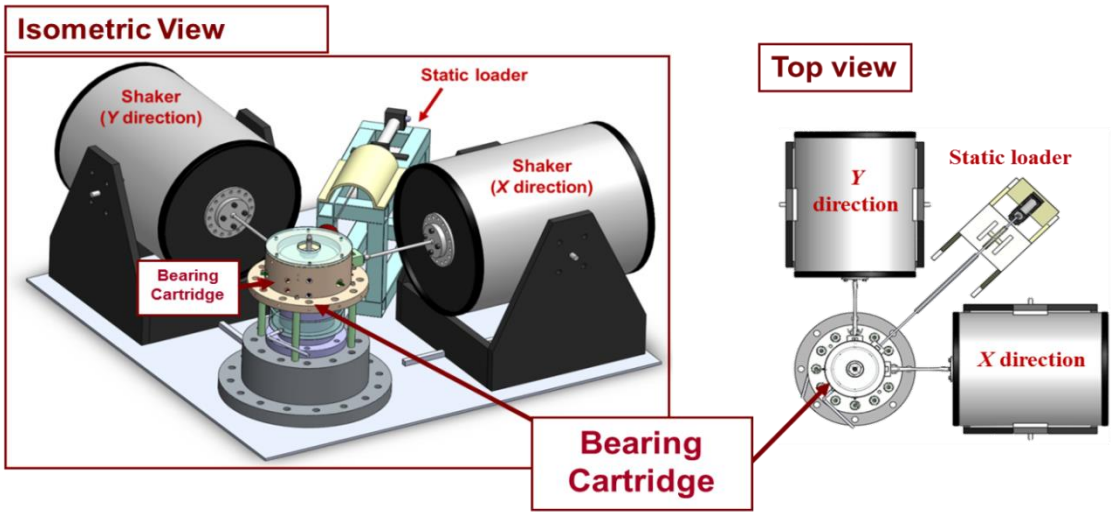

Figure 4. Schematic view of the SFD test rig (isometric and top views).

The test journal is centered and bolted using a torque wrench set to 364 N·m. Four structural rods support the bearing cartridge with mass M_{BC}=15.15 kg. The rods provide a structural stiffness K_S~12 MN/m along the static load direction and ensure concentricity with the journal at zero static load. Appendix B details the measurement of the test rig structural stiffness.

The shakers in the *X* and *Y* directions deliver a single-frequency dynamic load to the BC to produce whirl motions with amplitude $r_X=r_Y$ (circular). Motion of the BC results from two linearly-independent load vectors, $\mathbf{F}_1$ and $\mathbf{F}_2$, imposed on the BC with a 90° ($\pi/2$) phase difference between them to produce clockwise and counterclockwise whirl motions[1], respectively:

$$\mathbf{F}_1 = \begin{bmatrix} F_{X_1}\cos(\omega t) \\ F_{Y_1}\sin(\omega t) \end{bmatrix}$$
$$\mathbf{F}_2 = \begin{bmatrix} F_{X_2}\cos(\omega t) \\ -F_{Y_2}\sin(\omega t) \end{bmatrix} \quad (7)$$

where ω represents the excitation frequency (Hz). Circular orbits have equal amplitude of load ($F_X=F_Y$) along the *X*, *Y* directions to produce BC whirl motions with amplitude $r_X=r_Y$. Again, the relative motion between the BC and the journal simulates actual SFD operation in which the journal whirls inside the bearing housing.

Test Rig Lubrication System

A lubrication pump-sump system circulates lubricant through the test rig. Figure 5 depicts the lubricant flow path. Lubricant enters the journal with a designated supply

[1] For clarification, $\mathbf{F}_1$ and $\mathbf{F}_2$ pertain to separate sets of experiments, a clockwise whirl orbit and a counter-clockwise whirl orbit, respectively.

pressure (P_{in}) through a vertical cavity in the journal, then flows radially through three feedholes, with diameter ϕ=2.54 mm, spaced 120° apart, to the damper film land, then exits the film land at its top and bottom ends at ambient pressure. The test rig maintains a lubricant flow rate Q_{in}=5.1 LPM, as measured by a turbine flow meter upstream of the damper. This flow rate is consistent among the various test damper comparisons [10-12]. The supply pressure required to maintain the flow rate is P_{in}~0.36 bar, as measured by a Bourdon-type pressure gauge. Note that the selected flow rate of 5.1 LPM and supply pressure P_{in}~0.36 bar suffice for minimizing lubricant starvation during operation with large orbit amplitudes for the current damper configuration (see feed-squeeze flow parameter γ in Ref. [39]).

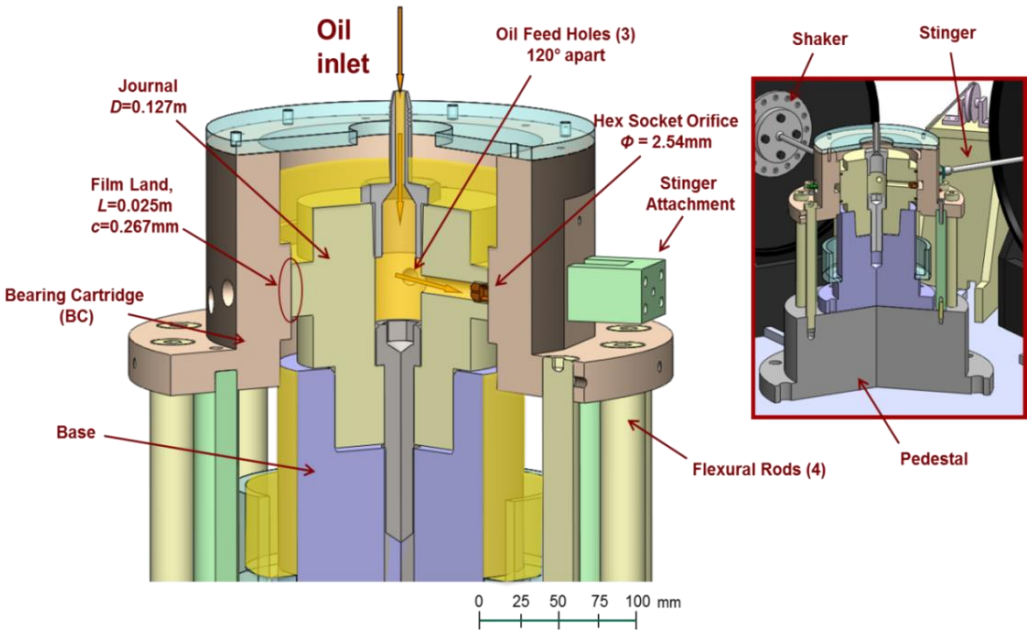

Figure 5. Cut-section view of the SFD test bearing section [12].

The lubricant used is ISO VG2, a light lubricant having measured viscosity μ=2.65 mPa·s and density ρ=802 kg/m^3 at a temperature T=19.5°C. Assuming isothermal operation due to the damper having open-ends, the kinematic viscosity of the ISO VG 2

oil represents that of lubricants used in aircraft engines operating at a high temperature. Appendix C contains measurements of the lubricant viscosity and flow conductance (inverse of the resistance of the lubricant flow through the orifice and film land).

Test Rig Instrumentation

The SFD test rig uses a myriad of sensors to measure various operation parameters and fluid film properties. The sensors comprise of displacement eddy current sensors, accelerometers, load cells, pressure sensors, and flow measurement sensors, among others. Table 1 lists only the instrumentation pertinent to the experiments in this thesis.

Table 1. SFD test rig instrumentation

Sensor	Manufacturer	Sensitivity*	Measurement Variable
Proximity (Eddy Current) (2)	Bently-Nevada®	0.8 V/mil (31 mV/μm)	Bearing Cartridge displacement with respect to journal along *X* and *Y* axes
Accelerometer (2)	PCB®	105 mV/g	Bearing accelerations along *X* and *Y* axes
Piezoelectric pressure sensor (6)	PCB®	10 mV/psi** (145 mV/bar)	Dynamic pressure along film land for varying axial positions *Z*
Piezoelectric load cell (2)	PCB®	10 mV/lbf (2248 mV/kN)	Dynamic load on BC applied by shakers along *X* and *Y* axes
Strain-gage type pressure transducer (1)	Omega®	0.05 mV/psi (0.73 mV/bar)	Lubricant supply pressure prior to entering journal
Strain gage type load cell (1)	Omega®	0.04 mV/lbf (9 mV/kN)	Magnitude of static load applied on bearing cartridge to generate off-centered operation
Flowmeter	Omega®	-	Lubricant supply flow rate prior to entering journal

*Listed in English units per manufacturer specifications.

*Varies.

Bently Nevada REBAM® eddy current sensors installed in the BC record the relative displacement (x, y) between the BC and journal along the X,Y-axes. PCB® accelerometers attached to the BC record the BC absolute acceleration (a_X, a_Y) along the X,Y directions. Load cells attached to the shaker excitation stingers record magnitude of the dynamic excitation force (F_X, F_Y). Dynamic pressure sensors installed around the BC record damper film land pressures (P) for identification and analysis of lubricant cavitation and air ingestion. A strain gauge type load cell measures the force applied to statically offset the BC along the 45° direction.

Note that the test data obtained for operation of the SFD with a moderately large amplitude ($r/c_1 > 0.29$) is limited to excitation frequency $f \leq 100$ Hz since the magnitude of the dynamic load exerted by the shakers often exceeds the load cell's rated linear range of 0-2.23 kN.

Measurement of dynamic film pressures at various circumferential positions (Θ) and axial film land positions (Z) elucidates the relationship between SFD pressure generation and whirl frequency (ω), orbit amplitude (r), and static eccentricity (e_S) and air ingestion or oil/vapor cavitation. Figure 6 depicts schematic diagrams of the pressure sensor layout in the BC as well as a schematic "unwrapped" 360° side view of the BC outlining the disposition of the instrumentation. The pressure sensors, installed in the BC and distributed around its circumference, measure the fluid film pressures at different locations. Two sets of three PCB pressure sensors ($P_{1\text{-}3} - P_{4\text{-}6}$), spaced apart by 90º, record the dynamic pressure at the top, bottom, and mid sections of the damper land as shown in the figure. Note that $P_{1\text{-}3}$ and $P_{4\text{-}6}$ are spaced 15º apart. Two other piezoelectric pressure

sensors (P_7 and P_8) measure the film dynamic pressures in the end grooves or at the exit of the squeeze film land (for a SFD with no end grooves such as the current damper, 1).

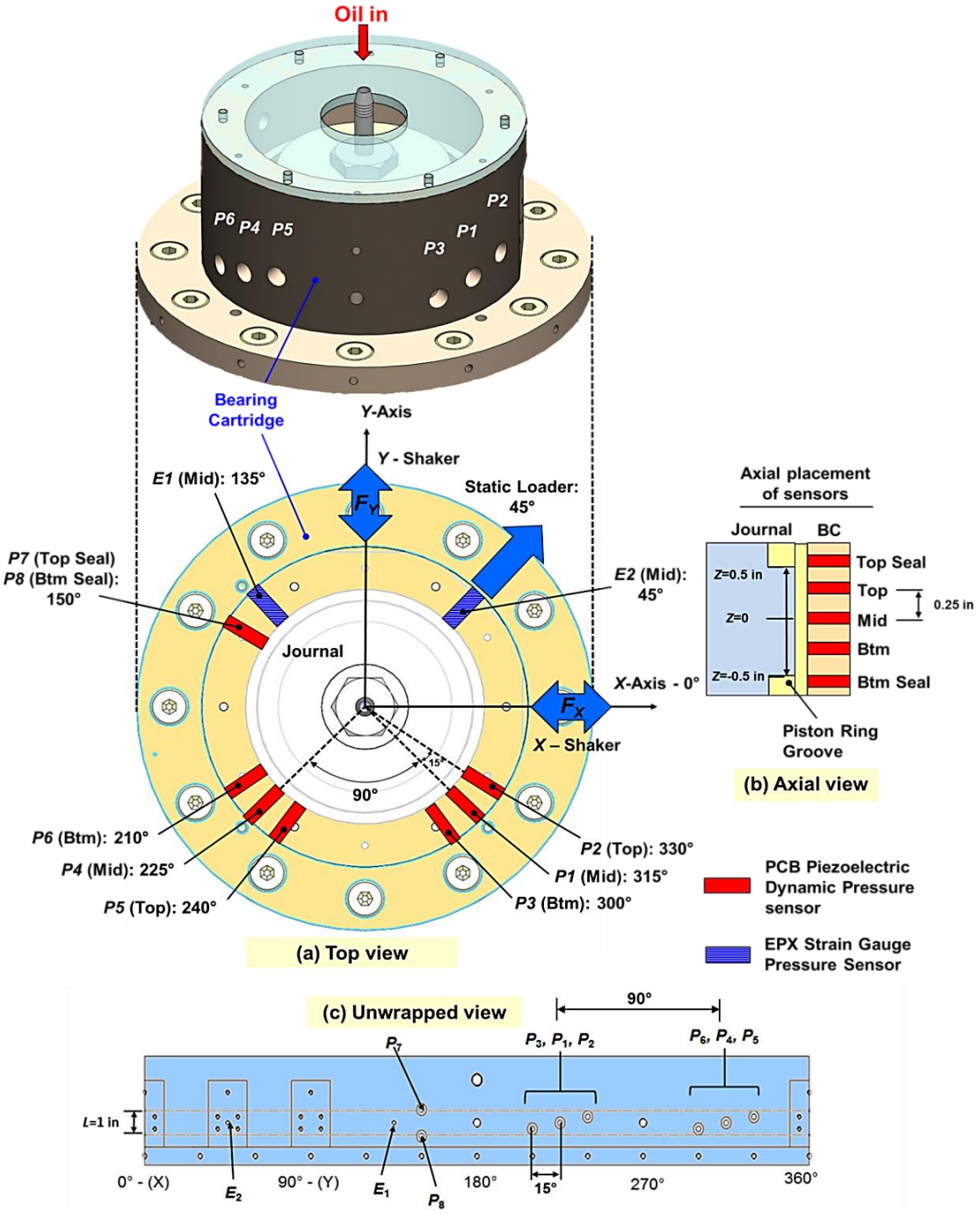

Figure 6. Schematic views of the disposition of pressure sensors in the BC: (a) top view, (b) axial view and (c) unwrapped view [11].

Test Rig Data Acquisition (DAQ) System

A cDAQ 9172 modular DAQ system continuously reads seventeen sensor output voltages to a precision of 10 μV. Next, a National Instruments LabVIEW 8.6® program acquires the voltage signals outputs them in the time domain. Additionally, within the same LabVIEW program the user specifies the frequency range, phase, and voltage amplitude to be delivered by the shakers. Thus the program both delivers the signal to the electromagnetic shakers and records voltage samples simultaneously from all sensors. After the test rig has reached a steady state at each whirl frequency, the DAQ/LabVIEW program saves data from all sensors at 16,384 samples per second for 0.25 seconds.

Test Rig Equation of Motion and Force Coefficient Identification

As shown in Figure 3 and 4, the SFD test rig can be modeled as a 2DOF mechanical system (*X* and *Y* components) with the following equation of motion (EOM):

$$M_{BC}\mathbf{a} = \mathbf{F}_{\mathbf{ext}(t)} + \mathbf{F}_{\mathbf{S}} + \mathbf{F}_{\mathbf{SFD}} \tag{8}$$

where **a** symbolizes the vector of the BC absolute acceleration. The external applied load combines the static load (F_s) applied by the static loader, and the dynamic load ($F_{(t)}$) exerted by the electromagnetic shakers, i.e.

$$\mathbf{F}_{\mathbf{ext}(t)} = \left[F_{sX} + F_{X(t)}, F_{sX} + F_{Y(t)} \right]^{\mathrm{T}} \tag{9}$$

Note $\left[F_{X(t)}, F_{Y(t)} \right]^{\mathrm{T}}$ corresponds to the dynamic load vector $\mathbf{F_1}$ or $\mathbf{F_2}$ expressed in Eqn. (7).

The structural reaction force, elements depicted in Figure 3, is governed by:

$$-\mathbf{F}_{\mathbf{S}} = \mathbf{M}_{\mathbf{S}}\ddot{\mathbf{z}} + \mathbf{C}_{\mathbf{S}}\dot{\mathbf{z}} + \mathbf{K}_{\mathbf{S}}\mathbf{z} \tag{10}$$

where $\mathbf{z} = (x, y)^{\mathrm{T}} = \mathbf{z_s} + \mathbf{z_{dyn}}$ is a vector adding the static ($\mathbf{z_S}$) plus dynamic ($\mathbf{z_{dyn}}$) displacements of the BC relative to the journal and recorded by the eddy current sensors. Note that $\dot{\mathbf{z}} = \dot{\mathbf{z}}_{\mathbf{dyn}}$, $\ddot{\mathbf{z}} = \ddot{\mathbf{z}}_{\mathbf{dyn}}$, and that $\mathbf{a} \neq -\mathbf{z}\omega^2$. Similarly, the fluid film (SFD) reaction force to a dynamic load, elements depicted in Figure 3, is governed by:

$$-\mathbf{F_{SFD}} = \mathbf{M_{SFD}}\ddot{\mathbf{z}} + \mathbf{C_{SFD}}\dot{\mathbf{z}} + \mathbf{K_{SFD}}\mathbf{z_{dyn}} \tag{11}$$

Substituting Eqns. (9-10) into Eqn. (8), the EOM becomes:

$$M_{BC}\mathbf{a} = \mathbf{F_{ext}}_{(t)} - \mathbf{M_S}\ddot{\mathbf{z}} - \mathbf{M_{SFD}}\ddot{\mathbf{z}} - \mathbf{C_S}\dot{\mathbf{z}} - \mathbf{C_{SFD}}\dot{\mathbf{z}} - \mathbf{K_S}\mathbf{z} - \mathbf{K_{SFD}}\mathbf{z_{dyn}} + \mathbf{F_S} \tag{12}$$

Let $\mathbf{M_L}=(\mathbf{M_{SFD}}+\mathbf{M_S})$, $\mathbf{C_L}=(\mathbf{C_{SFD}}+\mathbf{C_S})$, $\mathbf{K_L}=(\mathbf{K_{SFD}}+\mathbf{K_S})$ represent the lubricated system mass, damping, and stiffness matrices, respectively. Since $\mathbf{F_S}=\mathbf{K_S}\mathbf{z_s}$, Eqn. (12) reduces to:

$$(\mathbf{M_L}\ddot{\mathbf{z}}_{\mathrm{dyn}} + \mathbf{C_L}\dot{\mathbf{z}}_{\mathrm{dyn}} + \mathbf{K_L}\mathbf{z}_{\mathrm{dyn}}) = \mathbf{F_{ext}}_{(t)} - M_{BC}\mathbf{a} \tag{13}$$

In the frequency domain, the equation of motion becomes:

$$\left[\mathbf{K_L} - \omega^2\mathbf{M_L} + i\omega\mathbf{C_L}\right]\bar{\mathbf{z}}_{\mathrm{dyn}(\omega)} = \bar{\mathbf{F}}_{(\omega)} - M_{BC}\bar{\mathbf{a}}_{(\omega)} \tag{14}$$

where $\bar{\mathbf{z}}_{\mathrm{dyn}(\omega)} = \mathrm{DFT}(\mathbf{z}_{dyn})$, $\bar{\mathbf{F}}_{(\omega)} = \mathrm{DFT}(\mathbf{F_{ext}}_{(t)})$, $\bar{\mathbf{a}}_{(\omega)} = \mathrm{DFT}(\mathbf{a})$ are the Fourier components of the recorded system dynamic displacement vector, applied dynamic load vector, and BC absolute acceleration vector, respectively.

Recall that two linearly independent tests take place for each operating condition, namely experiments with a clockwise whirl and a counter-clockwise whirl of the SFD test rig. Furthermore, let $\bar{\mathbf{H}}$ represent the complex stiffness:

$$\bar{\mathbf{H}}_{(\omega)} = \left[\mathbf{K_L} - \omega^2\mathbf{M_L} + i\omega\mathbf{C_L}\right] \tag{15}$$

Combining the two linearly independent tests, one where $\overline{\mathbf{F}}_1 \Rightarrow \left(\bar{a}_1, \bar{z}_{1\text{-dyn}}\right)$ and one where $\overline{\mathbf{F}}_2 \Rightarrow \left(\bar{a}_2, \bar{z}_{2\text{-dyn}}\right)$, produces:

$$\begin{gathered}
\overline{\mathbf{H}}_{\mathbf{L}(\omega)}\left[\bar{\mathbf{z}}_{1-\mathrm{dyn}(\omega)}\right]=\left[\overline{\mathbf{F}}_{1(\omega)}-M_{BC}\bar{\mathbf{a}}_{1(\omega)}\right] \\
\overline{\mathbf{H}}_{\mathbf{L}(\omega)}\left[\bar{\mathbf{z}}_{2-\mathrm{dyn}(\omega)}\right]=\left[\overline{\mathbf{F}}_{2(\omega)}-M_{BC}\bar{\mathbf{a}}_{2(\omega)}\right] \\
\begin{bmatrix} \overline{H}_{XX} & \overline{H}_{XY} \\ \overline{H}_{YX} & \overline{H}_{YY} \end{bmatrix}=\begin{bmatrix} \overline{F}_{1-X}-M_{BC}\bar{a}_{1-X} & \overline{F}_{1-Y}-M_{BC}\bar{a}_{1-Y} \\ \overline{F}_{2-X}-M_{BC}\bar{a}_{2-X} & \overline{F}_{2-Y}-M_{BC}\bar{a}_{2-Y} \end{bmatrix}\begin{bmatrix} \bar{z}_{1\text{-dyn}-X} & \bar{z}_{1\text{-dyn}-Y} \\ \bar{z}_{2\text{-dyn}-X} & \bar{z}_{2\text{-dyn}-Y} \end{bmatrix}^{-1}
\end{gathered} \tag{16}$$

With the recorded system displacement, applied dynamic load, BC acceleration, and M_{BC}=15.15 kg, Eqn. (16) can be solved for the complex stiffness $\overline{\mathbf{H}}$. An in-house developed MATHCAD® script iteratively builds the real and imaginary parts of the SFD complex stiffnesses, $\overline{\mathbf{H}}$ using the Instrumental Variable Filter parameter identification method (IVFM). Ref. **[**32] provides a detailed description of IVFM; in short, the method iteratively reduces the influence of measurement noise on identification of force coefficients.

As seen in Eqn. (15), the real part Re($\overline{\mathbf{H}}$) = $\mathbf{K_L}$-$\omega^2\mathbf{M_L}$ yields the lubricated system stiffness ($\mathbf{K_L}$) and added mass ($\mathbf{M_L}$) coefficients via, respectively, a intercept and parabolic curve fit versus frequency (ω), while the imaginary part Im($\overline{\mathbf{H}}$) = $\mathbf{C_L}\omega$ yields the lubricated system damping coefficients ($\mathbf{C_L}$) via a linear curve fit (pertaining to viscous damping) versus frequency. Similarly, tests of the dry (no lubricant) system produce structural force coefficients ($\mathbf{K_S}$, $\mathbf{M_S}$, $\mathbf{C_S}$).

Finally, identification of the SFD force coefficients follow as:

$$(\mathbf{K}, \mathbf{C}, \mathbf{M})_{\mathrm{SFD}} = (\mathbf{K}, \mathbf{C}, \mathbf{M})_{\mathrm{L}} - (\mathbf{K}, \mathbf{C}, \mathbf{M})_{\mathrm{S}} \tag{17}$$

The curve fits (**K**,**C**,**M** model) of the real and imaginary parts of $\overline{\mathbf{H}}$, respectively, show satisfactory correlation factor ($R^2 > 0.90$) in a majority of the test conditions over the frequency range 0 to 100 Hz. Moreover, the imaginary part of the system direct complex stiffness shows a constant slope indicating that the lubricated system damping is viscous in character. In addition, the slopes increase with orbit amplitude (r) and journal static eccentricity (e_s), evidencing C_{XX} and C_{YY} are a function of both r and e_s. Appendix D contains the experimentally calculated real and imaginary parts of the direct (H_{XX}, H_{YY}) and cross-coupled (H_{XY}, H_{YX}) system complex stiffness from circular whirl orbits departing from a centered position (e_s/c_1=0). Note that complex stiffnesses calcualted at other static eccentricity positions are omitted for brevity. Appendix E tabulates the correlation factors of the curve fits for all test conditions.

Model Predictions

The work in this thesis compares experimental results against those from a computational model in Refs. [13-15] as well as those from the short-length open-ends SFD model [2], see Eqns. (3-6). These comparisons assess the accuracy of the predictive models against the experimental results.

The orbit-based model uses finite elements to model half of the film land and solves an extended Reynolds equation to calculate the dynamic pressure field developed in the film land. Figure 7 depicts a cross section of half the film land modeled with 10 elements along the axial direction (and 120 elements in the circumferential direction).

The model then performs an *orbit analysis* process to estimate the SFD force coefficients from small amplitude motions about a static position, or finite amplitude

motions about a centered position. Through solving the extended Reynolds equation, the model determines (F_X, F_Y) for the desired SFD whirl motion amplitude, static eccentricity (e_s) over a frequency (f) range. Then, the model builds the system complex stiffness and performs a curve fit of the complex stiffness over the whirl frequency range to deliver the frequency-independent force coefficients. Notice that the steps are similar to the experimental procedure for force coefficient identification. Table 2 lists the input parameters needed to model the current damper 1.

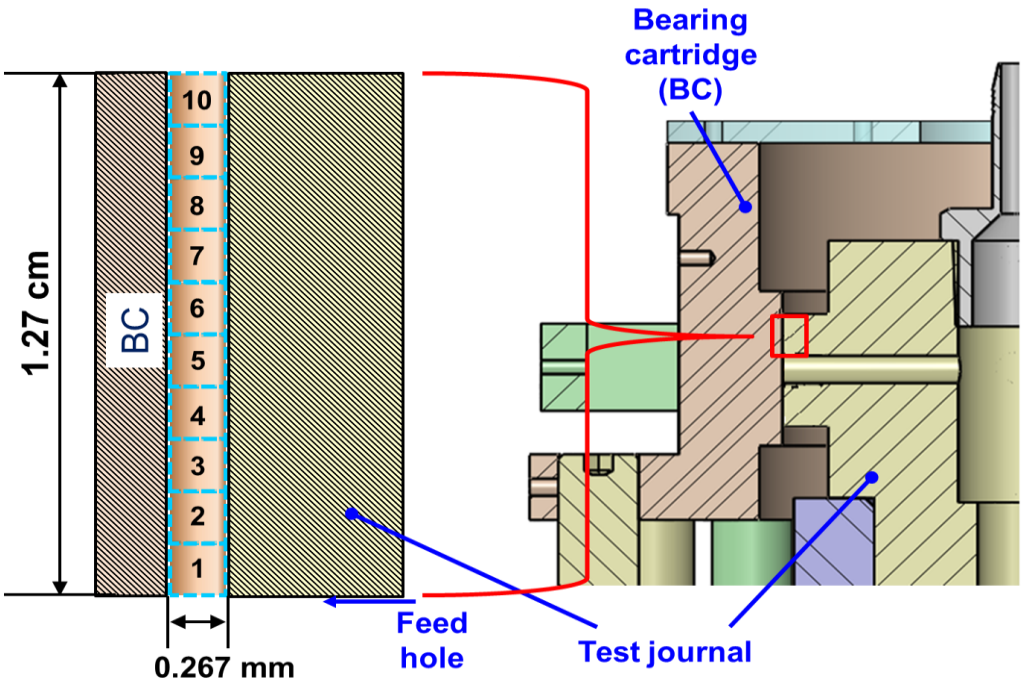

Figure 7. Cross-section of SFD test rig and finite elements modeling upper half of film land.

Table 2. Model parameters for Damper 1

Parameter	Value	Units
Journal diameter, D	127	mm
Nominal axial film land length, L	25.4	mm
Nominal radial clearance, c_1	0.267	mm
Ambient pressure at ends	0.0	bar(g)
Supply pressure, P_{in}	0.36	bar(g)
Cavitation pressure, P_{cav}	-1.01*	bar(g)
Supply temperature, T_S	23	°C
Oil viscosity	2.65	mPa·s
Oil density	802	kg/m^3

*The model selects cavitation pressure, -1.01 bar-gauge (~0 bar-absolute) which is the typical pressure where a "flat (constant) pressure zone [2, 43]" develops in recorded fluid film pressure profiles across various experiments [10-12].

As for predictions based on the short-length SFD model, recall from Eqns. (3-5) that the SFD force coefficients are primarily functions of the SFD geometry, and either the orbit amplitude (r), or the static eccentricity (e_s) for circular (centered and off-centered) whirl orbits.

The Test SFD Configurations and Operating Conditions

Comparisons of experimental results for the current SFD (#1) against that of two SFDs with similar configurations (dampers 2 and 3) examined in prior art, advance the knowledge of SFD design by highlighting the effects of a smaller radial clearance (in damper 2) and the effects of (2.5 mm length, 3.5 mm depth) end grooves (in damper 3) on SFD dynamic forced performance.

Recall that the SFDs are short-length open-ends (L/D=0.2) dampers. Each configuration has journal diameter D=0.127 m, and uses three feedholes located at the

mid-axial position of the film land, spaced 120° apart, and include hex sockets with orifice diameter of 2.54 mm. Figure 8 depicts schematic views of the current SFD and its test journal, as well as those for the comparison configurations.

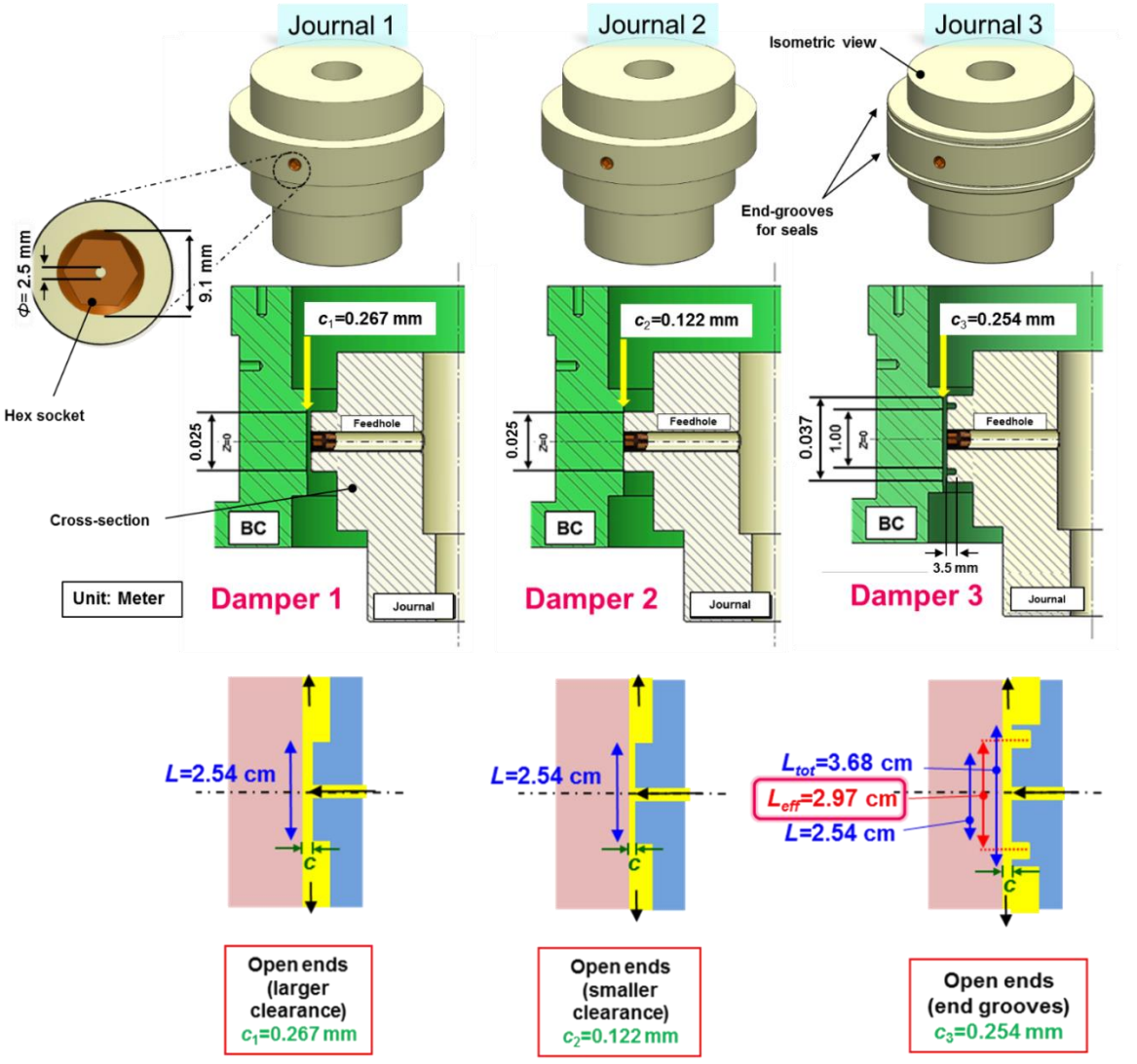

Figure 8. Isometric views of the SFD configurations and cross-section views. Left: clearance c_1=0.267 mm; Center: clearance c_2=0.122 mm; Right: clearance c_3=0.254 mm and end grooves (length 2.5 mm, depth 3.5 mm). Feedholes are 120° apart. Note that the figure exaggerates clearances c_1, and c_3.

Table 3 lists the geometry of the current damper (#1) as well as the geometry of the comparison dampers (#2 and 3) while Table 4 lists the operating conditions for the current damper as well as those for the comparison dampers. Note damper 2 with a smaller clearance requires of larger supply pressure (P_{in}) to maintain equal lubricant supply flow rate with the other dampers.

Table 3. Geometry for test open-ends SFDs [10-12].

Damper	Single film land length, L (cm)	Radial clearance, c (mm)	Structural stiffness, K_S (MN/m)	Number of feedholes	End grooves
Damper 1	2.54	0.267	12	3 open feedholes (ϕ=2.54 mm)	No
Damper 2	2.54	0.122	10.3*		No
Damper 3 [10]	2.97**	0.254	12		Yes, Length 2.5 mm, Depth 3.5 mm

*Structural stiffness determined via static load and BC displacement measurements. The damper with smaller clearance had a smaller measurement range, thus the calculated K_S is different.

**Denotes L_{eff}, including end grooves, as described in Refs. [11, 13]. $L_{tot}=L+2(L_{groove})+2L_{lip}$ = 2.54+(2)(0.25)+(2)(0.32) = 3.68 cm.

Table 4. Operating conditions for test dampers [10-12].

Damper	Frequency Range (Hz)	Whirl amplitude r (μm)	Static eccentricity e_s (μm)	Inlet flow rate Q_{in} (LPM)	Inlet pressure P_{in} (bar)
Damper 1 c_1=0.267 mm	10-100	13 – 191	0 – 229	5.10±0.11	0.36±0.03
Damper 2 c_2=0.122 mm	10-250*	13 – 64	0 – 64	6.10±0.11	1.86±0.03
Damper 3 [10] c_3=0.254 mm	10-100	13 – 191	0 – 191	5.06±0.11	0.35±0.03

*Measurements in prior experiments comment that force coefficients identified over frequency range 10-100Hz tend to be ~10% larger than the same coefficients identified over frequency range 10-250Hz [10-12].

CHAPTER V

RESULTS AND DISCUSSION

Experimentally Identified Force Coefficients for Damper 1

Recall damper 1 incorporates a land length L=2.54 cm, radial clearance c_1=0.267 mm, no grooves (end or central). Moreover, the damper receives ISO VG 2 oil at room temperature T=23°C, supply pressure P_{in}~0.36 bar, and flow rate Q_{in}=5.07 LPM.

Figure 9 shows an example of the measured real and imaginary parts of the lubricated system direct (H_{XX}, H_{YY})$_L$ and cross-coupled (H_{XY}, H_{YX})$_L$ complex stiffnesses from which the lubricated system stiffness, damping, added mass coefficients ($\mathbf{K_L}$, $\mathbf{C_L}$, $\mathbf{M_L}$), respectively, are identified. The data pertains to a centered (e_s/c_1=0) circular whirl orbit with amplitude r/c_1=0.05. Solid and dashed lines pertain to the curve fit constructed with the ($\mathbf{K}$, $\mathbf{C}$, $\mathbf{M}$)$_\mathbf{L}$ parameters. The correlation coefficient R^2 > 0.9 for the curve fits indicates that the ($\mathbf{K}$, $\mathbf{C}$, $\mathbf{M}$)$_\mathbf{L}$ model fits modestly well with the measured complex stiffnesses.

Figures 10 through 12 show the direct and cross-coupled SFD damping, (C), inertia, (M), and stiffness, (-K), coefficients , equal to [$\mathbf{K}$, $\mathbf{C}$, $\mathbf{M}$]$_\mathbf{L}$ -[$\mathbf{K}$, $\mathbf{C}$, $\mathbf{M}$]$_\mathbf{S}$, and derived from tests with whirl orbit amplitude r/c_1=0.05, 0.14, 0.29, 0.43, 0.57, 0.71 at a centered condition, and small amplitude whirl motions at static eccentricity e_s/c_1=0.0, 0.14, 0.29, 0.43, 0.57, 0.71 and 0.86. Recall that the static eccentricity (e_s) lies 45° away from the X and Y axes.

Figure 10 shows that the SFD direct damping coefficients (C_{XX}~C_{YY}) increase with both orbit amplitude (r) and static eccentricity (e_s). Increases in damping with orbit

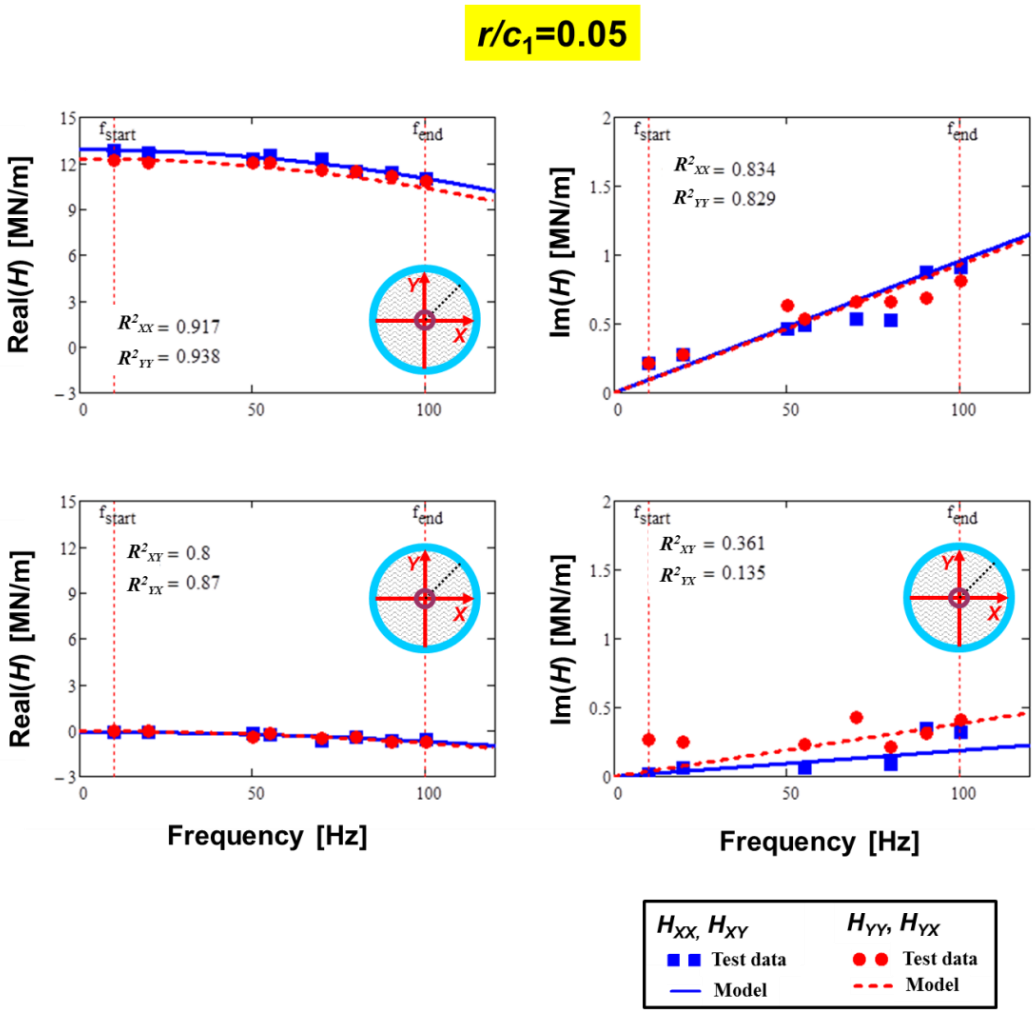

Figure 9. Measured real and imaginary parts of the direct (H_{XX}, H_{YY}) and cross-coupled (H_{XY}, H_{YX}) complex stiffnesses for a lubricated system. Data obtained from a centered (e_s/c_1=0) circular whirl orbit with small amplitude (r/c_1=0.05). Solid and dashed lines and correlation coefficient R^2 pertain to the curve fits constructed via the *K*, *C*, *M* parameters.

amplitude are nearly constant while increases with static eccentricity are small when e_s/c_1 < 0.3, and large when e_s/c_1 > 0.3. Cross-coupled damping coefficients (C_{XY}~C_{YX}) are generally an order of magnitude smaller than the direct damping coefficients. For small amplitude motions (r/c_1=0.05) about a very large static eccentricity (e_s/c_1 > 0.6), however, SFD cross-coupled damping coefficients grow considerably, becoming as large as ~60%

of the direct damping coefficients at a large static eccentricity. Note that this growth in cross-coupled damping with a large static eccentricity also appear seen in the results from dampers 2 and 3 [10-12].

Figure 11 shows that the SFD direct added mass coefficients (M_{XX}, M_{YY}) remain mostly invariant with orbit amplitude (r), and increase steadily with static eccentricity (e_s). Interestingly, the added mass coefficients increase slightly as the orbit amplitude increases. Prior experiments with other damper configurations do not show this behavior[2] [7-12]. Note that $M_{XX} \neq M_{YY}$ for a small number of conditions due to the system not being perfectly isotropic (i.e. feedhole distribution around the circumference of journal). The small differences, however, are generally within the measurement uncertainty. The cross-coupled added masses (M_{XY}, M_{YX}) are insensitive to orbit amplitude, being small in magnitude for the centered and moderately off-centered journal eccentricity, $e_s/c_1 < 0.3$. Notably, M_{XY} and M_{YX} increase for $e_s/c_1 > 0.3$, to reach ~50% of the direct coefficients (M_{XX}, M_{YY}) at a large static eccentricity, $e_s/c_1=0.6$.

Figure 12 shows the SFD direct stiffness coefficients $|K_{XX}|$, $|K_{YY}|$ increase moderately with both orbit amplitude (r) and static eccentricity (e_s) and appear to be mostly linear in nature. Recall that the identified SFD stiffness coefficients $\mathbf{K_{SFD}}=\mathbf{K_L}-\mathbf{K_s}$ are an artifact of the identification procedure. The figure depicts $-K_{XX}$, and $-K_{YY}$, meaning the test SFD delivers a negative SFD stiffness (softening) that is, direct $|K_{L\text{-}XX}|$, $|K_{L\text{-}YY}| < |K_{L\text{-}XX}|$, $|K_{L\text{-}YY}|$. The magnitude of the direct SFD stiffness coefficients does not exceed 40% of the structural stiffness (K_S). The cross-coupled stiffness $|K_{XY}|$, $|K_{YX}|$ are much

[2] Added mass coefficients for damper 2 are invariant with orbit amplitude, and added mass coefficients for damper 3 decrease slightly with orbit amplitude. See later, Figure 21 and Figure 23.

smaller in magnitude relative to the direct stiffness coefficients and exhibit little to no relationship with the static eccentricity or orbit amplitude, as expected in a SFD [1].

Appendix F presents the detailed procedure for the calculation of uncertainty in the SFD force coefficients. The direct damping (**C**), added mass (**M**), and stiffness (-**K**) coefficients have a maximum[3] uncertainty of U_{CSFD} =13%, U_{MSFD} =22% and U_{KSFD} =9%, respectively. Note that the force coefficients and their respective uncertainties are valid exclusively for the identification frequency range of 10-100 Hz.

[3] Actual uncertainties vary for every operating condition, see Appendix F.

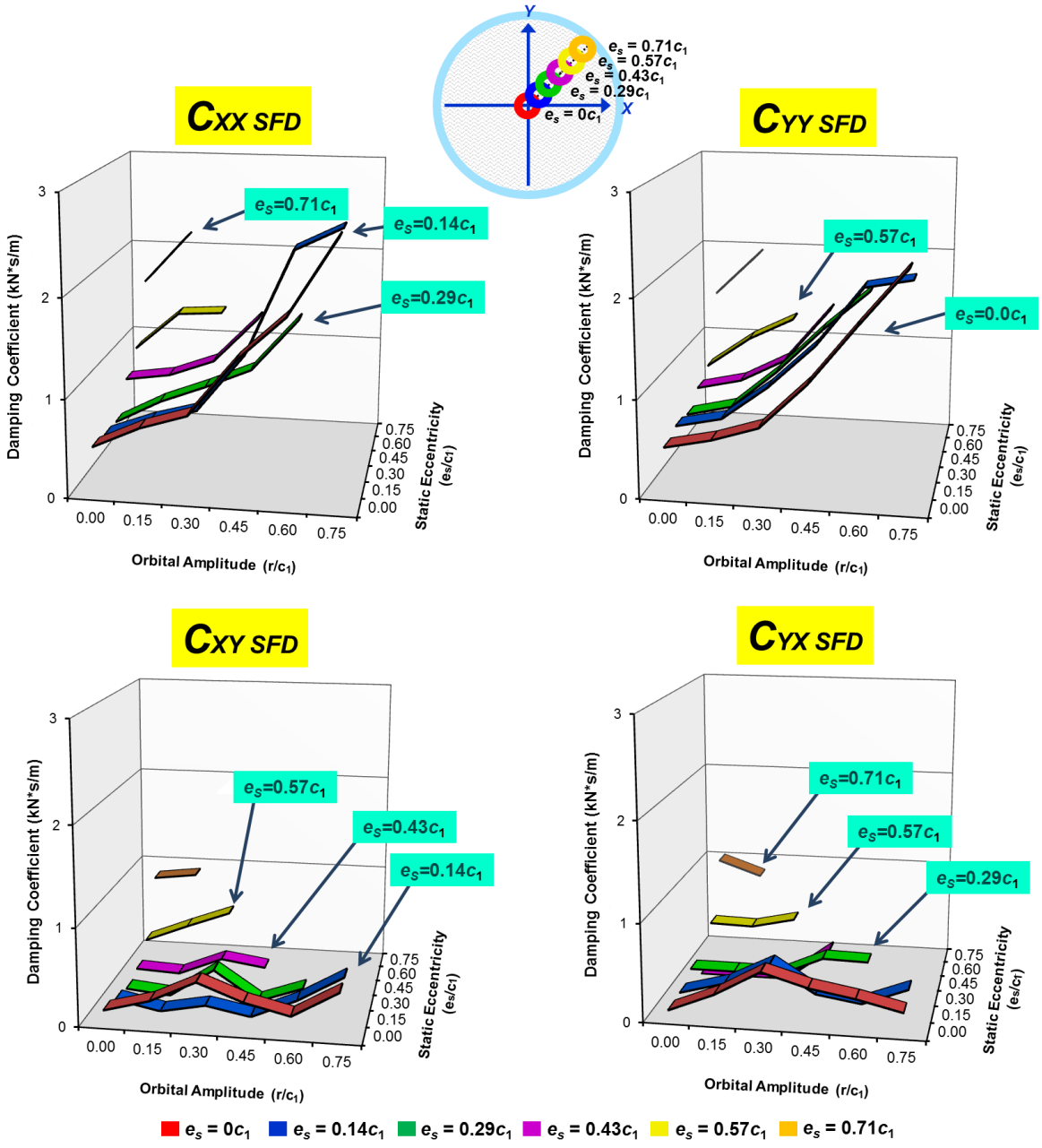

Figure 10. Open-ends short-length SFD (c_1=0.267 mm): Direct and cross-coupled damping coefficients $(C)_{SFD}$ versus static eccentricity (e_S/c_1) and orbit amplitude (r/c_1).

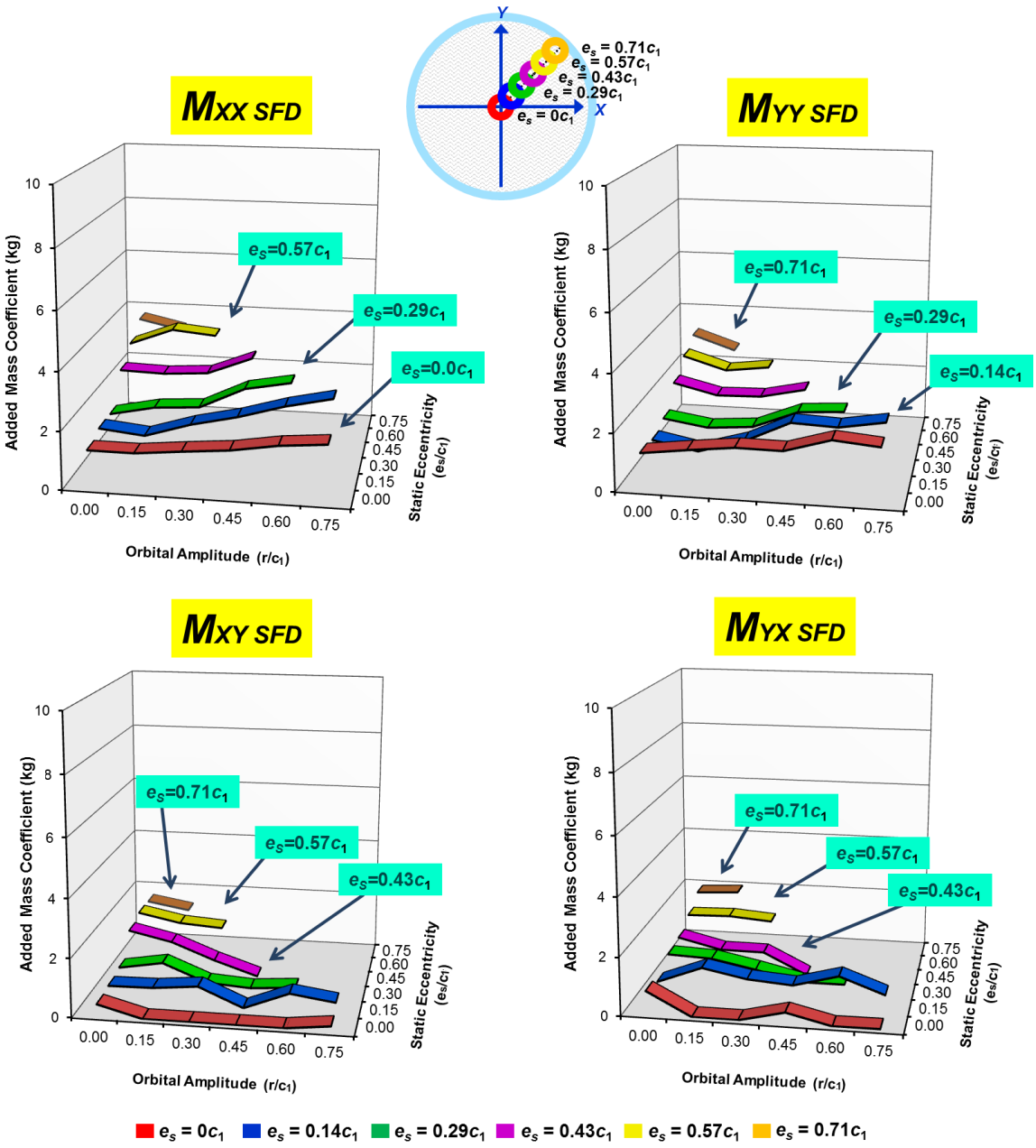

Figure 11. Open-ends short-length SFD (c_1=0.267 mm): Direct and cross-coupled added mass coefficients $(M)_{SFD}$ versus static eccentricity (e_S/c_1) and orbit amplitude (r/c_1).

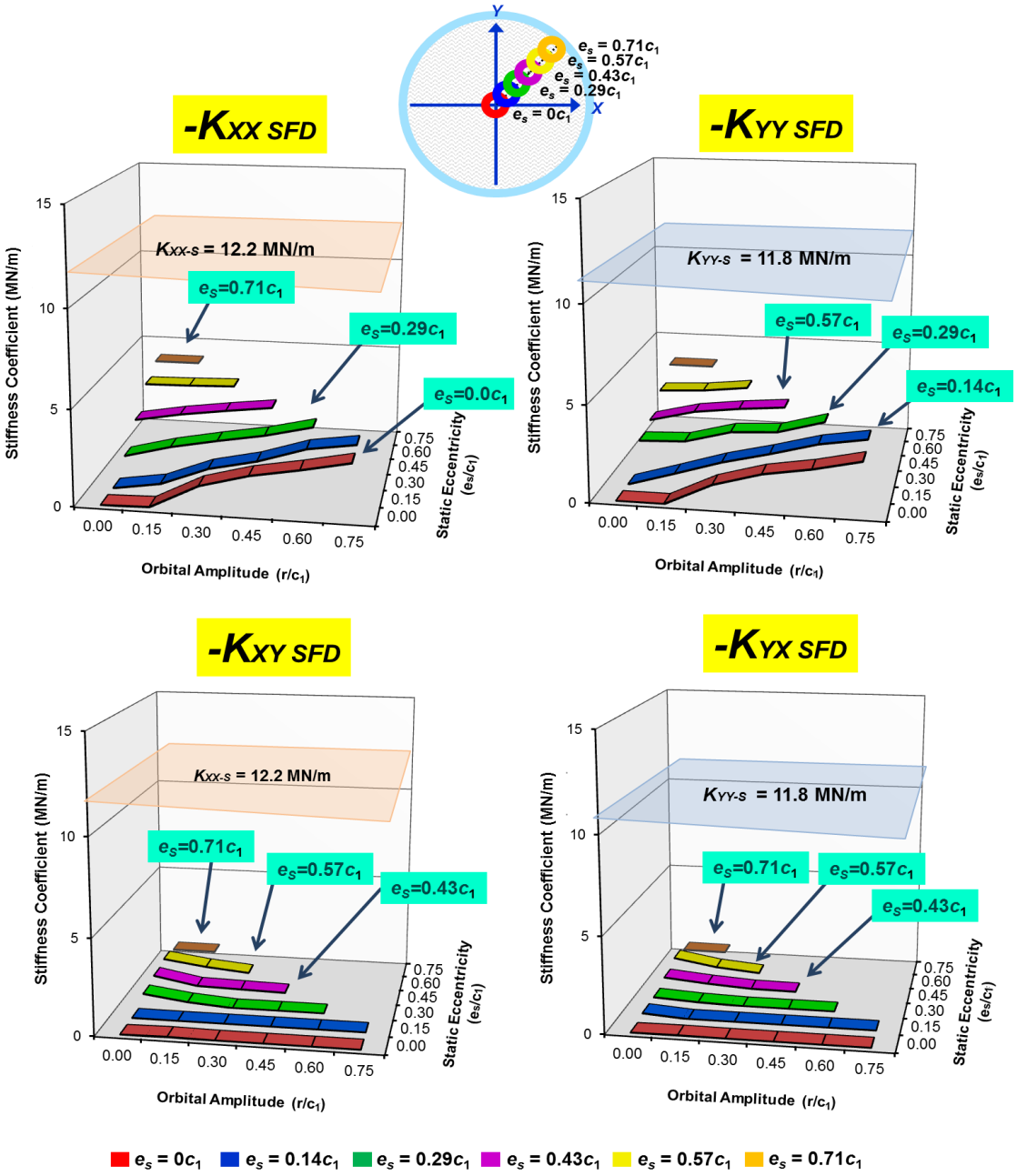

Figure 12. Open-ends short-length SFD (c_1=0.267 mm): Direct and cross-coupled stiffness coefficients $(K)_{SFD}$ versus static eccentricity (e_S/c_1) and orbit amplitude (r/c_1). Structural stiffness K_s also depicted for comparison.

Predicted Force Coefficients versus Experimental Results for Damper 1

This section presents predicted damping and added mass coefficients from the orbit-based model [13-15] as well as from the short-length open-ends SFD model [2]. Comparisons against the experimental results assess the accuracy of the predictive models. Overall, the trends (not to be confused with magnitudes) in experimental and predicted results coincide well for motions with moderate amplitude ($r/c_1 < 0.5$). Recall that the squeeze film Reynolds number over the operating conditions for damper 1 ranges from 1.4 to 12.5.

Figure 13 shows the experimentally identified and the predicted damping and added mass coefficients identified over the frequency range 10 to 100 Hz from circular orbits with amplitude, r/c_1=0.05 to 0.71, and at a centered condition, e_s/c_1=0. Error bars denote the uncertainty for the experimental parameters, as attained in Appendix F. The graphs include predictions from the orbit-based model and from the short-length open-ends SFD model, Eqns. (5, 6). Predicted damping force coefficients from the orbit-based model reproduce the same trend where the damping coefficient increases linearly at small amplitude orbits ($r/c_1 < 0.3$), and nonlinearly at large amplitude orbits ($r/c_1 > 0.3$). At a small orbit amplitude ($r/c_1 < 0.3$), the orbit-based model predictions and experimental results coincide. At large orbit amplitude motions ($r/c_1 > 0.3$), however, the models under predicts the damping force coefficient.

The test added mass coefficients are roughly 25% higher than both model predictions. Remarkably, the orbit-based model, unlike the short-length open-ends model, also shows the added mass coefficient increases with orbit amplitude for the current

damper when $r/c_1 < 0.7$. Predictions from either model for other configurations do not show this [10-12].

Figure 14 presents the experimentally identified and the predicted damping and added mass coefficients versus static eccentricity, e_s/c_1=0.0 to 0.86. The force coefficients correspond to a circular orbit with amplitude r=0.05c_1 and with frequency range 10 to 100 Hz. The graphs include predictions from the orbit-based model and the short-length SFD model, Eqns. (3, 4). Both the experimental and predicted results show a non-linear increase in damping with static eccentricity (e_s/c_1). At a lower static eccentricity, $e_s/c_1 <$ 0.5, the damping coefficients from experiments and both models are in excellent agreement. At $e_s/c_1 > 0.5$, however, the orbit-based model and the short-length SFD model over predict the damping coefficients.

As with the results shown in Figure 13, the models also under predict the added mass coefficients. While the experimental and predicted magnitudes of added mass coefficients are in close agreement at a lower static eccentricity ($e_s/c_1 < 0.4$) they diverge at a larger static eccentricity ($e_s/c_1 > 0.4$) with predicted magnitudes up to ~63% smaller than the experimental magnitudes. Despite this, their trends are in modest agreement; both demonstrate small increases in added mass at a moderate eccentricity, $e_s/c_1 < 0.4$, and moderate increases in added mass at larger static eccentricity, $e_s/c_1 > 0.4$.

Overall, both the orbit-based model and the short-length open-ends SFD model deliver force coefficients of similar magnitude, with noticeable differences only in added mass coefficients for whirl motions with a large orbit amplitude or damping coefficients for whirl motions departing from at a large static eccentricity. The similarity in the models' predictions is expected, however, due to the simplicity of the configuration of

damper 1. Predictions by both models for damper 3 [10] with end grooves, for example, demonstrate that the orbit-based model shows much closer agreement with the experimentally identified force coefficients.

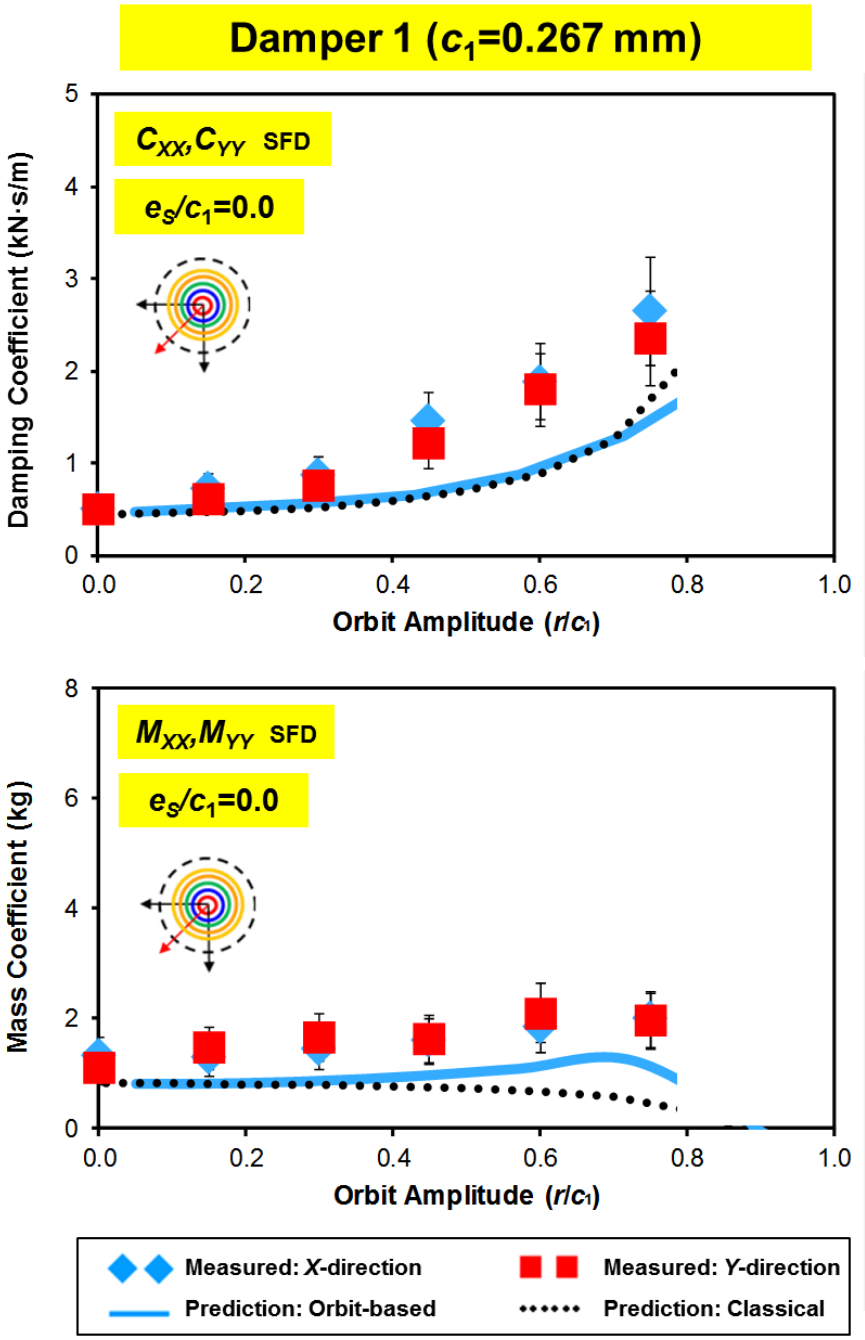

Figure 13. Open-ends SFD with c_1=0.267 mm: Measured and predicted direct damping coefficients (C_{XX}, C_{YY}) and mass coefficients (M_{XX}, M_{YY}) versus orbit amplitude (r/c_1) for circular orbits centered at e_S/c_1=0.

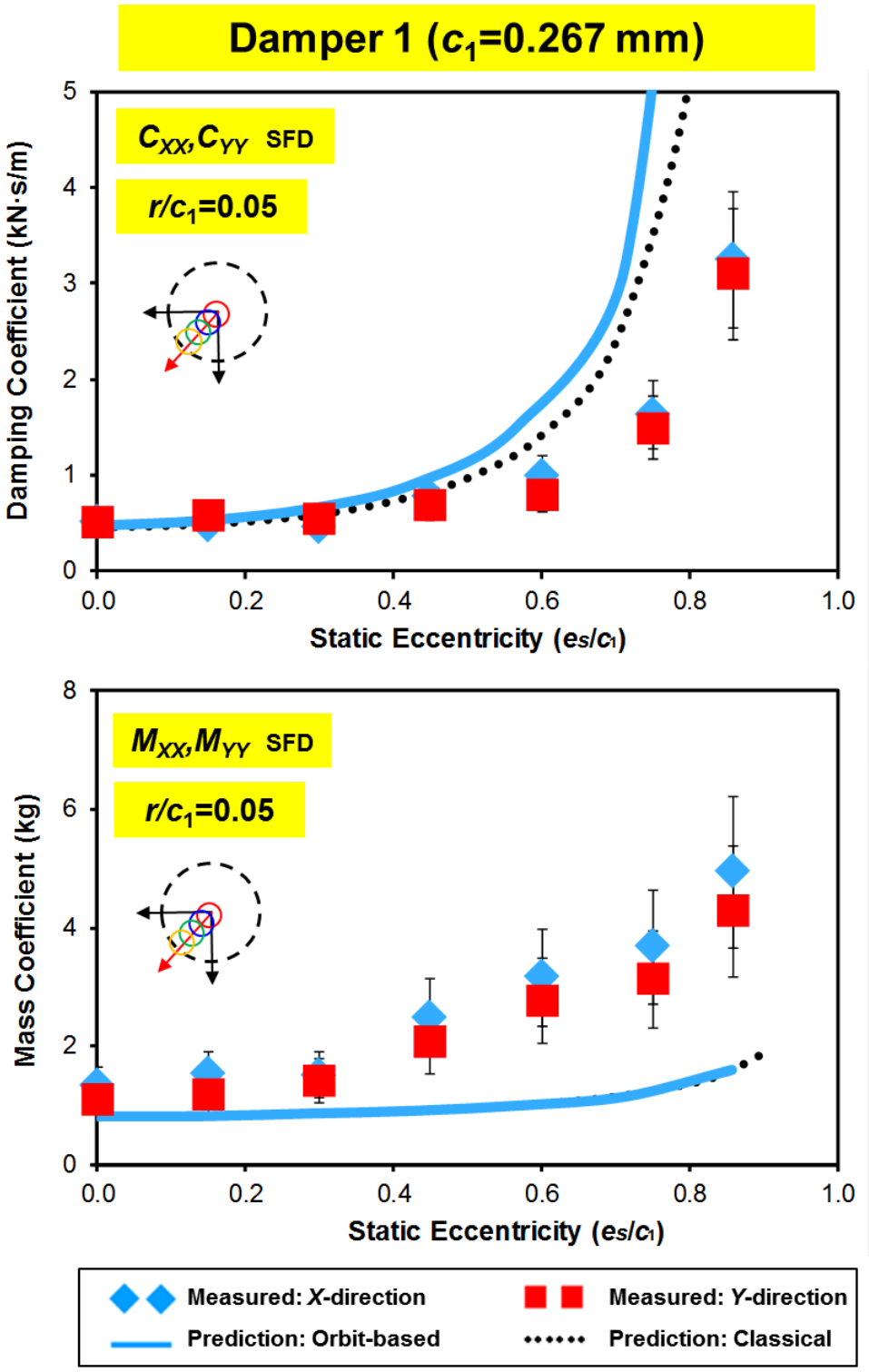

Figure 14. Open-ends SFD with c_1=0.267 mm: Measured and predicted SFD direct damping coefficients (C_{XX}, C_{YY}) and mass coefficients (M_{XX}, M_{YY}) versus static eccentricity (e_s/c_1) for small amplitude circular orbits (r/c_1=0.05).

Experimentally Recorded Dynamic Film Pressures for Damper 1

Identification of dynamic film pressures elucidates the relationship between SFD pressure generation and whirl frequency (ω), orbital amplitude (r), and static eccentricity (e_S).

Figure 15 depicts the mid-plane (P_4) *peak-to-peak* (*p-p*) dynamic film pressures versus excitation frequency for all test whirl orbit radii (r=0.05-0.71c_1) at e_S=0. The figure includes an inset that shows the location of the pressure sensor at the damper mid-plane and the journal whirl orbit relative to the BC. The trends show that the *p-p* dynamic pressures increase with whirl frequency, as well as orbit amplitude, with the latter being significantly more substantial. Note that *p-p* dynamic pressures recorded for motions with a large amplitude orbit ($r/c_1 \geq 0.43$) are limited in frequency range as recall, the load cell's rated measurement range of 500 lbf (2224 N) is exceeded at large amplitude motions and high whirl frequency. Figure 15 also hints to air ingestion occurring during SFD operation for f > 150 Hz, as the *p-p* dynamic pressure does not monotonically increase with frequency (f), in particular for $r/c_1 \geq 0.3$ (see dashed lines). Moreover, in general, for the recorded periods of motion, no two pressure peaks are alike in magnitude (±0.07 bar on average) due to air ingestion. Consequently, the fluctuations that exist in the pressure peak magnitudes influence the calculation of a unique *p-p* dynamic pressure.

Figure 16 depicts the mid-plane (P_4) *peak-to-peak* (*p-p*) dynamic pressures versus excitation frequency for all test static eccentricity conditions (e_S=0-0.86c_1) and whirl motions with a small orbit amplitude (r=0.05c_1). In comparison with the *p-p* dynamic pressures versus orbit amplitude, the *p-p* dynamic pressures appear to be less sensitive to static eccentricity. Still, the *p-p* dynamic pressures increase significantly at a large static

eccentricity relative to those exhibited at a low static eccentricity. For example, the dynamic *p-p* pressure obtained from whirl motions at a static eccentricity e_S/c_1=0.71 is nearly double that from whirl motions at a static eccentricity e_S/c_1=0.57. Likewise, the dynamic peak-to-peak pressure from whirl motions at a static eccentricity e_S/c_1=0.86 is nearly double that from whirl motions at static eccentricity e_S/c_1=0.71. This is expected since increasing the static eccentricity (along Θ=45°) displaces the BC towards the stationary journal thus reducing the clearance at the location of pressure sensor P_4 (Θ=225°).

Figure 17 and Figure 18 depict the film mid-plane pressure profiles (P_4) and the fluid film thickness (h) during the dynamic forced response. Figure 17 compares the film pressure profiles for circular centered (e_s=0) orbits with amplitude, r/c_1=0.14, 0.43, 0.71 and whirl frequency of 70 Hz. The squeeze film should achieve the maximum magnitude of pressure P_4 just after the maximum (negative) squeeze film velocity $\left|dh/dt\right|$ [2, 27, 28]. While periodic, the film pressure profiles, unlike the film thickness, do not exactly resemble a sinusoid during operation with orbit amplitude motions $r/c_1 > 0.05$. Instead, the pressure rises to zero psig, stagnates momentarily, rises to a maximum, and then sharply decreases. Ref. [43] attributes this behavior to air ingestion. Moreover, characteristics such as these are consistent with those exhibited by other damper configurations operating with air entrainment [10-12]. Similar to the observations made from the data in Figure 15, the magnitude of fluid film pressure increases with an increase in the whirl orbit amplitude.

Figure 18 compares the mid-plane (P_4) pressure profiles for operation of the SFD with circular orbit of small amplitude, r=0.05c_1, and operation from static eccentricity

e_s/c_1=0, 0.29, 0.57, 0.71, 0.86. Contrary to the film pressure profiles for large amplitude circular (centered) motions, the film pressure profiles for small amplitude whirl motions across all static eccentricities do not rise or drop suddenly, or stagnate. As with the observations from Figure 16, the magnitude of pressure increases with static eccentricity, with the pressures at e_s/c_1=0.86 being significantly larger than the other static eccentricity conditions (notice the change in the vertical axis scale in the third graph).

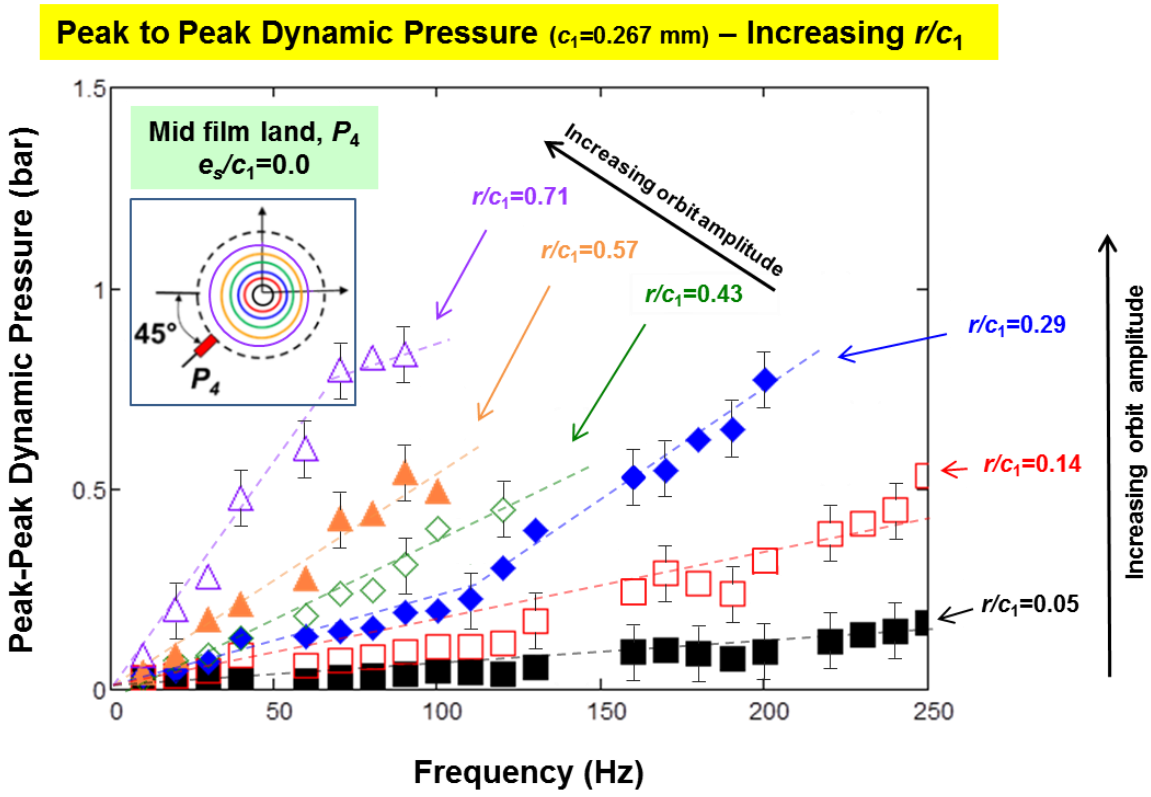

Figure 15. Open-ends SFD with c_1=0.267 mm: Measured mid-plane (P_4) peak-peak pressure versus whirl frequency for whirl motions with amplitude r/c_1=0.05-0.71. Measurements for tests at a centered condition (e_S/c_1=0). (Inset shows location of P_4, and journal position relative to the BC). Note error bars not depicted for every measurement to preserve visual clarity.

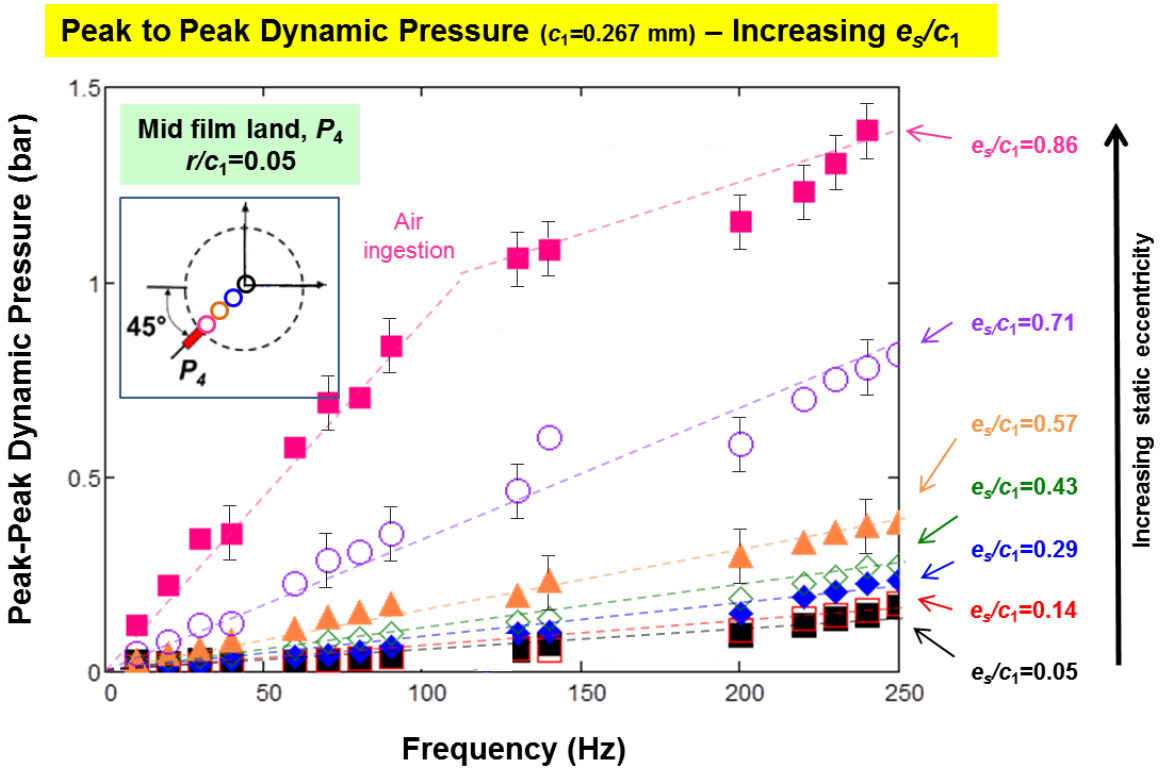

Figure 16. Open-ends SFD with c_1=0.267 mm Measured mid-plane (P_4) peak-peak pressure at the location of minimum film thickness versus whirl frequency for whirl motions departing from static eccentricity e_S/c_1=0-0.86. Measurements for tests with small orbit amplitude motions r/c_1=0.05. (Inset shows location of P_4, and journal position relative to the BC). Note error bars not depicted for every measurement to preserve visual clarity.

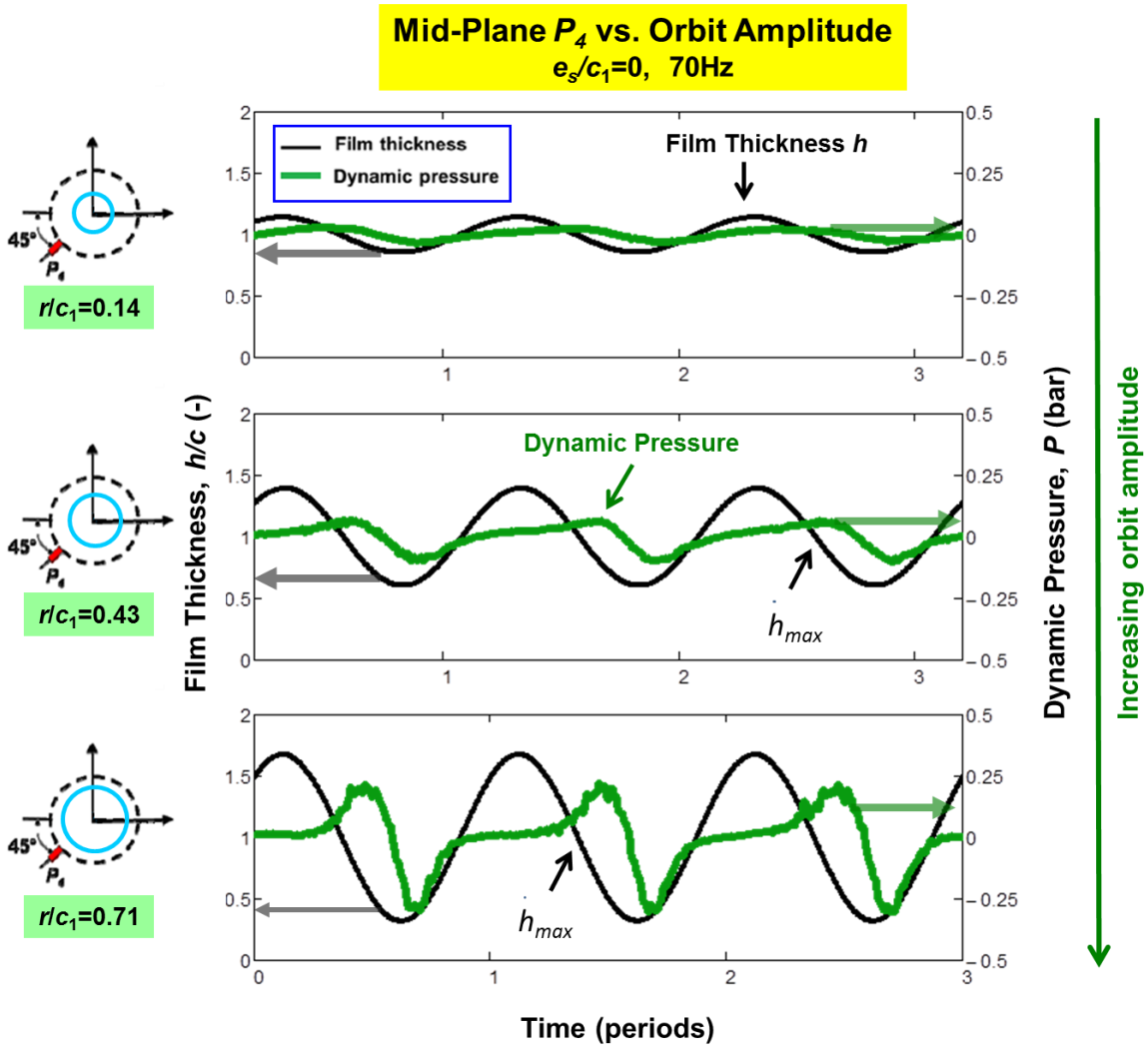

Figure 17. Open-ends SFD with c_1=0.267 mm: Dynamic film pressures (P_4) and film thickness (h) recorded at the mid-plane (z=0) and location of minimum film thickness. Circular centered (e_S/c_1=0) whirl orbits with amplitude r/c_1=0.14, 0.43 and 0.71, with frequency ω=70 Hz. (pressure supply P_{in}=0.36 bar).

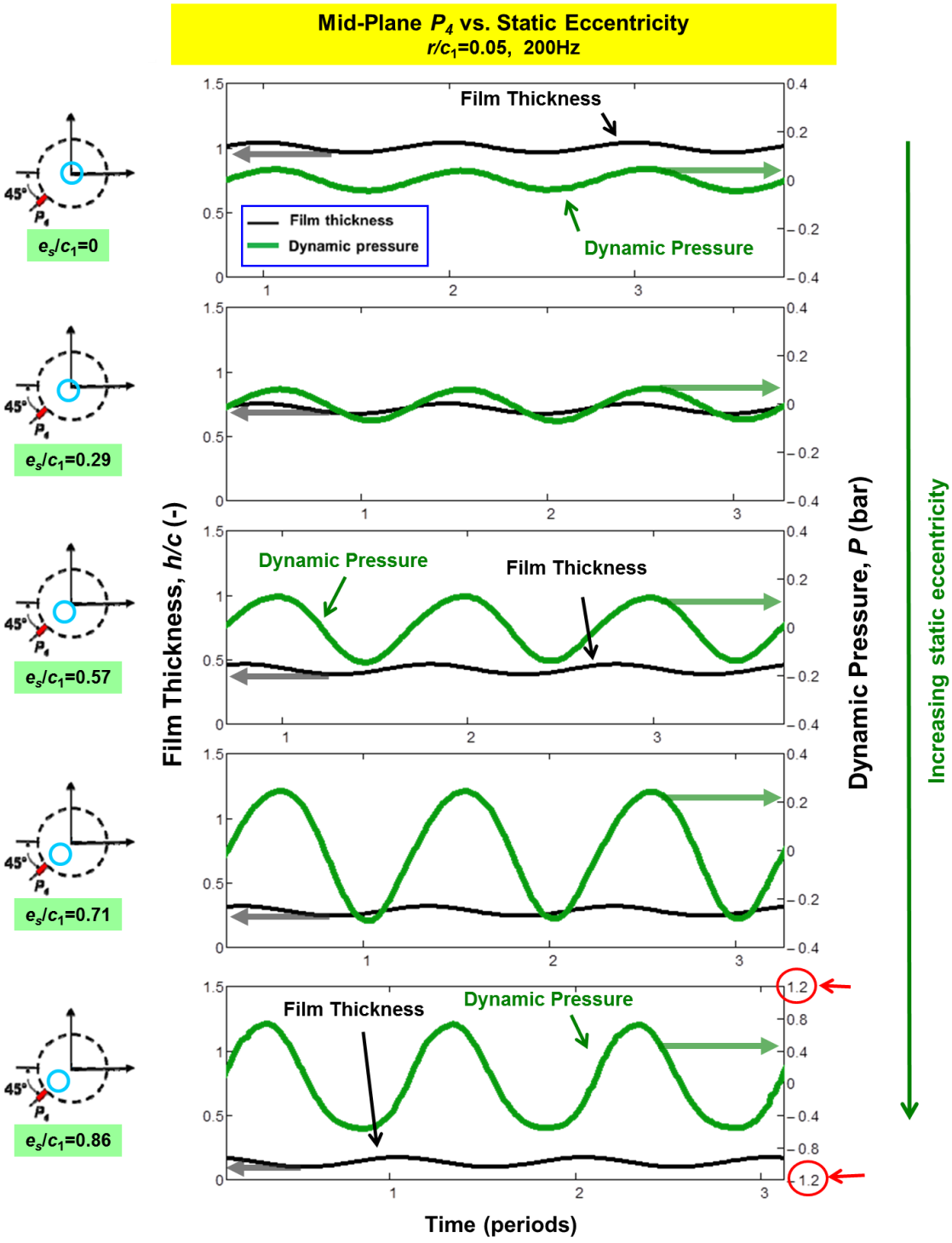

Figure 18. Open-ends SFD with c_1=0.267 mm: Dynamic film pressures (P_4) and film thickness (h) recorded at the mid-plane (z=0) and location of minimum film thickness. Whirl orbits with small amplitude r/c_1=0.05 from static eccentricity e_s/c_1=0, 0.29, 0.57, 0.71, 0.86. ω=200 Hz. (pressure supply P_{in}=0.36 bar).

Comparison of Identified Force Coefficients from SFDs 1, 2, and 3

Force coefficients identified for the current damper (#1) are compared against those for dampers 2 and 3 [10-12]. Recall Table 3 (reproduced below for convenience) lists the geometry of the various damper configurations. Figure 19 (extracted from Figure 8) depicts the cross-section views and geometry of the test SFDs.

Table 2. Geometry for test dampers [10-12].

Damper	Single film land length, L (cm)	Radial clearance, c (mm)	Structural stiffness, K_S (MN/m)	Number of feedholes	End grooves
Damper 1	2.54	0.267	12		No
Damper 2	2.54	0.122	10.3*	3 open feedholes (ϕ=2.54 mm)	No
Damper 3 [10]	2.97**	0.254	12		Yes Length 2.5 mm, Depth 3.5 mm

*Structural stiffness determined via static load and BC displacement measurements. The damper with smaller clearance had a smaller measurement range, thus the calculated K_S is different.

**Denotes L_{eff}, including end grooves, as described in Refs. [11, 13]. $L_{tot}=L+2(L_{groove})+2L_{lip}$ = 2.54+(2)(0.25)+(2)(0.32) = 3.68 cm.

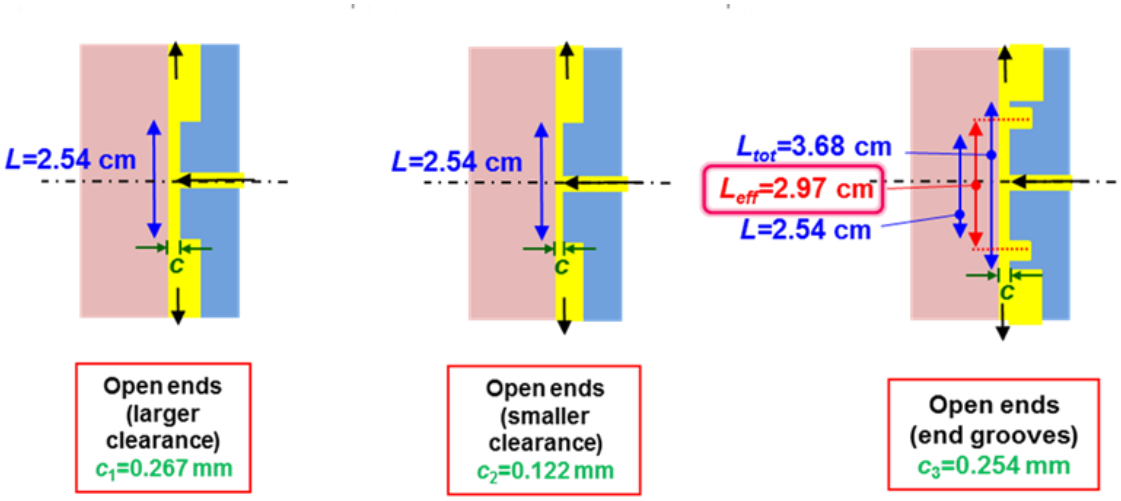

Figure 19. SFD cross-section views. Left: clearance c_1=0.267 mm; Center: clearance c_2=0.122 mm; Right: clearance c_3=0.254 mm and end grooves (length 2.5 mm, depth 3.5 mm).

The short-length SFD model predicts that the ratio of damping coefficients follows the geometric relationship (assuming the same oil viscosity) [2]:

$$\frac{C_{XX_3}}{C_{XX_1}} \sim \left(\frac{c_1}{c_3}\right)^3 \left(\frac{L_{3-eff}}{L_1}\right)^3 = \left(\frac{0.267}{0.254}\right)^3 \left(\frac{2.97}{2.54}\right)^3 = 1.85 \tag{18}$$

$$\frac{C_{XX_2}}{C_{XX_1}} \sim \left(\frac{c_1}{c_2}\right)^3 = \left(\frac{0.267}{0.122}\right)^3 = 10.5 \tag{19}$$

whereas the ratio of added mass coefficients follows [2]:

$$\frac{M_{XX_3}}{M_{XX_1}} \sim \left(\frac{c_1}{c_3}\right)\left(\frac{L_{3-eff}}{L_1}\right) = \left(\frac{0.267}{0.254}\right)\left(\frac{2.97}{2.54}\right) = 1.68 \tag{20}$$

$$\frac{M_{XX_2}}{M_{XX_1}} \sim \left(\frac{c_1}{c_2}\right) = \left(\frac{0.267}{0.122}\right) = 2.2 \tag{21}$$

Note that for damper 2, identification of the force coefficients took place over frequency range 10-250 Hz whereas for dampers 1 and 3, identification of the force coefficients took place over frequency range 10-100 Hz. This is, again, due to limitations in excitation frequency ($f \leq 100$ Hz) for large amplitude motions ($r/c > 0.3$) for the larger clearance dampers since the magnitude of the dynamic load exerted by the shakers often exceeds the load cell's rated measurement range of 500 lbf (2224 N). Measurements in prior experiments comment that force coefficients identified over frequency range 10-100 Hz tend to be ~10% larger than the same coefficients identified over frequency range 10-250 Hz [10-12].

Additionally, note that for damper 3, the simple formulas use the effective film length $L_{3\text{-}eff}$ =2.97 cm that is shorter than the actual wetted length $L_{3\text{-}tot}$ =3.68 cm (end grooves (two) are 2.5 mm in length, ends (two) are 3.2 mm in length), and larger than the

nominal film land length L_3=2.54 cm ($L_{3\text{-}tot} > L_{3\text{-}eff} > L_3$). Refs. [11, 13] detail the estimation of the effective length $L_{3\text{-}eff}$ by curve fitting the recorded pressure profile as a parabolic function of the axial coordinate (z).

Figures 20 to 25 show the damping (**C**) and added mass (**M**) coefficients obtained for the three dampers. Note that the coefficient magnitudes are normalized with respect to C^* and M^*, coefficients obtained via Eqns. (5, 6) for damper 1 (c_1=0.267 mm) at the centered condition (e_s/c=0), that is $\bar{C}_{XX} = C_{XX} \big/ C^*_{XX} = C_{XX} \big/ 0.46\,\text{kN}\cdot\text{s/m}$ and $\bar{M}_{XX} = M_{XX} \big/ M^*_{XX} = M_{XX} \big/ 0.82\,\text{kg}$. Note that the squeeze film Reynolds number for dampers 1, 2, and 3 operating over frequency range 10-100 Hz, 10-250 Hz, 10-100 Hz, respectively, are 1.4-12.5, 0.3-7.1, 1.2-12.3. The values mostly satisfy the short-length open-ends model.

Dampers 1 and 2

Figure 20 and 21 present, respectively, the test damping $(\bar{C}_{XX}, \bar{C}_{YY})_{\text{SFD}}$ and added mass $(\bar{M}_{XX}, \bar{M}_{YY})_{\text{SFD}}$ coefficients for both open-ends dampers 1 and 2. Figure 20 shows that $\bar{C}_{XX}$ and $\bar{C}_{YY}$ increase with orbit amplitude for motions about the center (e=0). Damper 2 generates on average ~eight times more damping than damper 1 at small amplitude motions (r/c < 100 μm), which lies moderately close to the theoretical ratio of 10.5. Figure 21 shows that at the centered position $\bar{M}_{XX}$ and $\bar{M}_{YY}$ remain invariant with orbit amplitude for damper 2 and likewise for damper 1 albeit the added mass coefficients increase slightly at larger amplitude motions (r > 100 μm). In general, however, the added

mass coefficients for damper 2 are on average 2.5 times larger than those for damper 1, which is close to the theoretical ratio of 2.2.

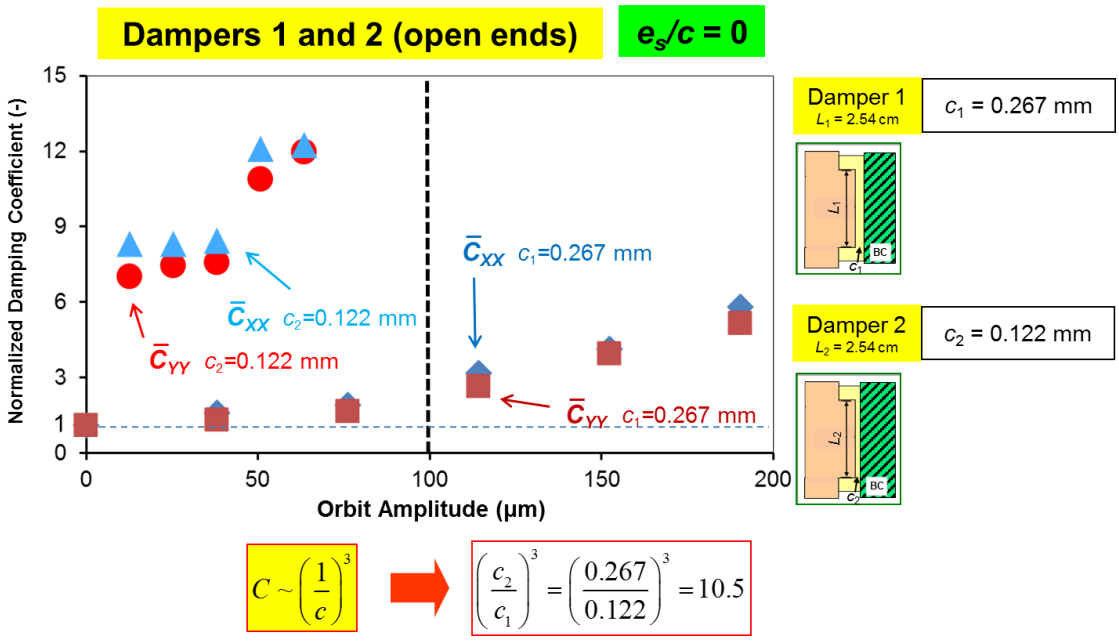

Figure 20. Open-ends dampers 1 and 2 normalized damping coefficients ($\bar{C}_{XX}$,$\bar{C}_{YY}$) versus orbit amplitude (μm). Parameters identified at a centered condition (e_s/c=0.0).

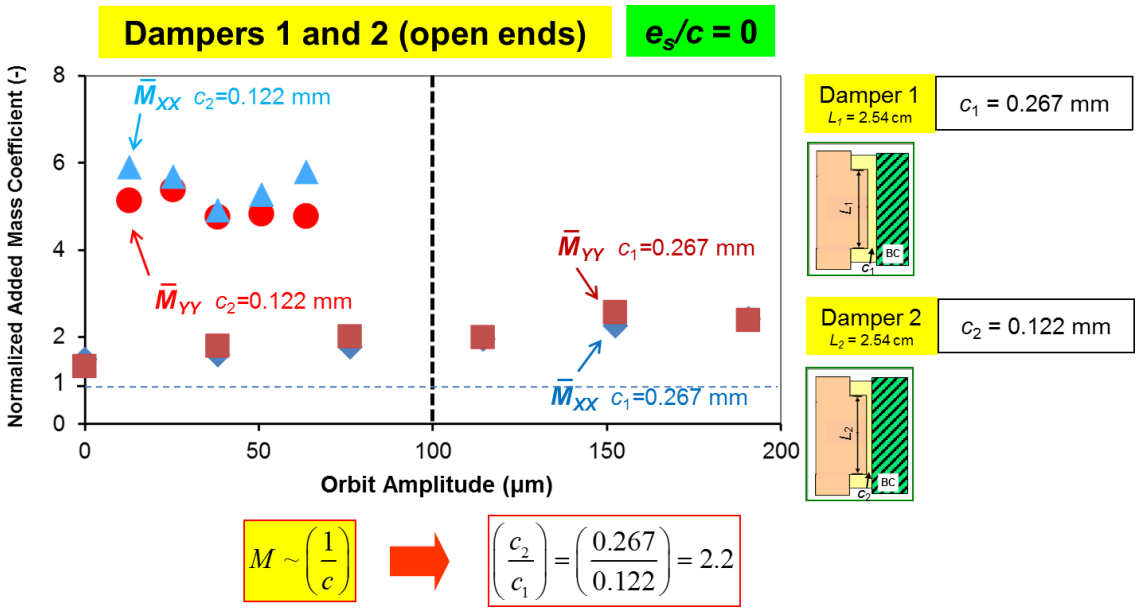

Figure 21. Open-ends dampers 1 and 2 normalized added mass coefficients ($\bar{M}_{XX}$,$\bar{M}_{YY}$) versus orbit amplitude (μm). Parameters identified at a centered condition (e_s/c=0.0).

Dampers 1 and 3

Comparison of force coefficients for damper 1 vis a vis damper 3 shows the ratio of damping coefficients between the two matches closely the geometric relationships. Recall damper 3 uses an effective land length, $L_{3\text{-}eff}$=2.97 cm, as detailed in Refs. [11, 13]. Figure 22 and 23 show, respectively, the direct damping $(\bar{C}_{XX},\bar{C}_{YY})_{\text{SFD}}$ and direct added mass coefficients $(\bar{M}_{XX},\bar{M}_{YY})_{\text{SFD}}$ versus orbit amplitude for centered (e=0) circular motions for dampers 1 and 3. Similarly, Figure 24 and 25 show, respectively, the direct damping and direct added mass coefficients versus static eccentricity for small amplitude circular orbits (r/c=0.15). The damping produced for the slightly smaller clearance damper 3 appears consistently ~1.75 times higher than the damping produced by damper 1, which agrees very well with the theoretical value of 1.85.

On the other hand, the added mass for damper 3 remains noticeably larger than that for damper 1, ~2.5 times, which deviates from the geometric ratio of 1.68. However, the reason for the disparity lies in the presence of (end) grooves in damper 3, which as seen in literature [10, 11, 20, 21, 29, 30], generate increased added fluid inertia coefficients.

Overall, the experimentally identified force coefficients obtained for all three damper configurations agree fairly well with the ratios predicted in Eqns. (18-20). For example, damper 3 (with slightly longer land length, L_{eff}) has a slightly larger damping and added mass than damper 1. Similarly, open-ends damper 2, whose clearance compares ~ 50% to that of damper 1, generates roughly eight times more damping and two times more added mass than damper 1.

Appendix G contains comparisons of the recorded dynamic film pressures versus whirl frequency (ω) and axial position (Z) for dampers 1, 2, and 3.

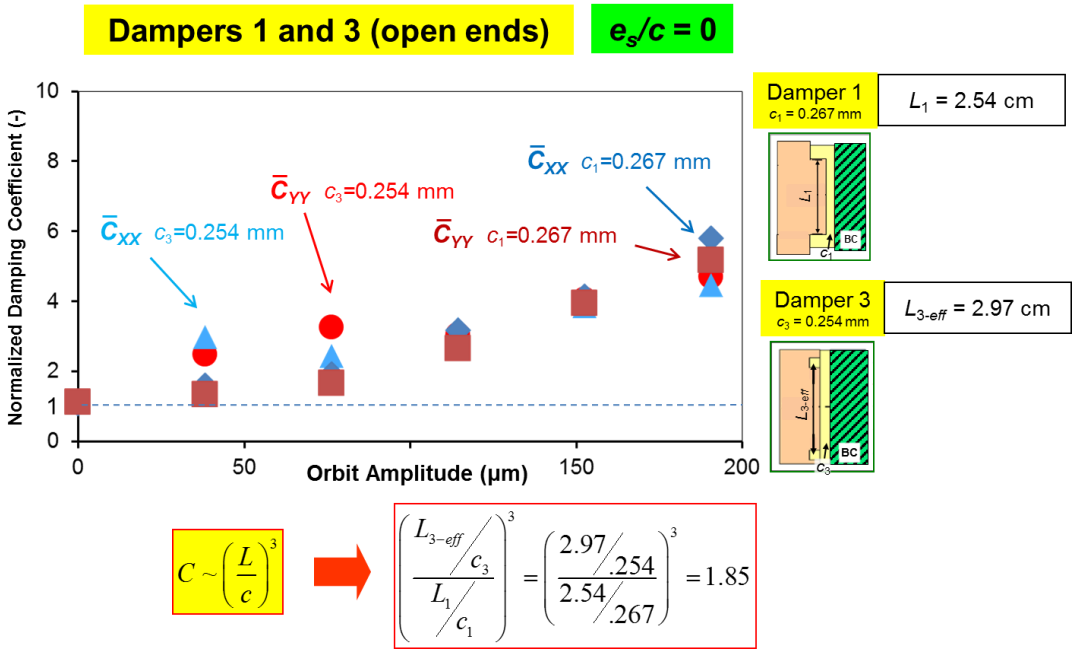

Figure 22. Open-ends dampers 1 and 3 normalized damping coefficients ($\bar{C}_{XX}$,$\bar{C}_{YY}$) versus orbit amplitude (μm). Parameters identified at a centered condition (e_s/c=0.0).

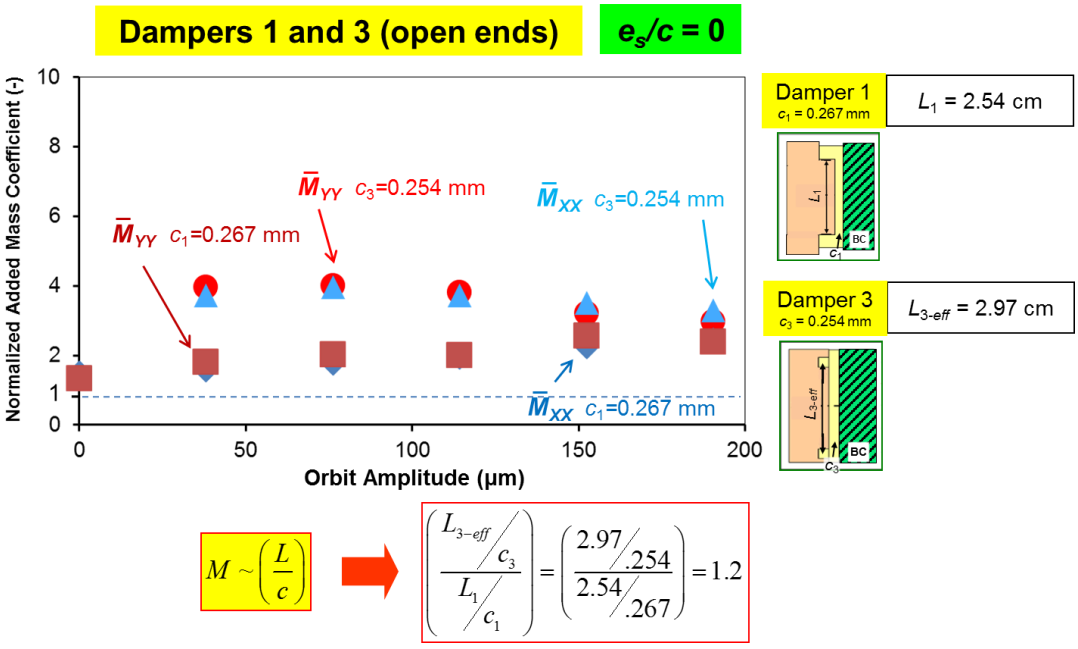

Figure 23. Open-ends dampers 1 and 3 normalized added mass coefficients ($\bar{M}_{XX}$,$\bar{M}_{YY}$) versus orbit amplitude (μm). Parameters identified at a centered condition (e_s/c=0.0).

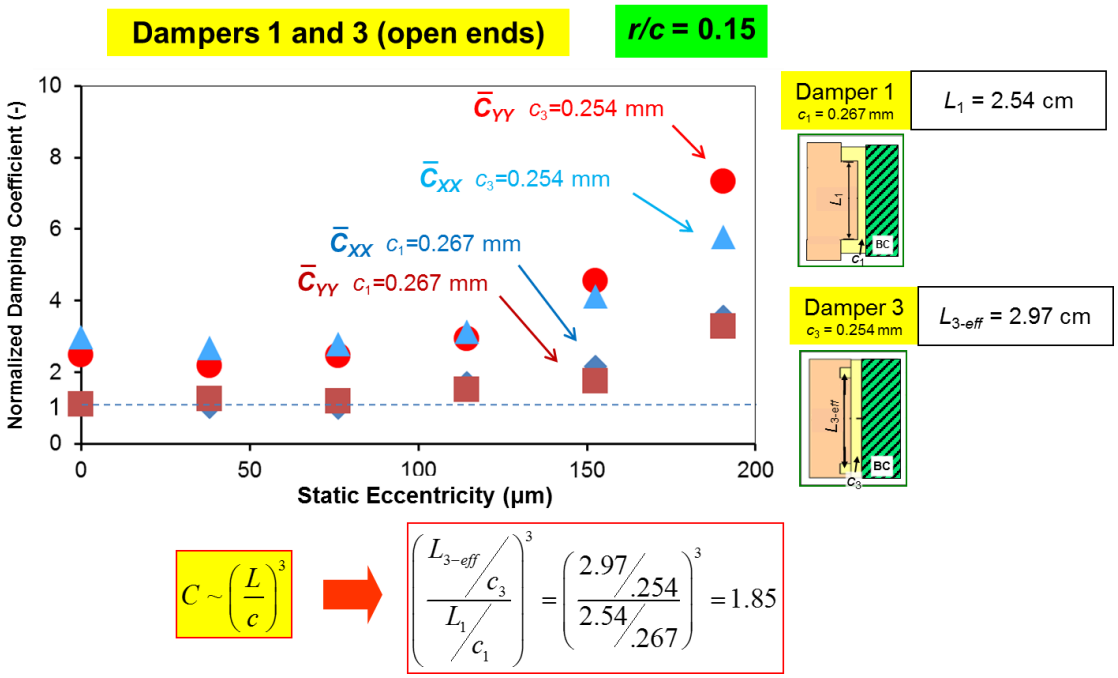

Figure 24. Open-ends dampers 1 and 3 normalized damping coefficients ($\bar{C}_{XX}$,$\bar{C}_{YY}$) versus static eccentricity (μm). Parameters identified for an orbit amplitude (*r*/*c*=0.15).

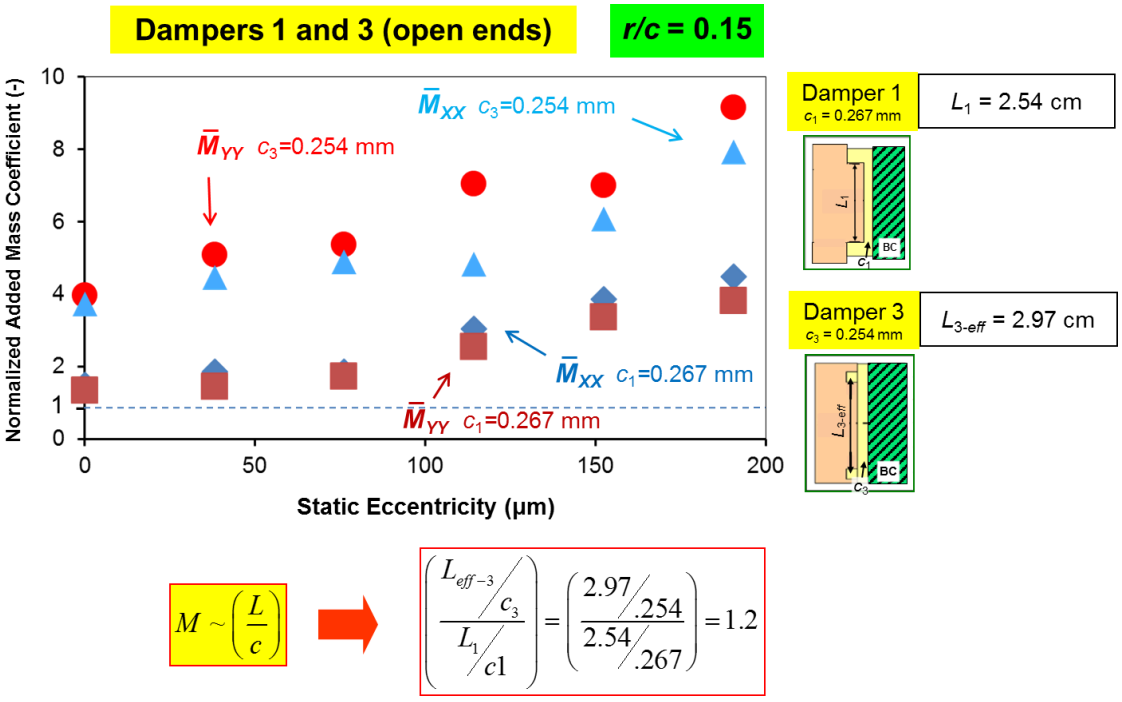

Figure 25. Open-ends dampers 1 and 3 normalized added mass coefficients ($\bar{M}_{XX}$,$\bar{M}_{YY}$) versus static eccentricity (μm). Parameters identified for an orbit amplitude (*r*/*c*=0.15).

CHAPTER VI

CONCLUSIONS

This thesis consolidates experimental findings that evaluate the dynamic forced performance of a simply configured short-length (L/D=0.2) open-ends SFD with clearance c_1=0.267 mm. In particular, this thesis presents identified force coefficients and recorded fluid film dynamic pressures for the SFD undergoing circular whirl orbits ranging from a small to large whirl orbit amplitude, and departing from a small to large static eccentricity. Additionally, the analysis in this thesis compares the performance of the current damper (termed as damper 1) against a second damper (#2) with a smaller radial clearance (c_2=0.122 mm), as well as against a third damper (#3) with similar clearance (c_3=0.254 mm) and configured with end grooves (for provision of end seals, L_{eff}=2.97 cm) [10-12].

Major Findings

a) Identified force coefficients show that damper 1 with large clearance (c_1=0.267 mm) offers direct damping coefficients that are slightly more sensitive to increases in static eccentricity (e_S) than to increases in orbit amplitude (r). SFD inertia coefficients are also more sensitive to increases in the static eccentricity than to orbit amplitude.

b) Predictions from the orbit-based model [13-15] agree modestly with the experimentally identified force coefficients. The overall trends in the experimentally identified damping and inertia coefficients versus orbit amplitude

or static eccentricity match those predicted by the model. Moreover, at a low orbit amplitude and low static eccentricity, the predicted and experimental damping coefficients coincide. However, the model over predicts the damping coefficients and under predicts the inertia coefficients at a large static eccentricity ($e_s/c_1 > 0.5$).

c) The fluid film dynamic pressure appears more sensitive to increases in orbit amplitude than to increases in static eccentricity. However, at a large static eccentricity ($e_s/c_1 > 0.7$), the dynamic pressure at the mid plane (and location of minimum film thickness) jumps to an order of magnitude larger than the pressure measured for a smaller static eccentricity. Film pressures show signs of air ingestion for operation with a large orbit amplitude (r/c_1=0.71).

d) Comparisons of experimental results between dampers 1, 2, and 3 show that the damping and added mass coefficients closely conform to the relationship based on the geometric ratios derived from the short-length SFD model, i.e. $C \propto \left(L/c\right)^3$ and $M \propto L^3/c$. Damper 2 (c_2=0.122 mm (c_2~0.5c_1), no end grooves) produces ~eight times more damping and ~2.5 times more added mass than does damper 1 (c_1=0.267 mm). Damper 3 (c_3=0.254 mm (c_1~c_3), with end grooves (L_{eff}=2.97 cm)) produces ~1.75 times more damping but ~2.5 times more added mass than does damper 1. Larger (than expected) added mass coefficients in damper 3 result from its employment of end grooves.

e) The fluid film dynamic *p-p* pressures tend to be largest in damper 2 (c_2=0.122 mm) due to its small clearance. Similarly, the fluid film dynamic pressures in

damper 3 (c_3=0.254 mm) are only slightly larger than the pressures measured in damper 1 (c_1=0.267 mm).

Future Work

As seen in comparisons of experimentally identified damping and added mass coefficients against those from the short-length open-ends SFD model and against those from the orbit-based model, the models over predict the damping coefficients and under predict the inertia coefficients for whirl motions departing from at a large static eccentricity ($e_s/c_1 > 0.5$). Thus, operation of a SFD at a large static eccentricity and fluid inertia effects (manifested as added mass coefficients) warrants continued particular investigation. Future work should address to the discrepancy between predictions and experimentally identified damping and added mass coefficients for motions departing from a large static eccentricity, in particular.

Closure

This thesis thoroughly compiles and compares the experimental results obtained from squeeze film dampers undergoing circular whirl orbits. The work addresses to industry needs for simpler SFD configurations by experimentally scrutinizing the dynamic force performance of a very simply configured hole-fed SFD: short-length (L/D=0.2), open-ends, with no central groove, no end grooves (provisions for seals), and a nominal radial clearance c_1=0.267 mm (c_1/R=0.004). The work also brings to light certain design characteristics in SFDs. Comparisons of three dampers illustrate the effects of a tighter clearance and the effects of end grooves on a test SFD dynamic force performance.

REFERENCES

[1] Zeidan, F., San Andrés, L., and Vance, J., 1996, "Design and Application of Squeeze Film Dampers in Rotating Machinery," Proc. of the 25th Turbomachinery Symposium, Turbomachinery Laboratory, Houston, TX, pp. 169-188.

[2] San Andrés, L., 2012, "Squeeze Film Damper: Operation, Models and Technical Issues," Modern Lubrication Theory, Notes 13, Texas A&M University Digital Libraries, http://repository.tamu.edu/handle/1969.1/93197

[3] Vance, J. M., 1988, *Rotordynamics of Turbomachinery*, John Wiley and Sons, Hoboken, New Jersey, Chap. 6.

[4] Harnoy, A., 2002, *Bearing Design in Machinery: Engineering Tribology and Lubrication*, CRC Press, Boca Raton, Florida, Chap. 18.

[5] Della Pietra, L., and Adiletta, G., 2002, "The Squeeze Film Damper Over Four Decades of Investigations. Part I: Characteristics and Operating Features," Shock and Vib. Dig., **34**(1) pp. 3-26.

[6] Della Pietra, L., and Adiletta, G., 2002, "The Squeeze Film Damper Over Four Decades of Investigations. Part II: Rotordynamic Analyses with Rigid and Flexible Rotors," Shock and Vib. Dig., **34**(2) pp. 97-126.

[7] Seshaghiri, S., 2011, "Identification of Force Coefficients in Two Squeeze Film Dampers with a Central Groove," M.S. Thesis, Texas A&M University, May.

[8] Mahecha, P., 2011, "Experimental Dynamic Forced Performance of a Centrally Grooved, End Sealed Squeeze Film Damper," M.S. Thesis, Texas A&M University, August.

[9] San Andrés, L., Seshaghiri, S., 2013, "Damping and Inertia Coefficients for Two End Sealed Squeeze Film Dampers With a Central Groove: Measurements and Predictions," J. Eng. Gas Turbines and Power, **135**(11), p. 112503

[10] San Andrés, L., Jeung, S., and Bradley, G., 2014, "Dynamic Forced Performance of Short Length Open-ends Squeeze Film Damper with End Grooves," *The 9th International Conference on Rotor Dynamics*, IFToMM, Milan, Italy, Aug. 29-Sep. 5, 2211-0984, pp. 1-11.

[11] Bradley, G., 2013, "Performance of a Short Open-End Squeeze Film Damper With Feed Holes: Experimental Analysis of Dynamic Force Coefficients," M.S. Thesis, Texas A&M University, August.

[12] Jeung, S. 2013, "Performance of an Open Ends Squeeze Film Damper Operating With Large Amplitude Orbital Motions: Experimental Analysis and Assessment of the Accuracy of the Linearized Force Coefficients Model," M.S. Thesis, Texas A&M University, December.

[13] Delgado, A., and San Andrés, L., 2010, "A Model for Improved Prediction of Force Coefficients in Grooved Squeeze Film Dampers and Oil Seal Rings," ASME J. Tribol., **132**(3), 7p. 032202.

[14] San Andrés, L., and Delgado, A., 2012, "A Novel Bulk-Flow Model for Improved Predictions of Force Coefficients in Grooved Oil Seals Operating Eccentrically," ASME J. Eng. Gas Turbines Power, **134**(5), p. 052509.

[15] San Andrés, L., and Jeung, S., 2015, "Orbit-Model Force Coefficients for Fluid Film Bearings: A Step Beyond Linearization," ASME J Gas Turb Pwr, **138**(2), p. 022502.

[16] Nikolajsen, J. L., and Holmes, R., 1979, "Investigation of Squeeze Film Isolators for the Vibration Control of a Flexible Rotors," J. Mech. Eng. Sci.., **21**(4) pp. 247-252.

[17] Marmol, R.A., and Vance, J.M., 1978, "Squeeze Film Damper Characteristics for Gas Turbine Engines," ASME J. Mech. Design, **100**(1), pp. 139-146.

[18] Cooper, S., 1963, "Preliminary Investigation of Oil Films for Control of Vibration," Proc. of Lubrication and Wear Convention, London, IMechE, pp. 305-315.

[19] Cookson, R.A., 1979, "The Effectiveness of Squeeze-Film Damper Bearings Supporting Rigid Rotors Without a Centralising Spring," Int. J. Mech. Sci., **21**, pp. 639-650.

[20] San Andrés, L., 1992, "Analysis of Short squeeze Film Dampers with a Central Groove," ASME, J. Tribol., **114**(4), pp. 659-664.

[21] Arauz, G., and San Andrés, L., 1994, "Effect of a Circumferential Feeding Groove on the Dynamic Force Response of a Short Squeeze Film Damper," ASME J. Tribol., **116**(2), pp. 369-377.

[22] Chen, P.Y., and Hahn, E.J. 1994, "Pressure Distribution in Squeeze Film Dampers with Oil Hole Feed," Proc. of the IMechE, Part J: J. Eng. Tribol., pp. 105-112.

[23] Defaye, C., Arghir, M., and Bonneau, O., 2006, "Experimental Study of the Radial and Tangential Forces in a Whirling Squeeze Film Damper," STLE Tribol. Trans., **49**(2) pp. 271-278.

[24] San Andrés, L., 2012, "Fluid Inertia and Turbulence in Fluid Film Bearings, Notes 09, Texas A&M University Digital Libraries, http://repository.tamu.edu/handle/1969.1/93249

[25] Smith, D. M., "Journal Bearing Dynamic Characteristics - Effect of Inertia of Lubricant," Proc. Inst. Mech. Engrs., Vol. 179, Part 3J, 1964-1965, pp. 37-44.

[26] Reinhardt, F., and Lund, J. W., 1975, "The Influence of Fluid Inertia on the Dynamic Properties of Journal Bearings," ASME J. Lubr. Technol., **97**(1), pp. 154-167.

[27] Tichy, J.A., 1982, "Effects of Fluid Inertia and Viscoelasticity on Squeeze-Film Bearing Forces," ASLE Trans., **25**(1), pp. 125-132.

[28] Tichy, J.A., 1984, "Measurements of Squeeze-Film Bearing Forces and Pressures, Including the Effect of Fluid Inertia," ASLE Trans., **28**(1), pp. 520-526.

[29] San Andrés, L., 1985, "Effect of Fluid Inertia Effect on Squeeze Film Damper Force Response," Ph.D. Dissertation, Texas A&M University, December.

[30] Arauz, G., 1993, "Experimental Study of a Grooved Squeeze Film Damper," M.S. Thesis, Texas A&M University, May.

[31] Tiwari, R., Lees, A. W., and Friswell, M.I., 2004, "Identification of Dynamic Bearing Parameters: A Review," Shock Vib. Dig., **36**(2) pp. 99-124.

[32] Fritzen, C.-P., 1986, "Identification of Mass, Damping, and Stiffness Matrices of Mechanical Systems," J. Vib. Acoust., **108**, pp. 9-16.

[33] San Andrés, L., 2012, "Liquid Cavitation in Fluid Film Bearings" Modern Lubrication Theory, Notes 6, Texas A & M University Digital Libraries, http://repository.tamu.edu/handle/1969.1/93197

[34] Walton II, J. F., Walovit, J. A., Zorzi, E. S., and Schrand, J. 1987, "Experimental Observation of Cavitating Squeeze-Film Dampers," ASME J. Tribol., **109**(2) pp. 290-295.

[35] Zeidan, F. Y, and Vance, J. M, 1989, "Cavitation Leading to a Two Phase Fluid in a Squeeze Film Damper," STLE Tribol. Trans., **32**, pp. 100-104.

[36] Zeidan, F. Y, and Vance, J. M, 1989, "Experimental Investigation of Cavitation Effects on the Squeeze Film Damper Force Coefficients ," Proc. of the 12th Biennial ASME Conference on Mechanical Vibration and Noise, Montreal, Canada., DE-18-1, pp. 237-242.

[37] Zeidan, F. Y, and Vance, J. M, 1990, "Cavitation and Air Entrainment Effects on the Response of Squeeze Film Support Rotors," ASME J. Tribology., **112**, pp.347-353

[38] Diaz, S., and San Andrés, L., 2001, "A Model for Squeeze Film Dampers Operating with Air Entrainment and Validation with Experiments," ASME J. Tribol., **123**(1), pp. 125-133.

[39] Diaz, S.E., and San Andrés, L., 2001, "Air Entrainment Versus Lubricant Vaporization in Squeeze Film Dampers: An Experimental Assessment of Their Fundamental Differences," ASME J. Eng. Gas Turbines and Power, **123**(4), pp. 871-877.

[40] Mendez, T. H., Ciaccia, M. A., Torres, J. E., and Diaz, S. E., 2010, "On the Numerical Prediction of Finite Length Squeeze Film Dampers Performance with Free Air Entrainment," ASME J. Eng. Gas Turbines Power, **132**(1), 012501

[41] Younan, A., Cao, J., Dimond, T., and Allaire, P., 2011, "Nonlinear Analysis of Squeeze Film Damper with Entrained Air in Rotordynamic Systems," STLE Tribol. Trans., **54**(2), pp. 132-144.

[42] Tao, L., Diaz, S., and San Andrés, L. (2000), "Analysis of Squeeze Film Dampers with Bubbly Lubricants," ASME J. Tribol., **122**, pp 205-210.

[43] Gehannin, J., Arghir, M., Bonneau, O., 2015, “A Volume oF Fluid METHOD for Air Ingestion in Squeeze Film Dampers,” Tribology Transactions (Accepted manuscript), DOI: 10.1080/10402004.2015.1023409.

[44] Adiletta, G., and Della Pietra, L., 2006, "Experimental Study of a Squeeze Film Damper with Eccentric Circular Orbits," ASME J. Tribol., **128(**2), pp. 365-377.

[45] Pan, C. H. T., and Tonessen, J., 1978, "Eccentric Operation of Squeeze-Film Damper," STLE J. Lubr. Tech., **2**(100), pp. 369-377.

[46] San Andrés, L., and De Santiago, O., 2004, “Forced Response of a Squeeze Film Damper and Identification of Force Coefficients from Large Orbital Motions,” ASME J. Tribol., **126**(2), pp.292-300.

APPENDIX A

TRANSFORMATION OF SHORT-LENGTH OPEN-ENDS MODEL LINEARIZED FORCE COEFFICIENTS

Table A.1. lists the linearized force coefficients for damper with 2π film (no cavitation) found in Table 1 of Ref. [A.1]. These are for small amplitude motions about a static eccentricity ε_s.

Ref. [A.1] defines ε_s as e_{sy}/c. Thus a coordinate transform of the coefficients by counter-clockwise (+) 45° is needed to represent those valid using the coordinates defined in the test rig in this thesis where e_s is along Θ=45°, see (in main text) Figure 2.

Table A. 1. Linearized force coefficients for short-length open-ends SFD undergoing small amplitude motions about static eccentricity ε_s [A.1].

Parameter	Relation
C_{XX}	$\frac{\pi\mu D}{2}\left(\frac{L}{c}\right)^3\left\{\frac{1+2\varepsilon_s^{\,2}}{\left(1-\varepsilon_s^{\,2}\right)^2}\right\}$
C_{YY}	$\frac{\pi\mu D}{2}\left(\frac{L}{c}\right)^3\left\{\frac{1}{\left(1-\varepsilon_s^{\,2}\right)^{3/2}}\right\}$
C_{XY}	0
C_{YX}	0
M_{XX}	$\frac{\pi\rho D}{12}\left(\frac{L^3}{c}\right)\left\{\frac{1-\left(1-\varepsilon_s^{\,2}\right)^{1/2}}{\varepsilon_s^{\,2}\left(1-\varepsilon_s^{\,2}\right)^{1/2}}\right\}$
M_{YY}	$\frac{\pi\rho D}{12}\left(\frac{L^3}{c}\right)\left\{\frac{1-\left(1-\varepsilon_s^{\,2}\right)^{1/2}}{\varepsilon_s^{\,2}}\right\}$
M_{XY}	0
M_{YX}	0

Transformation of the damping coefficients to the new coordinate system follows:

$$\bar{\mathbf{C}} = \mathbf{ACA}^{\mathrm{T}} \tag{A.1}$$

where $\bar{\mathbf{C}}$ represents the transformed damping coefficients valid for the coordinate system used in this thesis, and **A** is a transformation matrix. The following equations list the algebraic process for the transformation of the force coefficients.

$$\begin{bmatrix} \bar{C}_{XX} & \bar{C}_{XY} \\ \bar{C}_{YX} & \bar{C}_{YY} \end{bmatrix} = \begin{bmatrix} \cos(\Theta) & \sin(\Theta) \\ -\sin(\Theta) & \cos(\Theta) \end{bmatrix} \begin{bmatrix} C_{XX} & C_{XY} \\ C_{YX} & C_{YY} \end{bmatrix} \begin{bmatrix} \cos(\Theta) & -\sin(\Theta) \\ \sin(\Theta) & \cos(\Theta) \end{bmatrix} \tag{A.2}$$

Since C_{XY}= C_{YX} =0,

$$\begin{bmatrix} \bar{C}_{XX} & \bar{C}_{XY} \\ \bar{C}_{YX} & \bar{C}_{YY} \end{bmatrix} = \begin{bmatrix} C_{XX}\cos(\Theta) & C_{YY}\sin(\Theta) \\ -C_{XX}\sin(\Theta) & C_{YY}\cos(\Theta) \end{bmatrix} \begin{bmatrix} \cos(\Theta) & -\sin(\Theta) \\ \sin(\Theta) & \cos(\Theta) \end{bmatrix} \tag{A.3}$$

$$\begin{bmatrix} \bar{C}_{XX} & \bar{C}_{XY} \\ \bar{C}_{YX} & \bar{C}_{YY} \end{bmatrix} = \begin{bmatrix} C_{XX}\cos^2(\Theta) + C_{YY}\sin^2(\Theta) & -C_{XX}\sin(\Theta)\cos(\Theta) + C_{YY}\sin(\Theta)\cos(\Theta) \\ -C_{XX}\sin(\Theta)\cos(\Theta) + C_{YY}\sin(\Theta)\cos(\Theta) & C_{XX}\sin^2(\Theta) + C_{YY}\cos^2(\Theta) \end{bmatrix} \tag{A.4}$$

Substituting $\cos(45°)=\sin(45°)=\sqrt{2}/2$, and $\cos^2(45°)=\sin^2(45°)=1/2$, Eqn. (A.4) becomes:

$$\begin{bmatrix} \bar{C}_{XX} & \bar{C}_{XY} \\ \bar{C}_{YX} & \bar{C}_{YY} \end{bmatrix} = \begin{bmatrix} \frac{1}{2}(C_{XX} + C_{YY}) & \frac{1}{2}(C_{YY} - C_{XX}) \\ \frac{1}{2}(C_{YY} - C_{XX}) & \frac{1}{2}(C_{XX} + C_{YY}) \end{bmatrix} \tag{A.5}$$

Thus, it is obvious that

$$\begin{aligned} \bar{C}_{XX} &= \bar{C}_{YY} = \tfrac{1}{2}(C_{XX} + C_{YY}) \\ \bar{C}_{XY} &= \bar{C}_{YX} = \tfrac{1}{2}(C_{YY} - C_{XX}) \end{aligned} \tag{A.6}$$

Substituting the relations for C_{XX} and C_{YY} from Table A.1, the relations become:

$$\begin{aligned} \bar{C}_{XX} &= \bar{C}_{YY} = \frac{\mu D}{2}\left(\frac{\pi}{2}\right)\left(\frac{L}{c}\right)^3 \left\{ \frac{1+2\varepsilon_s^2}{\left(1-\varepsilon_s^2\right)^2} + \frac{1}{\left(1-\varepsilon_s^2\right)^{3/2}} \right\} \\ \bar{C}_{XY} &= \bar{C}_{YX} = \frac{\mu D}{2}\left(\frac{\pi}{2}\right)\left(\frac{L}{c}\right)^3 \left\{ \frac{1}{\left(1-\varepsilon_s^2\right)^{3/2}} - \frac{1+2\varepsilon_s^2}{\left(1-\varepsilon_s^2\right)^2} \right\} \end{aligned} \tag{A.7}$$

Further simplification results in:

$$\bar{C}_{XX} = \bar{C}_{YY} = \frac{\pi\mu D}{4}\left(\frac{L}{c}\right)^3 \left\{\frac{1+2\varepsilon_s{}^2+\left(1-\varepsilon_s{}^2\right)^{1/2}}{\left(1-\varepsilon_s{}^2\right)^2}\right\}$$
$$\bar{C}_{XY} = \bar{C}_{YX} = \frac{\pi\mu D}{4}\left(\frac{L}{c}\right)^3 \left\{\frac{\left(1-\varepsilon_s{}^2\right)^{1/2}-1-2\varepsilon_s{}^2}{\left(1-\varepsilon_s{}^2\right)^2}\right\} \quad \text{(A.8)}$$

Analysis of $\bar{C}_{XY}, \bar{C}_{YX}$ reveals that they are essentially nil for any static eccentricity $0 \leq \varepsilon_s < 0.86$, per the operating conditions used in this thesis.

In an identical fashion, the added mass coefficients are also transformed to the new coordinate system used in this thesis. Applying Eqns. (A.1-A.5), the transformed added mass coefficients are:

$$\bar{M}_{XX} = \bar{M}_{YY} = \tfrac{1}{2}(M_{XX} + M_{YY})$$
$$\bar{M}_{XY} = \bar{M}_{YX} = \tfrac{1}{2}(M_{YY} - M_{XX}) \quad \text{(A.9)}$$

Substituting the relations for M_{XX} and M_{YY} from Table A.1, the relations become:

$$\bar{M}_{XX} = \bar{M}_{YY} = \frac{\rho D}{2}\left(\frac{\pi}{12}\right)\left(\frac{L^3}{c}\right)\left\{\frac{1-\left(1-\varepsilon_s{}^2\right)^{1/2}}{\varepsilon_s{}^2\left(1-\varepsilon_s{}^2\right)^{1/2}} + \frac{1-\left(1-\varepsilon_s{}^2\right)^{1/2}}{\varepsilon_s{}^2}\right\}$$
$$\bar{M}_{XY} = \bar{M}_{YX} = \frac{\rho D}{2}\left(\frac{\pi}{12}\right)\left(\frac{L^3}{c}\right)\left\{\frac{1-\left(1-\varepsilon_s{}^2\right)^{1/2}}{\varepsilon_s{}^2} - \frac{1-\left(1-\varepsilon_s{}^2\right)^{1/2}}{\varepsilon_s{}^2\left(1-\varepsilon_s{}^2\right)^{1/2}}\right\} \quad \text{(A.10)}$$

Further simplification results in:

$$\bar{M}_{XX} = \bar{M}_{YY} = \frac{\pi\rho D}{24}\left(\frac{L^3}{c}\right)\left\{\frac{1}{\left(1-\varepsilon_s{}^2\right)^{1/2}}\right\}$$
$$\bar{M}_{XY} = \bar{M}_{YX} = \frac{\pi\rho D}{24}\left(\frac{L^3}{c}\right)\left\{\frac{2\left(1-\varepsilon_s{}^2\right)^{1/2}+\varepsilon_s{}^2-2}{\varepsilon_s{}^2\left(1-\varepsilon_s{}^2\right)^{1/2}}\right\} \quad \text{(A.11)}$$

As with the cross-coupled damping coefficients, analysis of $\bar{M}_{XY}, \bar{M}_{YX}$ reveals that they are essentially nil for any static eccentricity $0 \leq \varepsilon_s < 0.86$, per the operating conditions used in this thesis.

References

[A.1] San Andrés, L., 2012, "Squeeze Film Damper: Operation, Models and Technical Issues," Modern Lubrication Theory, Notes 13, Texas A&M University Digital Libraries, http://repository.tamu.edu/handle/1969.1/93197

APPENDIX B

IDENTIFICATION OF DRY SYSTEM STRUCTURAL PARAMETERS

Identification of the system structural force coefficients without lubricant (dry), K_s, C_s, M_s, is necessary for the identification of that generated by the squeeze film. Recall that four structural rods support the bearing cartridge (BC) and give the system a static stiffness. A static load test and a dynamic load test adequately determine the system dry parameters.

Figure B.1 presents the BC displacement versus the static load applied for the *X* and *Y* directions obtained from the static load test. The estimated structural stiffness along the *X* and *Y* axes are K_{SX}=12.77 MN/m and K_{SY}=12.36 MN/m, respectively.

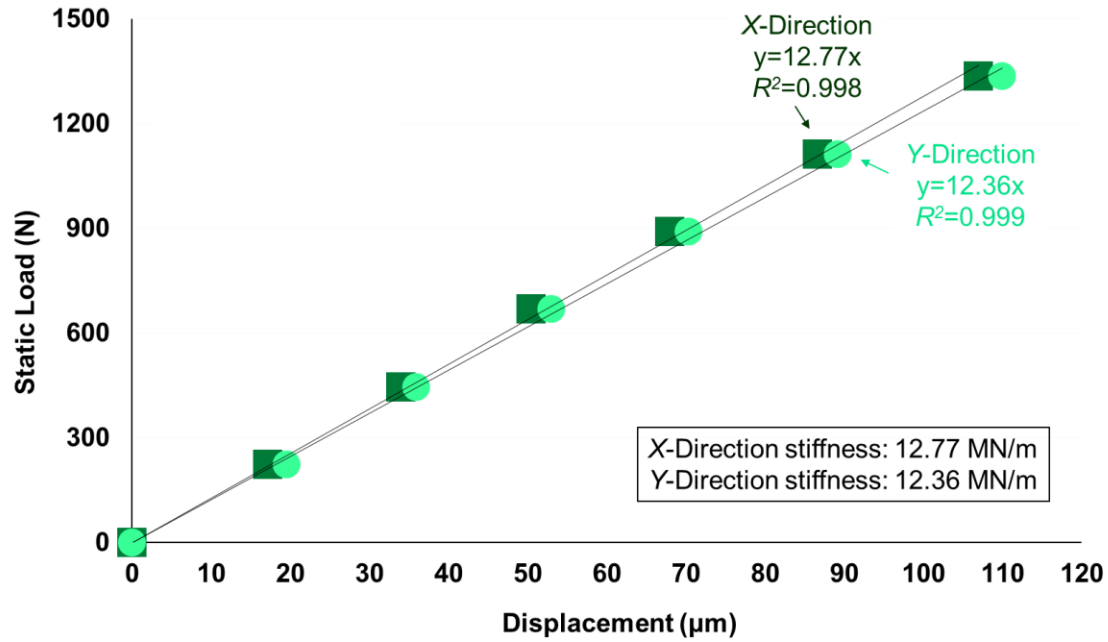

Figure B.1. Static load versus BC displacement and estimated structural stiffness along the *X*, and *Y* axes.

Figure B.2 shows identified system complex stiffness, **H**, obtained from the dynamic load test and *K-C-M* model (dashed lines) curve fits for the real and imaginary parts. The data is obtained from the SFD undergoing circular centered motions with orbit amplitude, r/c_1=0.1, and no lubricant (dry test). The goodness of fit R^2≈0.9 for the physical models shows the test data represent the system well. From the figure, it is clear that there is little remnant damping and added mass.

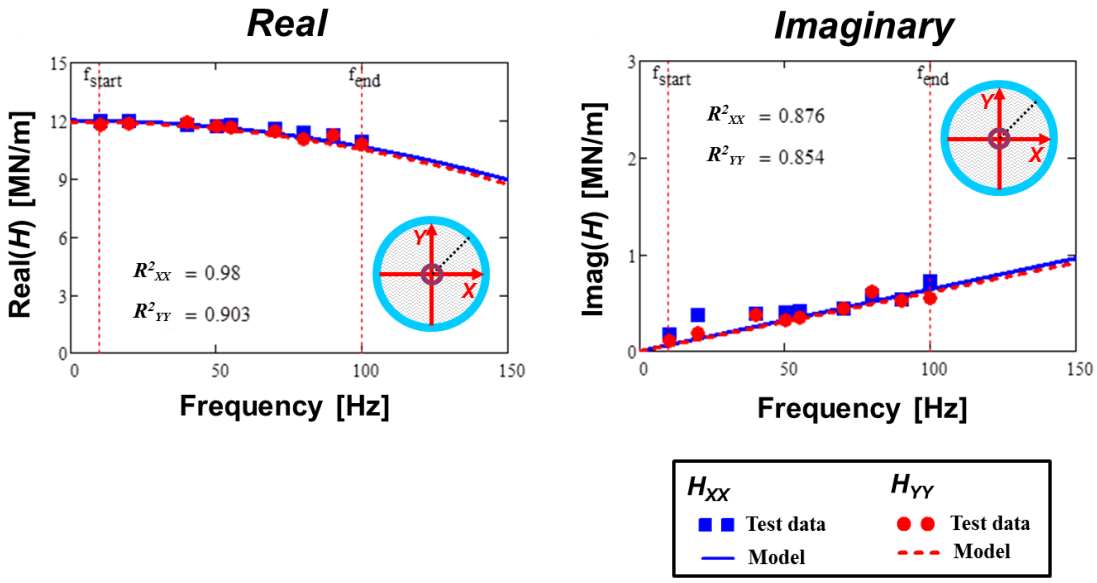

Figure B.2. Dry test system: Real and imaginary parts of the system direct complex stiffness (H_{XX}, H_{YY}) versus excitation frequency for dry circular orbit dynamic load tests. Data corresponds to e_s/c_1=0 and r/c_1=0.1.

Table B.1 lists the identified test system structural parameters (K_s, C_s, M_s) from the dynamic load test over a excitation frequency range from f_{start}=10 Hz to f_{end}=100 Hz. Dynamic load tests reveal K_{SXX}=12.0 MN/m and K_{SYY}=11.9 MN/m, approximately 6% smaller and 3% smaller than K_{SX} and K_{SY} (identified from the static load test), respectively.

Table B.1. System structural parameters obtained from circular orbit tests under a dry condition (no lubricant). Parameters identified from frequency range 10 Hz–100 Hz. Orbit amplitude r/c_1 = 0.05 and static eccentricity e_s/c_1 = 0.0.

Frequency range 10 - 100 Hz						
Structural parameter			**Direct**		**Cross-coupled**	
			XX	***YY***	***XY***	***YX***
Stiffness	K_S	[MN/m]	12.0	11.9	-0.32	-0.26
Damping	C_S	[kN·s/m]	1.33	1.40	0.07	0.09
Residual mass	M_S	[kg]	2.64	2.54	-0.05	-0.05
System Mass	M_{BC}	[kg]	15.15	15.15		
Natural frequency	f_n	[Hz]	132	131		
Damping ratio	ξ_S	[-]	0.02	0.01		

APPENDIX C

LUBRICANT PROPERTIES AND FILM FLOW CONDUCTANCE

Routine inspection of lubricant density and viscosity ensure that computational models use accurate values. Table C.1 presents manufacturer specifications for ISO VG2, the lubricant used in the SFD test rig.

Table C.1. Mobil Velocite™ No 3 (ISO VG 2) Manufacturer specification [C1]

	Mobil Velocite Oil Numbered Series No 3 (ISO VG 2)
cSt @ 40ºC	2.1
cSt @ 100ºC	0.95
Pour Point, ºC	-36
Flash Point, ºC	84
Density @ 15º C, kg/L	0.802

The measured density is ρ=802 kg/m^3, which is in agreement with manufacturer specifications. Figure C.1 shows measured lubricant viscosity versus temperature. The lubricant exhibits 2.4 cSt (1.92 cPoise) at 40°C and 3.31 cSt (2.65 cPoise) at room temperature 23^{o}C. Measured viscosity, as expected, is different from the manufacturer specifications, due to prolonged exposure to air entrainment events, and blending of multiple batches of lubricant.

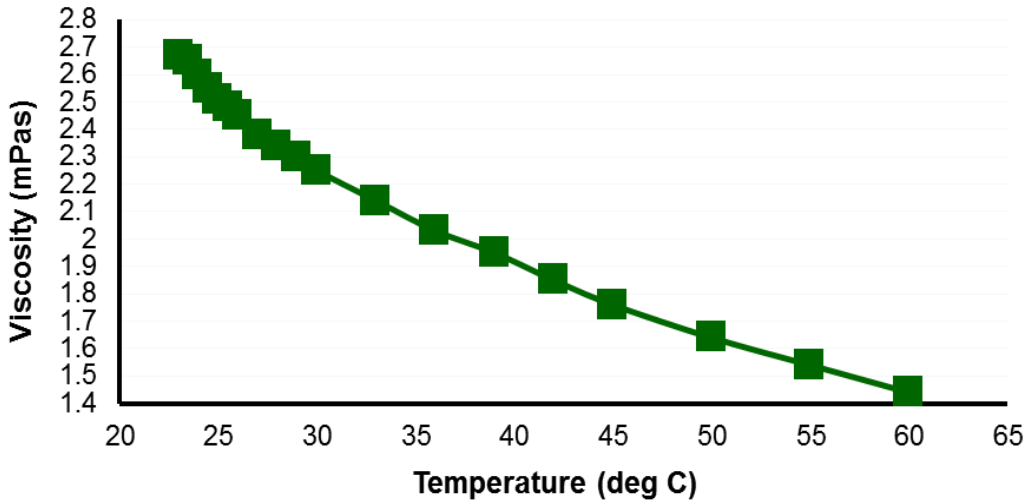

Figure C.1. Measured lubricant dynamic viscosity versus temperature.

Lubricant at a controlled pressure flows to the film land through three radial feedholes and exits to the top and bottom sections of the film land to ambient pressure. A turbine flow meter measures the lubricant inlet flow rate (Q_{in}) and a dial gauge pressure measures the inlet pressure (P_{in}) prior to entering the journal.

Table C.2. lists the recorded static pressures (P_{in}), flow rates, and ratio Q_B/Q_{in} for damper 1. The table also lists the flow conductance (C_{total}) which is equal to dQ/dP obtained from a linear regression of Q_{in} versus P_{in} (open-ends SFD has ambient pressure P_a=14.7 psia). Note the theoretical flow conductance is calculated as $Q_{in}/P_{in} - P_a$ = 0.133 LPM/kPa (2.22 mm^3/s/Pa), which is slightly larger than the experimentally measured flow conductance $dQ/dP = 0.086$ LPM/kPa.

Table C.2. Open-ends Damper 1 (c_1=0.267 mm) with hex socket orifice ϕ=2.54 mm. measured inlet pressures, lubricant flow rates, and flow conductance for ISO VG 2 oil at room temperature T_S=17°C.

P_{in} (kPa(g)) [±0.344]	Q_{in} (LPM) [±5%]
119.76	3.10
132.86	4.58
147.34	5.98
163.89	7.19
181.81	8.52
Flow conductance	dQ/dP ***(LPM/kPa)***
	0.086

References

[C.1] "Mobil Velocite™ No 3 (ISO VG 2) Manufacturer specification sheet", Hydraulic oils Typical Properties, Mobil, Accessed October 2013, http://www.mobil.com/USAEnglish/Lubes/PDS/GLXXENINDMOMobil_Velocite_Oil_Numbered.aspx

APPENDIX D

SYSTEM COMPLEX STIFFNESS FOR CIRCULAR CENTERED ORBIT TESTS

Figure D.1. through D.4 displays graphs of the real and imaginary parts of the system direct (H_{XX}, H_{YY}) and the cross-coupled (H_{XY}, H_{YX}) system complex stiffness obtained from the circular centered orbit tests with circular orbit amplitude r/c_1=0.02–0.73. The frequency range for the physical model curve-fits spans from f_{start}=10 Hz to f_{end}=100 Hz. Each graph displays the correlation coefficient (R^2) for the respective system complex stiffness.

Note that the cross-coupled (H_{XY}, H_{YX}) system complex stiffness generally exhibit low correlation coefficient $R^2 < 0.8$, which is expected since the cross-coupled force coefficients are generally orders of magnitude lower than their direct counterparts. Notice the cross-coupled R^2 increase with static eccentricity, which is in tandem with cross-coupled force coefficient magnitudes that increase with static eccentricity. In any event, system complex stiffness for other static eccentricity conditions ($e_s/c_1 \neq 0$) are omitted below for brevity.

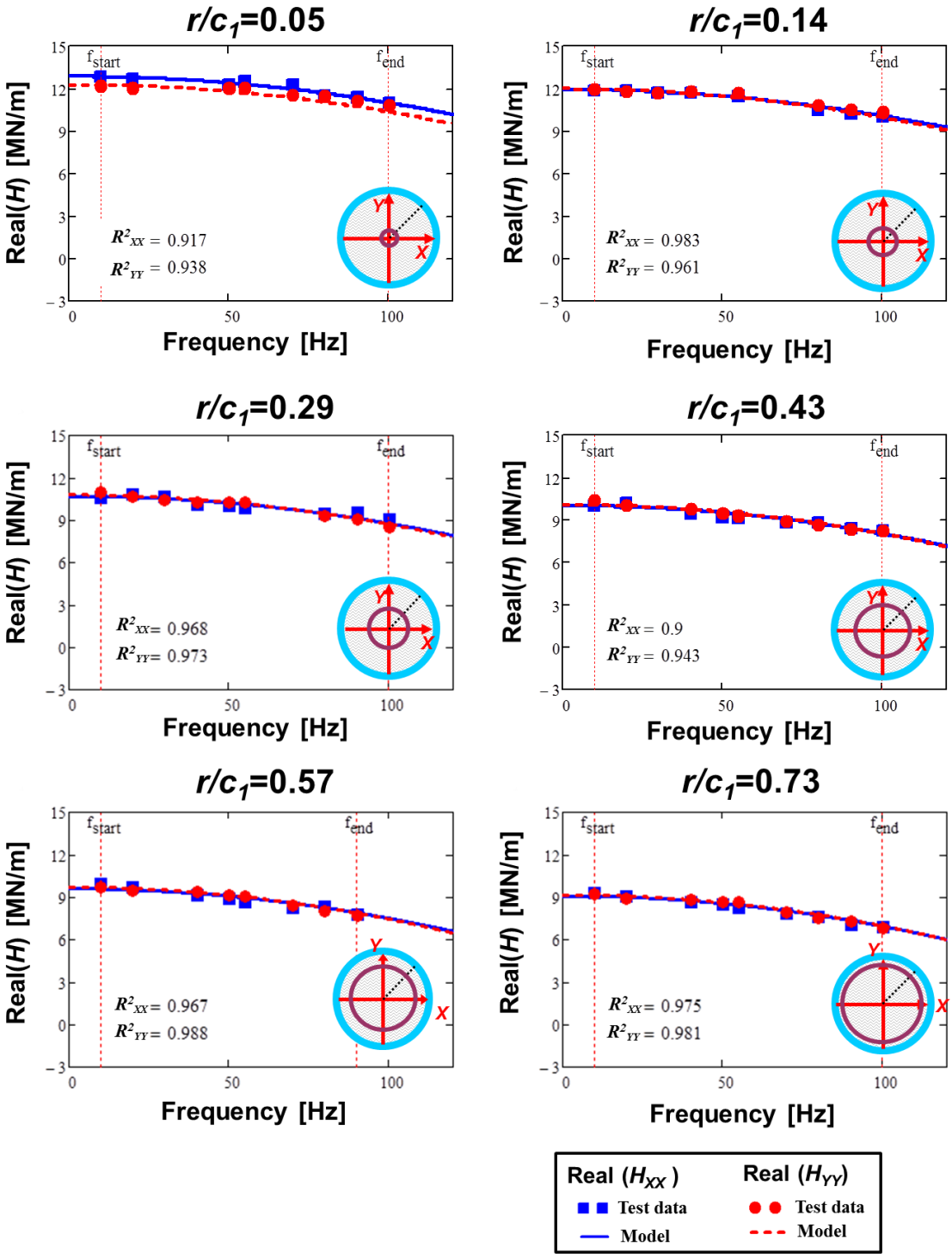

Figure D.1. Real part of direct complex stiffness (H_{XX}, H_{YY}) versus excitation frequency. Test data and corresponding physical model (K-$\omega^2 M$). Short length SFD (c_1=0.267 mm) with circular orbits of amplitude r/c_1=0.05–0.73 at static eccentricity $e_s=0.0c_1$.

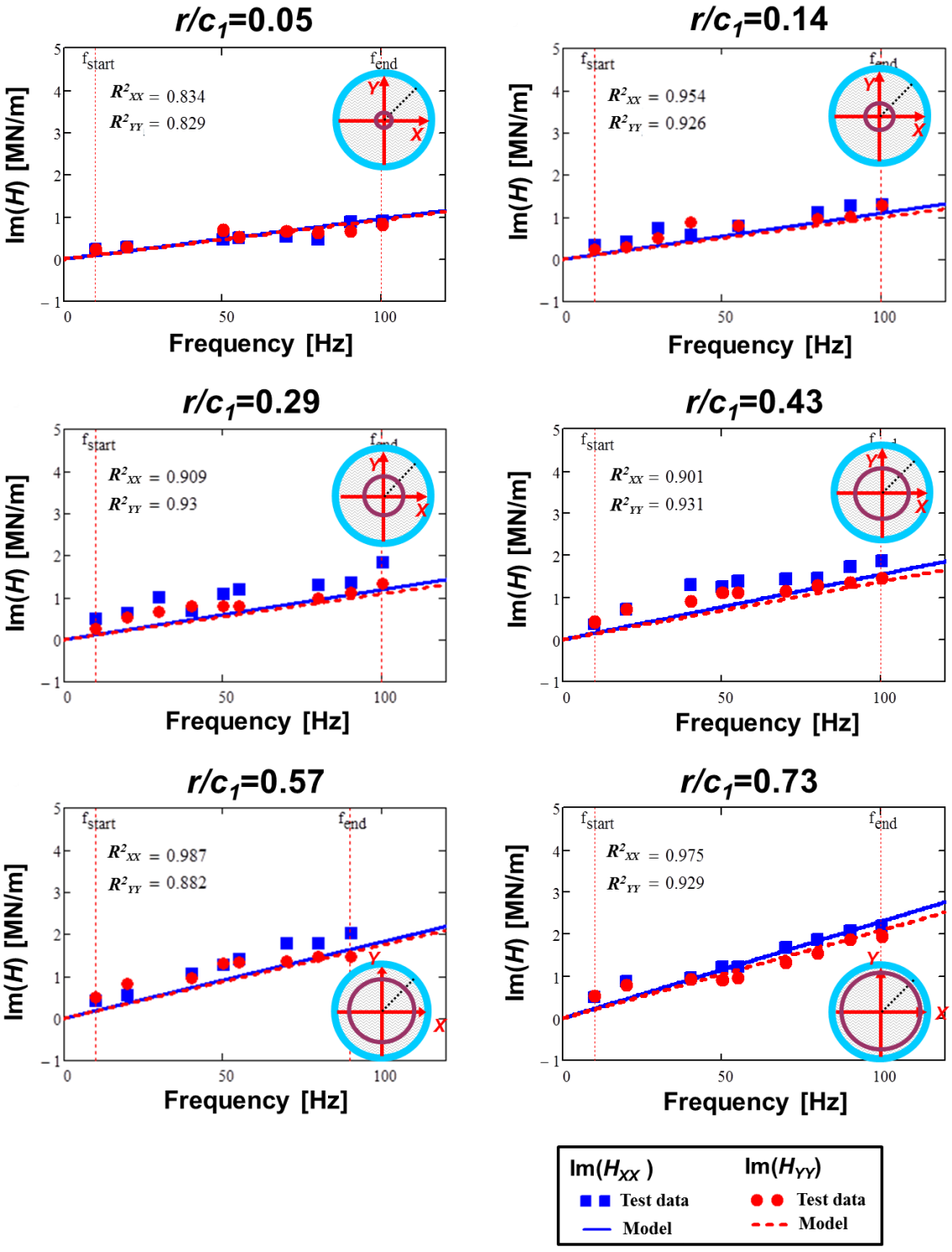

Figure D.2. Imaginary part of direct complex stiffness (H_{XX}, H_{YY}) versus excitation frequency. Test data and corresponding physical model ($C\omega$). Short length SFD (c_1=0.267 mm) with circular orbits of amplitude r/c_1=0.05–0.73 at static eccentricity $e_s=0.0c_1$.

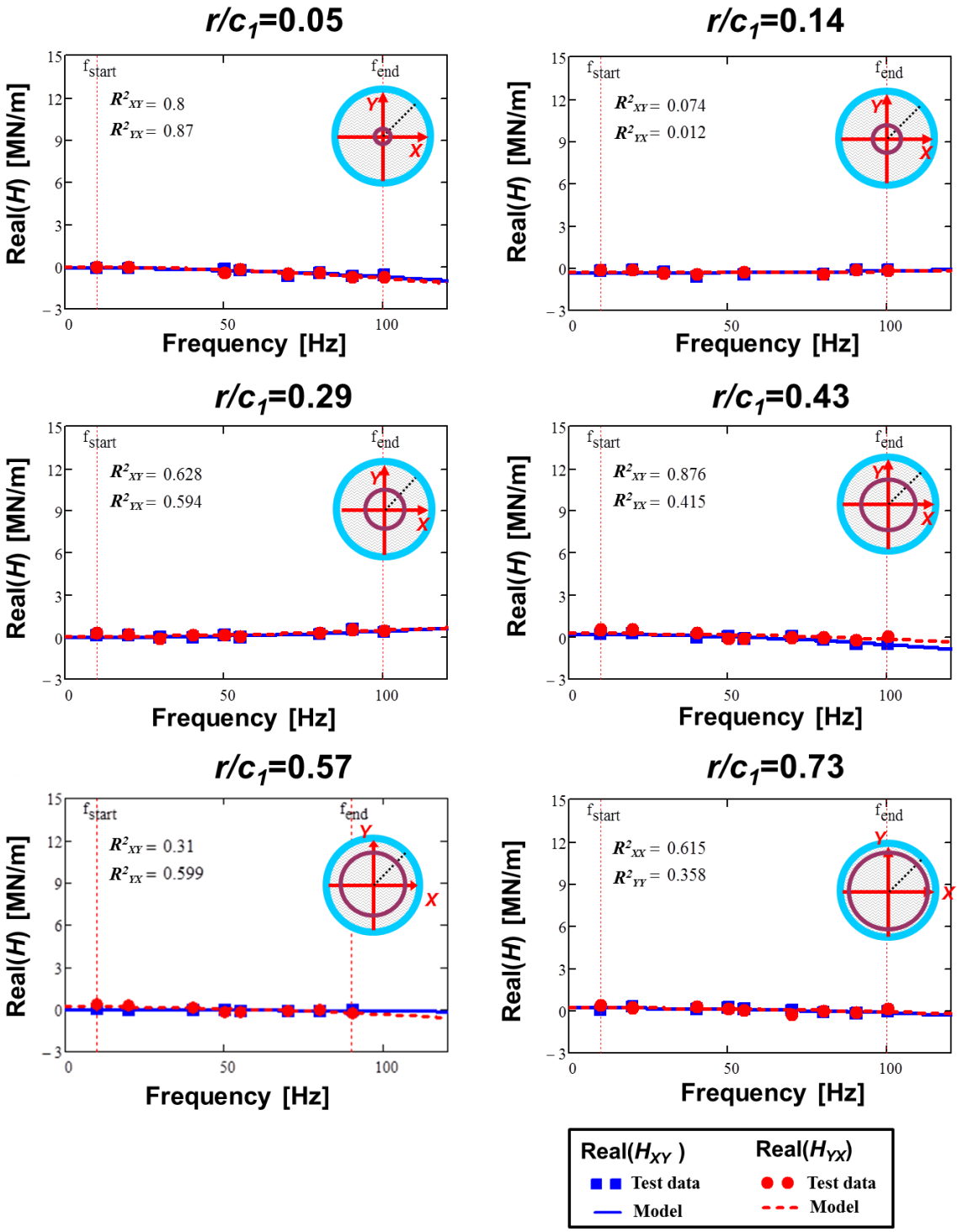

Figure D.3. Real part of cross-coupled complex stiffness (H_{XY}, H_{YX}) versus excitation frequency. Test data and corresponding physical model (K-$\omega^2 M$). Short length SFD (c_1=0.267 mm) with circular orbits of amplitude r/c_1=0.05–0.73 at static eccentricity $e_s=0.0c_1$.

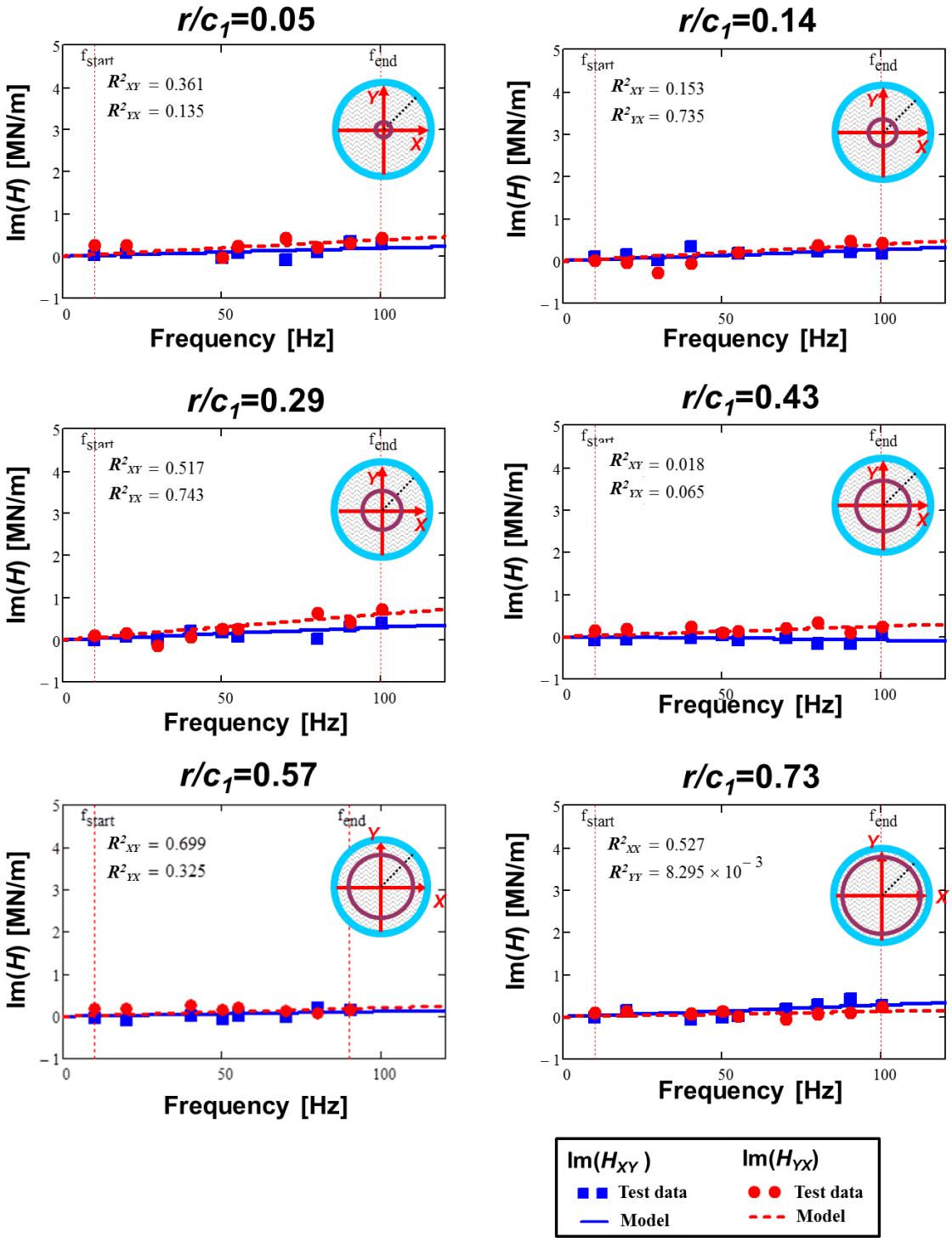

Figure D.4. Imaginary part of cross-coupled complex stiffness (H_{XY}, H_{YX}) versus excitation frequency. Test data and corresponding physical model ($C\omega$). Short length SFD (c_1=0.267 mm) with circular orbits of amplitude r/c_1=0.05–0.73 at static eccentricity $e_s=0.0c_1$.

APPENDIX E

TABULATED REAL AND IMAGINARY PART OF SYSTEM COMPLEX STIFFNESS CORRELATION COEFFICIENTS

For the short-length (L/D=0.2) open-ends SFD with c_1=0.267 mm and 2.54 cm single film land, Figure E.1. through E.6 list the correlation coefficients (direct and cross-coupled) obtained from the curve fit of the real and imaginary parts of the measured system complex stiffness.

Table E.1. Real part of SFD direct complex stiffness from circular orbits of amplitude r=12.7-191 μm at static eccentricities e_s=0.0-229 μm. Parameters identified over frequency range 10 – 100 Hz.

R^2_{XX}		Orbit Radius (r/c_1)					
		0.05	**0.14**	**0.29**	**0.43**	**0.57**	**0.71**
Static eccentricity (e_s/c_1)	**0.00**	0.917	0.983	0.87	0.9	0.921	0.975
	0.14	0.909	0.947	0.98	0.956	0.968	0.972
	0.29	0.876	0.974	0.954	0.931	0.971	
	0.43	0.906	0.927	0.931	0.954		
	0.57	0.906	0.911	0.915			
	0.71	0.875	0.88				
	0.86	0.919					

R^2_{YY}		Orbit Radius (r/c_1)					
		0.05	**0.14**	**0.29**	**0.43**	**0.57**	**0.71**
Static eccentricity (e_s/c_1)	**0.00**	0.938	0.961	0.973	0.943	0.988	0.981
	0.14	0.941	0.874	0.87	0.917	0.971	0.976
	0.29	0.808	0.961	0.914	0.856	0.951	
	0.43	0.928	0.948	0.96	0.978		
	0.57	0.926	0.831	0.908			
	0.71	0.852	0.847				
	0.86	0.886					

Table E.2. Imaginary part of SFD direct complex stiffness from circular orbits of amplitude r=12.7-191 μm at static eccentricities e_s=0.0-229 μm. Parameters identified over frequency range 10 – 100 Hz.

R^2_{XX}		Orbit Radius (r/c_1)					
		0.05	**0.14**	**0.29**	**0.43**	**0.57**	**0.71**
Static eccentricity (e_s/c_1)	**0.00**	0.834	0.954	0.864	0.901	0.987	0.975
	0.14	0.922	0.911	0.924	0.886	0.952	0.955
	0.29	0.93	0.953	0.938	0.833	0.976	
	0.43	0.87	0.842	0.94	0.94		
	0.57	0.823	0.948	0.93			
	0.71	0.852	0.864				
	0.86	0.948					

R^2_{YY}		Orbit Radius (r/c_1)					
		0.05	**0.14**	**0.29**	**0.43**	**0.57**	**0.71**
Static eccentricity (e_s/c_1)	**0.00**	0.829	0.885	0.93	0.931	0.882	0.929
	0.14	0.943	0.959	0.926	0.948	0.958	0.913
	0.29	0.778	0.917	0.809	0.934	0.953	
	0.43	0.908	0.827	0.776	0.917		
	0.57	0.841	0.904	0.826			
	0.71	0.891	0.835				
	0.86	0.975					

Table E.3. Real part of SFD cross-coupled complex stiffness from circular orbits of amplitude r=12.7-191 μm at static eccentricities e_s=0.0-229 μm. Parameters identified over frequency range 10 – 100 Hz.

R^2_{XY}		Orbit Radius (r/c_1)					
		0.05	**0.14**	**0.29**	**0.43**	**0.57**	**0.71**
Static eccentricity (e_s/c_1)	**0.00**	0.8	0.074	0.628	0.876	0.31	0.615
	0.14	0.822	0.516	0.308	0.354	0.524	0.769
	0.29	0.493	0.879	0.487	0.372	0.533	
	0.43	0.802	0.866	0.645	0.336		
	0.57	0.931	0.821	0.855			
	0.71	0.839	0.767				
	0.86	0.927					

R^2_{YX}		Orbit Radius (r/c_1)					
		0.05	**0.14**	**0.29**	**0.43**	**0.57**	**0.71**
Static eccentricity (e_s/c_1)	**0.00**	0.87	0.012	0.597	0.415	0.599	0.358
	0.14	0.332	0.915	0.725	0.666	0.885	0.708
	0.29	0.793	0.699	0.717	0.28	0.247	
	0.43	0.783	0.69	0.62	0.533		
	0.57	0.956	0.793	0.867			
	0.71	0.945	0.838				
	0.86	0.868					

Table E.4. Imaginary part of SFD cross-coupled complex stiffness from circular orbits of amplitude r=12.7-191 μm at static eccentricities e_s=0.0-229 μm. Parameters identified over frequency range 10 – 100 Hz.

R^2_{XY}		Orbit Radius (r/c_1)					
		0.05	**0.14**	**0.29**	**0.43**	**0.57**	**0.71**
Static eccentricity (e_s/c_1)	**0.00**	0.361	0.153	0.517	0.018	0.699	0.527
	0.14	0.182	0.004	0.053	0.046	0.198	0.195
	0.29	0.006	0	0.051	0.006	0.006	
	0.43	0.111	0.011	0.053	0.004		
	0.57	0.004	0.096	0.56			
	0.71	0.759	0.732				
	0.86	0.917					

R^2_{YX}		Orbit Radius (r/c_1)					
		0.05	**0.14**	**0.29**	**0.43**	**0.57**	**0.71**
Static eccentricity (e_s/c_1)	**0.00**	0.135	0.735	0.743	0.065	0.325	0.008
	0.14	0.897	0.011	0.193	0.245	0.021	0.411
	0.29	0.744	0.006	0.133	0.085	0.771	
	0.43	0.332	0.035	0.049	0.366		
	0.57	0.322	0.769	0.866			
	0.71	0.675	0.967				
	0.86	0.823					

APPENDIX F

UNCERTAINTY IN IDENTIFIED SFD FORCE COEFFICIENTS

This section outlines the calculation of uncertainty in identified SFD force coefficients. The total uncertainty consists of a bias (instrument) uncertainty, precision (curve fit) uncertainty, and variability. The procedure for each uncertainty is outlined, along with their combination into a total uncertainty for each force coefficient (K, C, M)$_{SFD}$. B, P, V, and U denote the bias, precision, variability, and total uncertainty, respectively. The following procedures for the precision and variability uncertainty also contain an example calculation for an individual operating condition.

It is important to note that each force coefficient has its own uncertainty, and is calculated accordingly[4]. Tables F.1-F.3 list the calculated total uncertainty for every SFD direct damping, added mass, and stiffness coefficient. Note that this section omits uncertainties for cross-coupled coefficients since the small magnitude of the cross-coupled coefficients causes their calculated uncertainty to be irrationally large.

Bias uncertainty

Bias uncertainty deals with uncertainty resulting from the resolution of the sensor and precision of a voltage acquisition system. Note that some of the following values are in English units per the manufacturers' specifications.

[4] A spreadsheet facilitates calculation of individual uncertainties.

- The data acquisition (DAQ) system (NI cDAQ-1972) uses NI 9215 Analog Input Modules for recording of voltage from the sensors. Ref. [F.1] specifies the NI 9215 as a 16-bit system, which translates to a resolution[5] of $^{10\,\mathrm{V}}\!/_{2^{16}} = 153\ \mu\mathrm{V}$.
- The DAQ board samples at a rate of 16,384 Hz, and stores 4096 samples, giving an uncertainty in the output frequency of 2 Hz for the entire frequency range [F.1]. This is equivalent to B_ω=20% at the lowest test frequency of 10 Hz, and B_ω=0.8% at the largest test frequency of 250 Hz, and an average of B_ω=3.1% across the entire range. Note, the following analysis considers the average B_ω=3.1%, because the force coefficients are best fit over the entire range. Note that actual uncertainty may be less than 3.1% since a Fourier series is used to express the recorded data in the frequency domain.
- As for the uncertainty of the X and Y – REBAM® (displacement) sensors, the DAQ system saves the sensor voltage to a precision of 153 μV. Based on calibration of the sensors' sensitivity: X=0.79 V/mil (31.1 mV/μm), Y=0.82 V/mil (32.3 mV/μm), 153 μV precision renders an uncertainty of $2\cdot10^{-4}$ mil. Using the smallest specified displacement over all the experiments will give the maximum bias uncertainty. This pertains to an orbit amplitude of r/c=0.05 (r=0.5 mil), which gives uncertainty in measurement of displacement as B_{DISP} = 0.04%.
- Based on the sensitivity of the PCB® load cells, 10 mV/lbf (2.25 mV/N), the DAQ precision (153 μV) renders a load cell uncertainty of $1.5\cdot10^{-2}$ lbf. The smallest recorded dynamic load amplitude, pertaining to orbit amplitude r/c=0.05, is 133 N (31 lbf). This gives uncertainty in measurement of dynamic load as B_{LOAD} = 0.05%.

[5] Note that the NI cDAQ-1972, however, can be configured to save measurements to precision of 1 mV.

- Based on the sensitivity of the PCB® accelerometer (100 mV/g), the DAQ precision (153 μV) renders an uncertainty of $1.5 \cdot 10^{-3}$ g. The smallest recorded acceleration amplitude, pertaining to orbit amplitude r/c=0.05 at a low whirl frequency is 0.2 g. This gives uncertainty in measurement of acceleration as B_{ACM} = 0.77%.
- For reference, the sensitivity of the PCB® piezoelectric pressure sensor, 1.45 mV/kPa (10 mV/psi), and the DAQ precision (153 μV) render an uncertainty of $1.5 \cdot 10^{-2}$ psi. Note, however, that identification of force coefficients does not incorporate measurement of dynamic pressure.

With these individual uncertainties, the propagation of uncertainty using the Kline-McClintock [F.2] procedure can be calculated. Knowledge of frequency domain relations $K \sim (F - M_{BC}a)/z$, $C \sim ((F - M_{BC}a)/z)\omega$, and $M \sim ((F - M_{BC}a)/z)\omega^2$ aids to determine the total bias uncertainty in force coefficients as

$$B_K = \sqrt{(B_{DISP})^2 + (B_{FORCE})^2 + (B_{ACC})^2} = 0.8\% \tag{F.1}$$

$$B_C = \sqrt{(B_{DISP})^2 + (B_{FORCE})^2 + (B_{ACC})^2 + (B_\omega)^2} = 3.1\% \tag{F.2}$$

$$B_M = \sqrt{(B_{DISP})^2 + (B_{FORCE})^2 + (B_{ACC})^2 + (2 \cdot B_\omega)^2} = 6.3\% \tag{F.3}$$

Recall, determination of the SFD force coefficient requires subtraction of the dry system coefficients from the lubricated system coefficients, i.e.

$$(\mathbf{K}, \mathbf{C}, \mathbf{M})_{SFD} = (\mathbf{K}, \mathbf{C}, \mathbf{M})_L - (\mathbf{K}, \mathbf{C}, \mathbf{M})_S \tag{F.4}$$

Therefore, propagation of the instrumentation bias uncertainty from two separate measurements into the SFD coefficient's bias is

$$B_{K_{SFD}} = \sqrt{(B_{K_S})^2 + (B_{K_L})^2} = \sim 0\% \tag{F.5}$$

$$B_{C_{SFD}} = \sqrt{(B_{C_S})^2 + (B_{C_L})^2} = 4.4\% \tag{F.6}$$

$$B_{M_{SFD}} = \sqrt{(B_{M_S})^2 + (B_{M_L})^2} = 8.9\% \tag{F.7}$$

Precision uncertainty

Plotting the real and imaginary part of the measured complex stiffness versus frequency gives plots as those shown in Figure F.1. Extracting the *Y*-intercept and the curvature of the real part produces, respectively, the stiffness coefficient (*K*) and the mass coefficient (*M*). The slope of the imaginary part of the measured complex stiffness produces the estimated damping coefficient (*C*).

The precision uncertainty associated with a least squares curve fit is:

$$\varphi_{fit} = t \cdot S \tag{F.8}$$

where *t* is the student's *t*-distribution value 1.83 pertaining to a 95% confidence interval [F.3], *S* is the estimated standard deviation based upon engineering knowledge. Ref [F.2] gives relations for estimated standard deviation (*S*) of the intercept and slope of a least squares fit line as:

$$S_{Intercept} = \sqrt{\frac{1}{N(N-2)}\frac{1-r^2}{r^2}} \tag{F.9}$$

$$S_{Slope} = \sqrt{\frac{1}{(N-2)}\frac{1-r^2}{r^2}} \tag{F.10}$$

where *N* is the number of points (ten) used for the curve fit and r^2 is the goodness of curve fit.

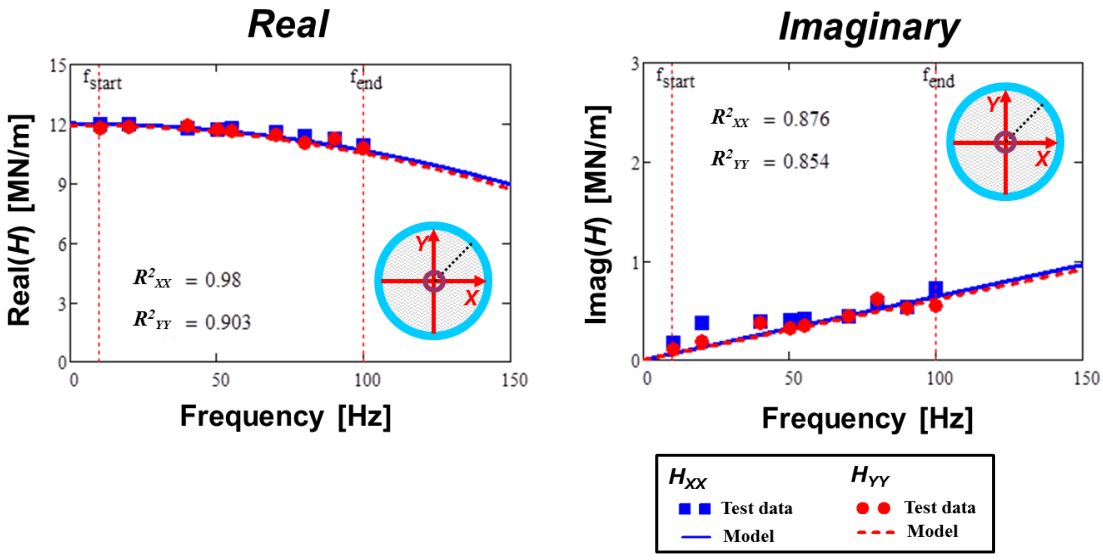

Figure F.1. Plots of real (a) and imaginary (b) parts of mechanical complex stiffness versus frequency (ω). Curve fit and measured data shown

Using an example case for operating condition, e_s/c=0.86, r/c=0.05, with N=10 and r^2 values as tabulated in Appendix E, the uncertainty of the SFD direct (XX) coefficients are:

$$\varphi_{K_{XX\,SFD}} = 0.011 \text{ MN/m } (0.061 \text{ klbf/in}) \tag{F.11}$$

$$\varphi_{C_{XX\,SFD}} = 0.027 \text{ kN·s/m } (0.152 \text{ lbf·s/m}) \tag{F.12}$$

$$\varphi_{M_{XX\,SFD}} = 0.087 \text{ kg } (0.192 \text{ lbm}) \tag{F.13}$$

These pertain to precision uncertainties:

$$P_{K_{SFD}} = \frac{\varphi_{K_{XX\,SFD}}}{K_{XX\,SFD}} = \frac{0.011}{4.187} = 0.3\% \tag{F.14}$$

$$P_{C_{SFD}} = \frac{\varphi_{C_{XX\,SFD}}}{C_{XX\,SFD}} = \frac{0.027}{3.236} = 0.8\% \tag{F.15}$$

$$P_{M_{SFD}} = \frac{\varphi_{M_{XX\,SFD}}}{M_{XX\,SFD}} = \frac{0.087}{4.955} = 1.8\% \tag{F.16}$$

Uncertainty due to variability

Uncertainty from variability deals with the repeatability of measurements. In an effort assess the repeatability of the identified *K*, *C*, *M* coefficients, several of the operating conditions included three sets of experiments to calculate the standard deviation of the force coefficient among the three experiments. Note that a weighted average (a function of r/c and e_s/c) of the measured standard deviations delivered those for the operating conditions without three experiments.

The estimation of uncertainty pertaining to the variability of the force coefficients from the averaging of multiple test results is [F.2]:

$$\varphi_{var} = t \cdot S \tag{F.17}$$

where *t* is the student's *t*-distribution value 1.83 corresponding to a 95% confidence interval [F.3], and S is the precision index of the averaged result and follows given by Ref. [F.2]:

$$S = \hat{S} \Big/ \bar{X}\sqrt{M} \tag{F.18}$$

where $\hat{S}$ is the standard deviation among the tests, $\bar{X}$ is the mean value, and *M* is the number of tests, three.

Using again the example case for operating condition, e_s/c=0.86, r/c=0.05, the uncertainty of the SFD direct (*XX*) coefficients among the three experiments are:

$$\varphi_{K_{XX\,SFD}} = 0.017 \text{ MN/m } (0.097 \text{ klbf/in}) \tag{F.19}$$

$$\varphi_{C_{XX\,SFD}} = 0.100 \text{ kN·s/m } (0.571 \text{ lbf·s/in}) \tag{F.20}$$

$$\varphi_{M_{XX\,SFD}} = 0.287 \text{ kg } (0.637 \text{ lbm}) \tag{F.21}$$

These pertain to variability uncertainties:

$$V_{K_{SFD}} = \frac{\varphi_{K_{XX\ SFD}}}{K_{XX\ SFD}} = \frac{0.017}{4.187} = 0.4\% \quad \text{(F.22)}$$

$$V_{C_{SFD}} = \frac{\varphi_{C_{XX\ SFD}}}{C_{XX\ SFD}} = \frac{0.100}{3.236} = 3.1\% \quad \text{(F.23)}$$

$$V_{M_{SFD}} = \frac{\varphi_{M_{XX\ SFD}}}{M_{XX\ SFD}} = \frac{0.287}{4.955} = 5.8\% \quad \text{(F.24)}$$

Total uncertainty

As a result of bias, precision, and variability uncertainty, the final (total) uncertainty in each SFD force coefficients is:

$$U_{K_{SFD}} = \sqrt{(B_{K_{SFD}})^2 + (P_{K_{SFD}})^2 + (V_{K_{SFD}})^2} \quad \text{(F.25)}$$

$$U_{C_{SFD}} = \sqrt{(B_{C_{SFD}})^2 + (P_{C_{SFD}})^2 + (V_{C_{SFD}})^2} \quad \text{(F.26)}$$

$$U_{M_{SFD}} = \sqrt{(B_{M_{SFD}})^2 + (P_{M_{SFD}})^2 + (V_{M_{SFD}})^2} \quad \text{(F.27)}$$

Using again the example case for operating condition, e_s/c=0.86, r/c=0.05, the final uncertainty of the SFD direct (*XX*) coefficients are:

$$U_{K_{XX\ SFD}} = \sqrt{0^2 + 0.3^2 + 0.4^2} = 0.5\% \quad \text{(F.28)}$$

$$U_{C_{XX\ SFD}} = \sqrt{4.4^2 + 0.8^2 + 3.1^2} = 5.5\% \quad \text{(F.29)}$$

$$U_{M_{XX\ SFD}} = \sqrt{8.9^2 + 1.8^2 + 5.8^2} = 10.8\% \quad \text{(F.30)}$$

Again, the author stresses that calculation of the uncertainty takes place for each force coefficient over each operating condition. Tables F.1-F.3 list the calculated total uncertainty for every SFD direct damping, added mass, and stiffness coefficient.

Tabulated Uncertainty for SFD Direct K, C, M Coefficients

Table F.1. Total uncertainties for the SFD direct stiffness coefficients from circular orbits of amplitude r=12.7-191 μm at static eccentricities e_s=0.0-229 μm.

K_{XX}		Orbit Radius (r/c_1)					
		0.05	**0.14**	**0.29**	**0.43**	**0.57**	**0.71**
Static eccentricity (e_s/c_1)	**0.00**	2.5%	8.5%	3.0%	2.9%	3.1%	3.2%
	0.14	4.5%	2.7%	2.1%	2.4%	2.3%	2.6%
	0.29	2.5%	0.9%	1.4%	1.7%	1.8%	
	0.43	1.0%	0.7%	1.0%	1.2%		
	0.57	0.6%	0.5%	0.8%			
	0.71	0.6%	0.5%				
	0.86	0.5%					

K_{YY}		Orbit Radius (r/c_1)					
		0.05	**0.14**	**0.29**	**0.43**	**0.57**	**0.71**
Static eccentricity (e_s/c_1)	**0.00**	5.7%	14.9%	3.3%	3.1%	3.3%	3.3%
	0.14	9.1%	2.0%	2.1%	2.2%	2.3%	2.6%
	0.29	1.7%	0.9%	1.3%	1.8%	1.8%	
	0.43	1.1%	0.7%	1.0%	1.3%		
	0.57	0.7%	0.7%	0.8%			
	0.71	0.7%	0.6%				
	0.86	0.6%					

Table F.2. Total uncertainties for the SFD direct damping coefficients from circular orbits of amplitude r=12.7-191 μm at static eccentricities e_s=0.0-229 μm.

C_{XX}		Orbit Radius (r/c_1)					
		0.05	**0.14**	**0.29**	**0.43**	**0.57**	**0.71**
Static eccentricity (e_s/c_1)	**0.00**	12.2%	8.5%	10.0%	7.7%	7.0%	6.4%
	0.14	10.2%	9.1%	9.1%	7.4%	5.8%	6.0%
	0.29	10.4%	7.6%	7.7%	8.6%	6.6%	
	0.43	8.4%	8.5%	6.9%	6.2%		
	0.57	8.4%	5.8%	6.2%			
	0.71	6.6%	5.7%				
	0.86	5.5%					

C_{YY}		Orbit Radius (r/c_1)					
		0.05	**0.14**	**0.29**	**0.43**	**0.57**	**0.71**
Static eccentricity (e_s/c_1)	**0.00**	12.3%	11.1%	10.5%	8.6%	7.5%	6.9%
	0.14	8.2%	7.9%	7.5%	6.7%	6.2%	6.8%
	0.29	13.2%	8.7%	8.2%	6.3%	6.1%	
	0.43	8.4%	9.1%	8.6%	6.1%		
	0.57	9.6%	6.9%	7.0%			
	0.71	6.7%	6.0%				
	0.86	5.5%					

Table F.3. Total uncertainties for the SFD direct added mass coefficients from circular orbits of amplitude r=12.7-191 μm at static eccentricities e_s=0.0-229 μm.

M_{XX}		Orbit Radius (r/c_1)					
		0.05	**0.14**	**0.29**	**0.43**	**0.57**	**0.71**
Static eccentricity (e_s/c_1)	**0.00**	13.4%	13.2%	15.4%	15.5%	15.4%	16.2%
	0.14	14.4%	14.2%	12.1%	12.1%	11.9%	12.2%
	0.29	15.0%	11.9%	12.1%	11.2%	11.1%	
	0.43	11.1%	10.9%	10.8%	10.3%		
	0.57	11.2%	10.4%	10.5%			
	0.71	11.5%	11.6%				
	0.86	10.8%					

M_{YY}		Orbit Radius (r/c_1)					
		0.05	**0.14**	**0.29**	**0.43**	**0.57**	**0.71**
Static eccentricity (e_s/c_1)	**0.00**	13.1%	12.7%	12.8%	14.7%	13.7%	16.3%
	0.14	16.3%	21.7%	16.5%	12.9%	13.7%	14.2%
	0.29	16.9%	15.4%	15.8%	13.9%	13.5%	
	0.43	11.6%	12.2%	12.2%	11.7%		
	0.57	11.7%	13.1%	12.0%			
	0.71	12.4%	13.2%				
	0.86	11.4%					

References

[F.1] National Instruments, Operating Instructions and Specifications NI 9215, May 2011, http://www.ni.com/pdf/manuals/373779f.pdf

[F.2] Coleman, H.W., and Steele, G.W., 1998, *Experimentation and Uncertainty Analysis for Engineers*, John Wiley & Sons, New York.

[F.3] Beckwith, T., Marangoni, R., and Lienhard, J. 1993, "Mechanical Measurements", Prentice Hall, 5th edition, pp. 82

APPENDIX G

COMPARISON OF RECORDED DYNAMIC FILM PRESSURES FROM DAMPERS 1, 2, AND 3

The following figures depict comparisons of the *peak-to-peak* (*p-p*) dynamic pressures recorded at the top/bottom end planes, top/bottom half-planes, and mid-plane versus whirl frequency (ω) between dampers 1 and 2 and dampers 1 and 3. Recall that the lubricant supply upstream of the feedholes is maintained at P_{in}~0.36 bar, Q_{in}~5.10 LPM for damper 1; P_{in}~1.86 bar, Q_{in}~6.1 LPM for damper 2; and P_{in}~0.35 bar, Q_{in}~5.06 LPM for damper 3.

Note that similar (magnitude and shape) film *p-p* pressures recorded in the top and bottom half-planes (z=+¼L) P_2 and P_3, mid-plane (z=0 cm) P_1 and P_4, and the top and bottom ends P_7 and P_8 demonstrate the BC is centered (e_s/c=0).

Dampers 1 and 2

Figure G.1 compares the *p-p* dynamic pressures versus whirl frequency (ω) for a centered condition (e_s=0). For both dampers 1 and 2, the data corresponds to circular centered orbits of r/c=0.3. Notice, however, that the orbit amplitude for damper 1 is r=76 μm, twice that for damper 2, r=38 μm due to damper 2 having a smaller clearance. The figure demonstrates the pressures exhibited by both dampers for equal orbit amplitude to clearance ratio r/c=0.3 are close in magnitude; pressures in damper 1 are generally only slightly smaller than the pressures in damper 2, albeit the mid-plane pressures in damper 1 are notably smaller than the pressures in damper 2 at higher whirl frequencies. For the

larger clearance damper 1 (c_1=0.267 mm), the dynamic pressures were recorded to a maximum excitation frequency ω=200 Hz. This frequency is lower than the maximum frequency of 250 Hz for the smaller clearance damper 2 (c_2=0.122 mm) due to the load limit of the shakers.

On the other hand, Figure G.2 presents comparison of the *p-p* dynamic pressures versus whirl frequency for tests at a centered condition (e_s=0) and equal orbit radius, r=38 μm. Here, r/c_1=0.14 and r/c_2=0.31. In this case, the pressures exhibited in damper 2 are drastically larger than the pressures measured in damper 1, ~three times larger.

The pressures in both figures do not monotonically increase with whirl frequency, demonstrating the occurrence of air ingestion. In conclusion, among similarly configured SFDs with varying clearance, whirl orbits with the same amplitude to clearance ratio r/c likely produce pressures similar in magnitude. However, as expected, for equal orbit radii (r), smaller clearance SFDs produce larger pressures.

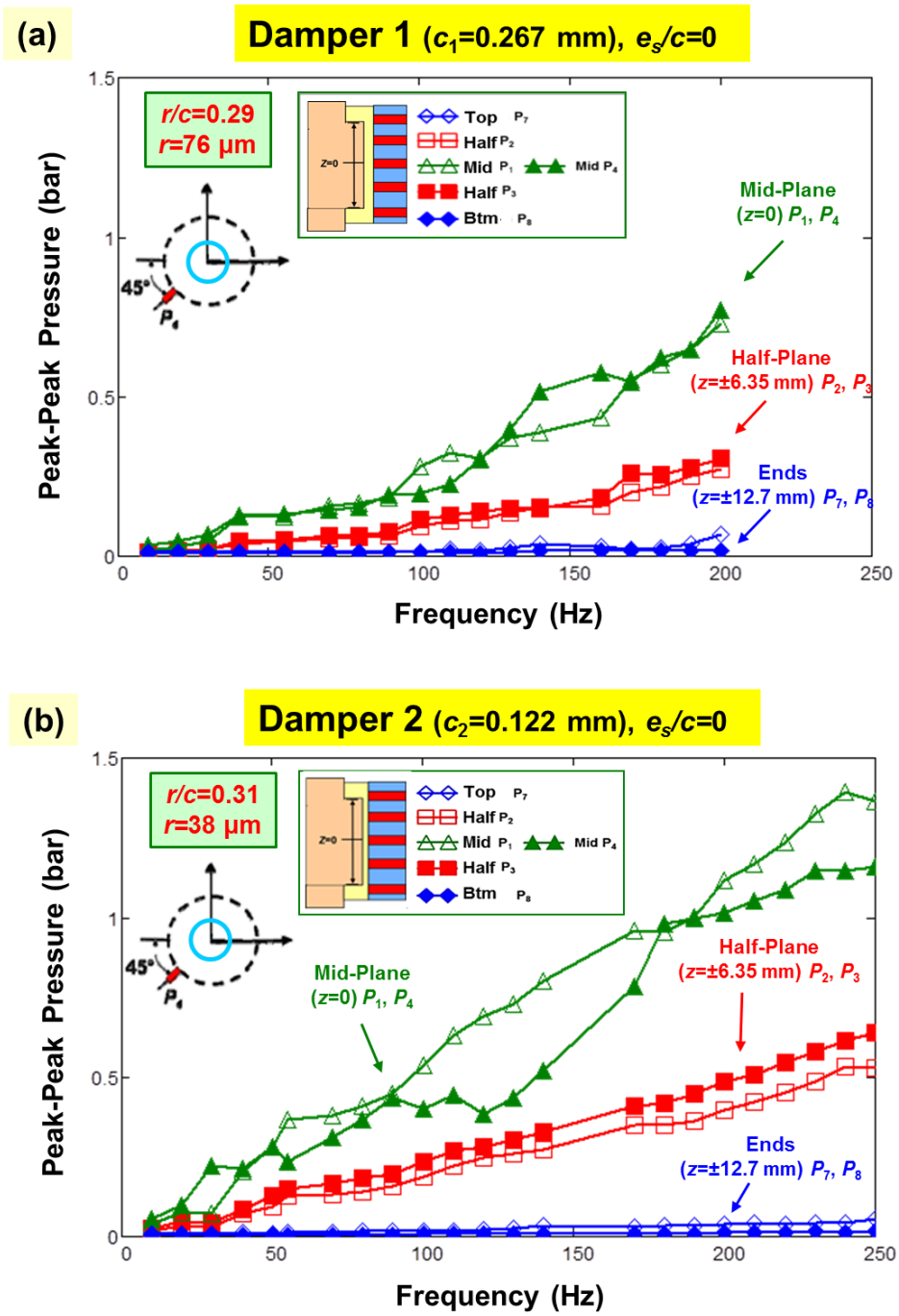

Figure G.1. Open-ends SFDs: Recorded *peak-to-peak* film dynamic pressures versus excitation frequency (ω) for (a) damper 1 (c_1=0.267 mm) and (b) damper 2 (c_2=0.122 mm). Centered (e_s=0) circular orbit tests with *r/c*≈0.30 (orbit amplitude/clearance). Measurements at the damper mid-plane, top and bottom half-planes, and bottom end groove. (Insets shows location of pressure sensors along film land, and show journal position relative to the BC).

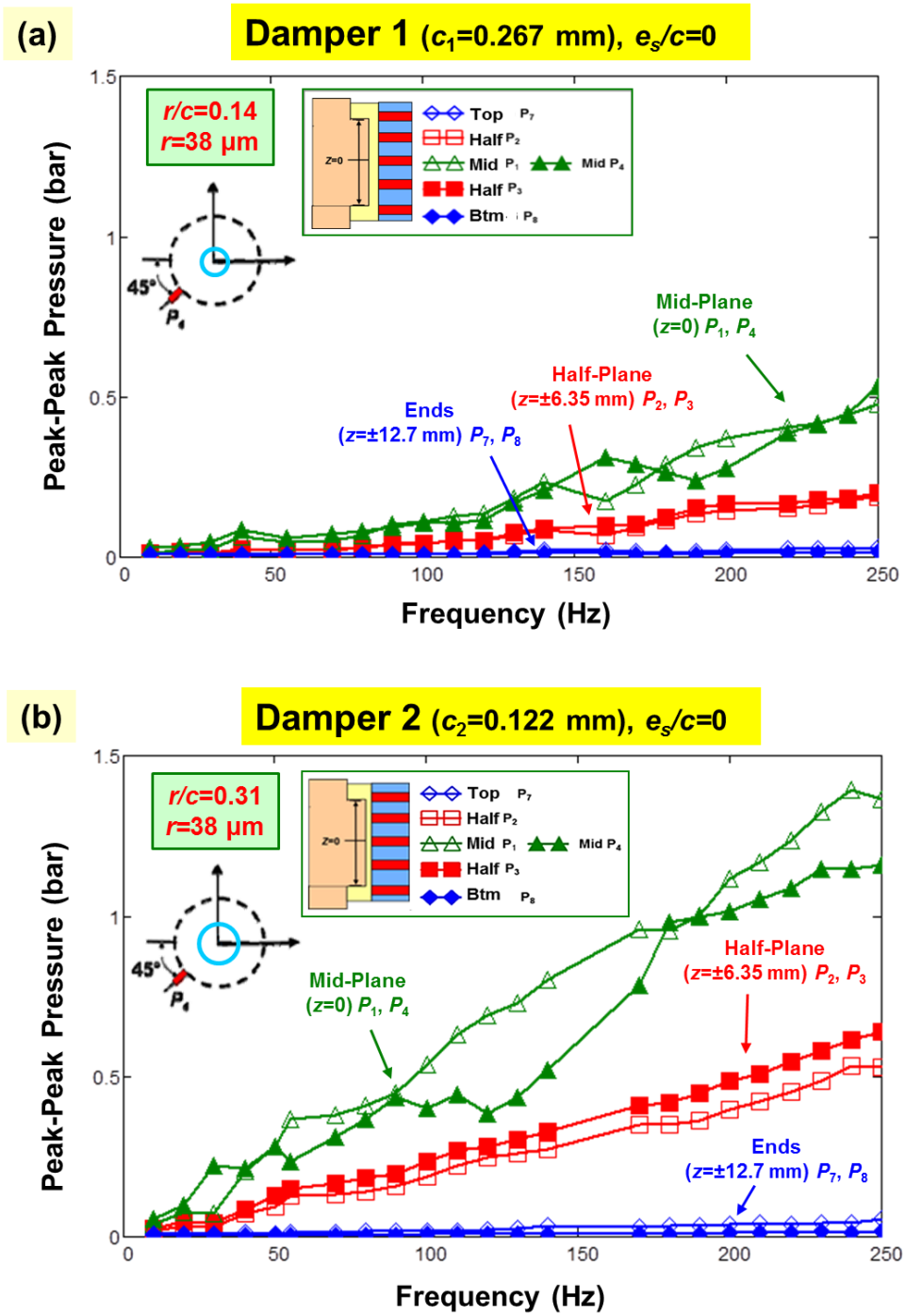

Figure G.2. Open-ends SFDs: Recorded *peak-to-peak* film dynamic pressures versus excitation frequency (ω) for (a) damper 1 (c_1=0.267 mm) and (b) damper 2 (c_2=0.122 mm). Centered (e_s=0) circular orbit tests with orbit amplitudes r_1=38 μm and r_2=38 μm. Measurements at the damper mid-plane, top and bottom half-planes, and bottom end groove. (Insets shows location of pressure sensors along film land, and show journal position relative to the BC).

Dampers 1 and 3

Figure G.3 presents comparisons of the *p-p* dynamic pressures for dampers 1 and 3 versus whirl frequency (ω) for motions at a centered condition (e_s=0) with orbit amplitude r=38 μm, or r/c=~0.15 (recall damper 1 has a slightly larger clearance than that of damper 3). Damper 3 with slightly smaller clearance and larger (effective) film land length ($L_{3\text{-}eff}$=0.297 cm) exhibits, as expected, larger pressures (50% higher) than damper 1. Notice that the pressures in the end grooves of damper 3 are not nil, whereas in damper 1, the pressures at the ends (with no grooves) are zero. The measurements thus further evidence the generation of dynamic film pressures in large clearance regions (end grooves) next to the squeeze film land. Hence, for damper 3, this led to the need to consider a larger effective film land length than the actual film land length ($L_{3\text{-}eff} > L_3$).

Figure Figure G.4 compares the *p-p* dynamic pressures versus whirl frequency for a largely off centered, e_s=191 μm, orbit with amplitude r=38 μm, or r/c=~0.15. For both dampers 1 and 3, the P_4 pressure is significantly larger than the pressures at other locations since the P_4 sensor is at the location of minimum film thickness as the static eccentricity (e_s) displaces along the Θ=45°. The *p-p* dynamic pressures in damper 3 are generally ~1.5 times larger than the pressures in damper 1.

The test results shown in the figures, as with prior measurements, also evidence that air ingestion occurs during SFD operation as the *p-p* dynamic pressures do not monotonically increase with frequency.

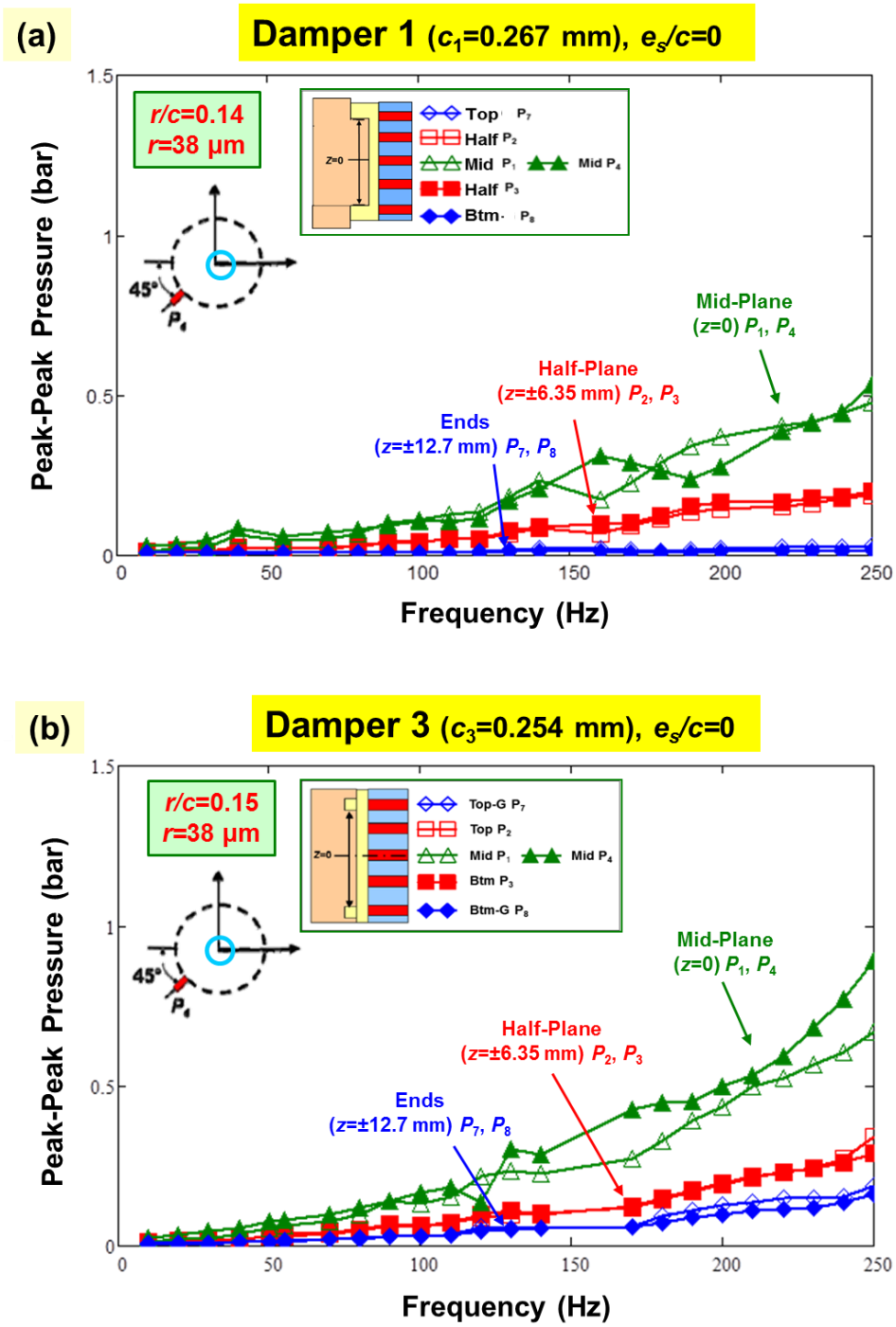

Figure G.3. Open-ends SFDs: Recorded *peak-to-peak* film dynamic pressures versus excitation frequency (ω) for (a) damper 1 (c_1=0.267 mm) and (b) damper 3 (c_3=0.254 mm). Centered (e_s=0) circular orbit tests with radius r/c=0.15. Measurements at the damper mid-plane, top and bottom half-planes, and bottom end groove. (Insets show location of pressure sensors along film land and journal position relative to the BC).

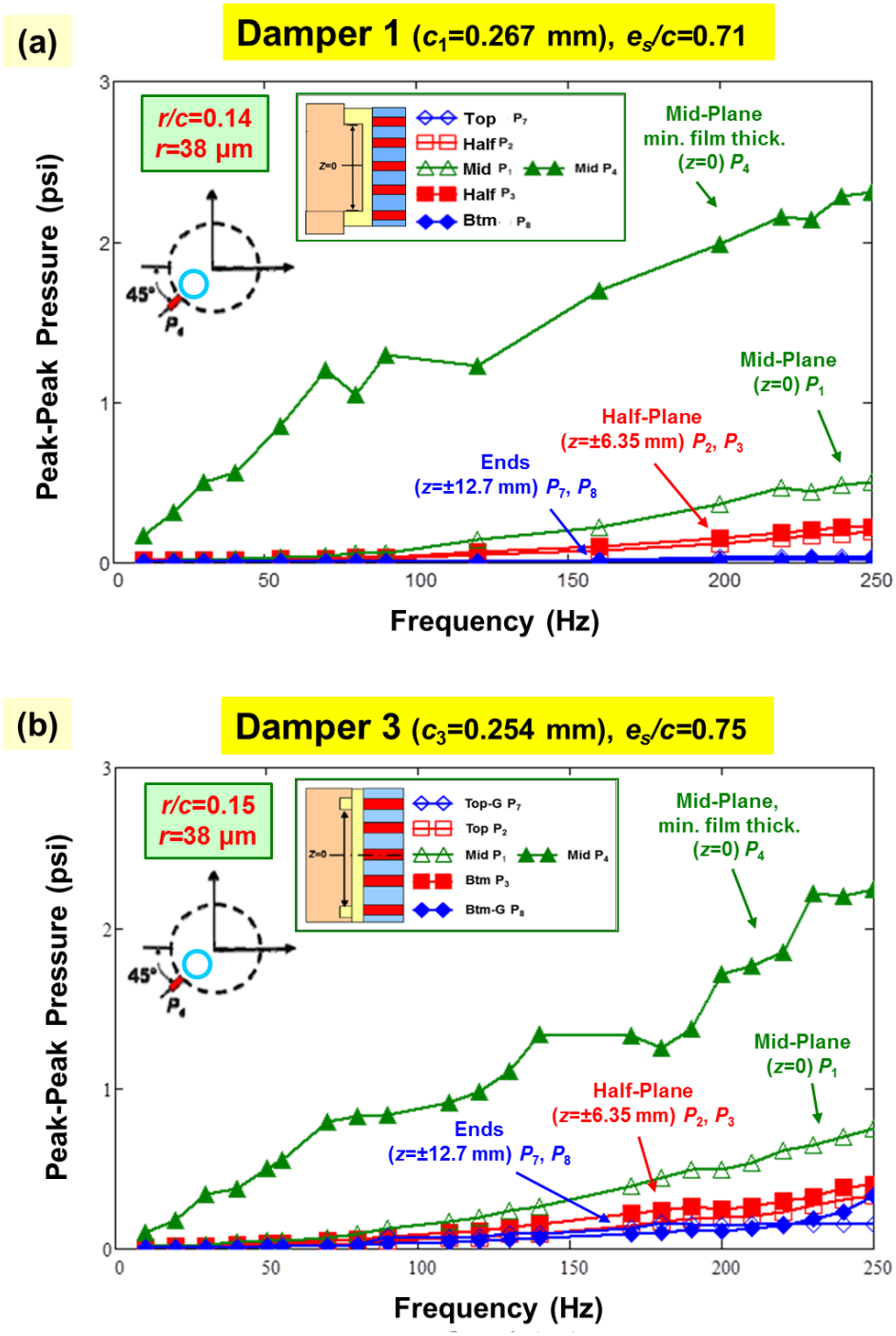

Figure G.4. Open-ends SFDs: Recorded *peak-to-peak* film dynamic pressures versus excitation frequency (ω) for (a) damper 1 (c_1=0.267 mm) and (b) damper 3 (c_3=0.254 mm). Largely off centered (e_s/c≈0.75) circular orbit tests with radius r/c=0.15. Measurements at the damper mid-plane, top and bottom half-planes, and bottom end groove. (Insets show location of pressure sensors along film land and journal position relative to the BC).